UNIVERSITY OF SOUTHAMPTON

FACULTY OF ENGINEERING, SCIENCE AND MATHEMATICS

School of Ocean and Earth Science

Influence of high latitude anomalies on tropical climate phenomena and global climate

PhD Thesis

Adam Blaker

September 2006

For Fiona

Abstract

The tropical ocean and atmosphere are a highly active and very important region of the globe. Climate phenomena such as El Niño (*Philander*, 1990), the Tropical Atlantic Dipole, and the Indian Ocean Dipole, play an important role in global climate variability. The tropical atmospheric boundary layer is very sensitive to even small changes in the sea surface temperature (SST). Small SST anomalies in the tropics can lead to shifts in the large scale convection cells and result in atmospheric heating. There is potential for positive feedback between the tropical ocean and atmosphere.

Ocean waves are capable of propagating long distances very fast. Barotropic waves (adjustments in free surface height) can propagate round the globe within days. Baroclinic waves, propagating along the thermocline are able to cross the equatorial Atlantic in 2 – 3 months. This work shows the potential for ocean wave propagation to influence global climate, by linking high latitude anomalies to tropical climate phenomena.

The first part of this thesis is a detailed examination of the "Tropical Atlantic Dipole" (TAD). Analysis of model data shows a dipole pattern in the SST, with strong cross-equatorial asymmetry in the surface mixed layer. Below the mixed layer the pattern becomes symmetric, and Kelvin and Rossby wave like adjustment can be seen to occur. However, the timeseries is not sufficiently long to provide confidence in resolving the power spectrum, and as such the results are inconclusive. The complexity of the model makes it difficult to identify the mechanism(s) which are responsible for driving the dipole. An idealised basin model is used to examine high latitude anomalies which create equatorward propagating coastal Kelvin waves as a possible driving mechanism for the TAD. The results show that coastal Kelvin wave propagation can quickly transmit a signal from the high latitude anomaly to the equator, and equatorial Kelvin and Rossby wave propagation can quickly influence the entire tropical ocean. This suggests that forcing of the TAD may come from higher latitudes, although it is still not fully understood how a symmetric sub-surface signal can become asymmetric at the surface. Restoring surface boundary conditions limit the response of the model, restricting the formation of a TAD. A similar experiment, using an idealised coupled model configuration is suggested, but not possible in the time available.

The second part of this thesis looks in detail at the role of the ocean in rapidly transmitting a high latitude response to the equator, using an existing coupled climate model configured with realistic land geometry and bottom topography. Simulations of a salinity anomaly in the Southern Ocean show that it is possible to create an equatorial response in SST within a month, with SST anomalies of

2.5° after 6 months. Barotropic Kelvin and Rossby wave propagation is shown to be important in creating such a rapid equatorial response. Two points that are identified from this experiment are examined in further detail using an idealised basin model. Firstly, a mechanism for energy exchange within the equatorial waveguide is tested. Results suggest that it is not the mechanism responsible for the signals seen in the coupled climate model. Secondly, idealised model integrations confirm that transmission of signals along topographic ridges is possible. Signals strong enough to excite equatorward coastal Kelvin wave propagation are able to use topography to cross the Southern Ocean and reach the coast of Australia.

Acknowledgements

I am very grateful to my supervisor, Dr Neil Wells, for the help, advice, encouragement and support he has provided me throughout my PhD.

I would like to thank Dr Bablu Sinha for his continued support, advice and assistance, in particular with the numerical models used throughout this work, and Dr Vladimir Ivchenko for useful discussions and advice. Thanks are also due to Dr Rowan Sutton of the University of Reading for some useful discussion and guidance.

Thanks also to the members of my panel, Professor Jochem Marotzke, Dr Brian King and Professor Peter Killworth, who offered advice and guidance and ensured that the course of my PhD went smoothly.

I would like to thank the members of the COAPEC project, and of the James Rennel Division at NOC,S for many useful discussions over the past four years.

On a personal note, I would also like to thank Fiona and my parents for their continued support throughout my PhD.

This work was supported by the NERC funded Coupled Ocean Atmosphere Processes and European Climate (COAPEC) project.

Contents

List of Tables

List of Figures

Chapter 1

Introduction

1.1 Introduction

The tropical atmospheric boundary layer is very sensitive to the sea surface temperature (SST). Small SST anomalies in the tropics can lead to shifts in the location of large-scale convection cells and result in atmospheric heating (*Trenberth et al.*, 1998). The consequence of this is that tropical climate phenomena have a global impact, frequently appearing in the media for causing flooding, drought and extreme weather. El Niño is the most widely known, with an interannual cycle. Other phenomena include the Indian Ocean Dipole (IOD) and the Tropical Atlantic Dipole (TAD).

The TAD is of particular interest due to its potential to affect European climate. Numerous studies of the relationship between rainfall in the Sahel (N. Africa) and Nordeste (N.E. Brazil) regions and the tropical Atlantic Sea Surface Temperature (SST) have been published and some suggest that a decadal N/S oscillation plays a significant role in the climate in these regions. Studies which have attempted to identify the mechanisms driving the TAD have provided mixed, and often contradictory, results. A theory published by *Yang* (1999) suggests coastally trapped waves may transmit a signal from northern hemisphere high latitudes to the tropical Atlantic, and that the decadal variability of the TAD may be driven by decadal variations in Labrador Sea Water (LSW) formation. The LSW thickness has a significant decadal component, and air-sea heat flux variation associated with the North Atlantic Oscillation (NAO) are largely responsible for these variations. The NAO is known to be an important climate signal at decadal timescales (*Rogers*, 1990; *Cayan*, 1992; *Hurrel*, 1995). Coastally trapped wave propagation was later observed by *Dong and Sutton* (2002a) in a modified version of HadCM3, the UK Met Office global coupled ocean-atmosphere general circulation model, when they induced a perturbation in the Meridional Overturning Circulation (MOC) by freshening the upper 500 m of the north

Atlantic by a salinity of 2, equivalent to a freshwater influx of around 3 x 10^{14} m^3.

Improved prediction of climate phenomena such as El Niño and the TAD could alleviate suffering in many third world countries. The ability to forecast the cycle of these tropical climate phenomena would enable better planning and preparation for aid and assistance to the worst affected areas. Predicting tropical climate events relies on an understanding of the driving mechanisms behind them. The work presented here examines remote forcing through the propagation of fast ocean waves from high latitudes as a potential driving mechanism for tropical climate phenomena.

The TAD is examined in detail using data from HadCM3. An idealised Atlantic Ocean basin setup is then used to examine the ocean wave response to a high latitude anomaly. The same model is forced with a high latitude fluctuating salt forcing similar in design to that used by *Yang* (1999), to try and elucidate the driving mechanism behind the asymmetric cross-equatorial SST anomaly.

A further study using FORTE, an intermediate resolution coupled climate model, looks at the response of the coupled climate system to a salinity anomaly in the Southern Ocean. High temporal resolution data show that anomalies at high latitudes have rapid implications for the whole globe.

1.2 Planetary waves

Planetary waves are fundamental to the teleconnections discussed later in this thesis. An overview of the different kinds of planetary wave that are important is given here.

Planetary waves in the ocean are often seen to propagate along lines of constant density (pycnoclines). The most obvious example is the surface of the ocean, which is known as the barotropic (external, depth averaged) mode of propagation. It is the fastest mode of propagation and carries the majority of the energy. Barotropic waves have an amplitude of the order of 1 m, and wave speeds are in the order of $100 - 300$ m s^{-1}. Planetary waves may also travel along lines of density where strong changes in the density profile exist, such as the thermocline. These are known as baroclinic (internal) modes of propagation, and may be infinite in number. Successive baroclinic modes decrease in strength, and typically only the first few are of importance. Higher baroclinic modes propagate with speeds comparable to the flow speed, giving rise to strong interaction between the waves and the mean flow which makes analysis difficult unless the mean flow varies slowly over the wavelength. The first baroclinic mode, usually found on the thermocline has a typical amplitude of around 50 m, much larger

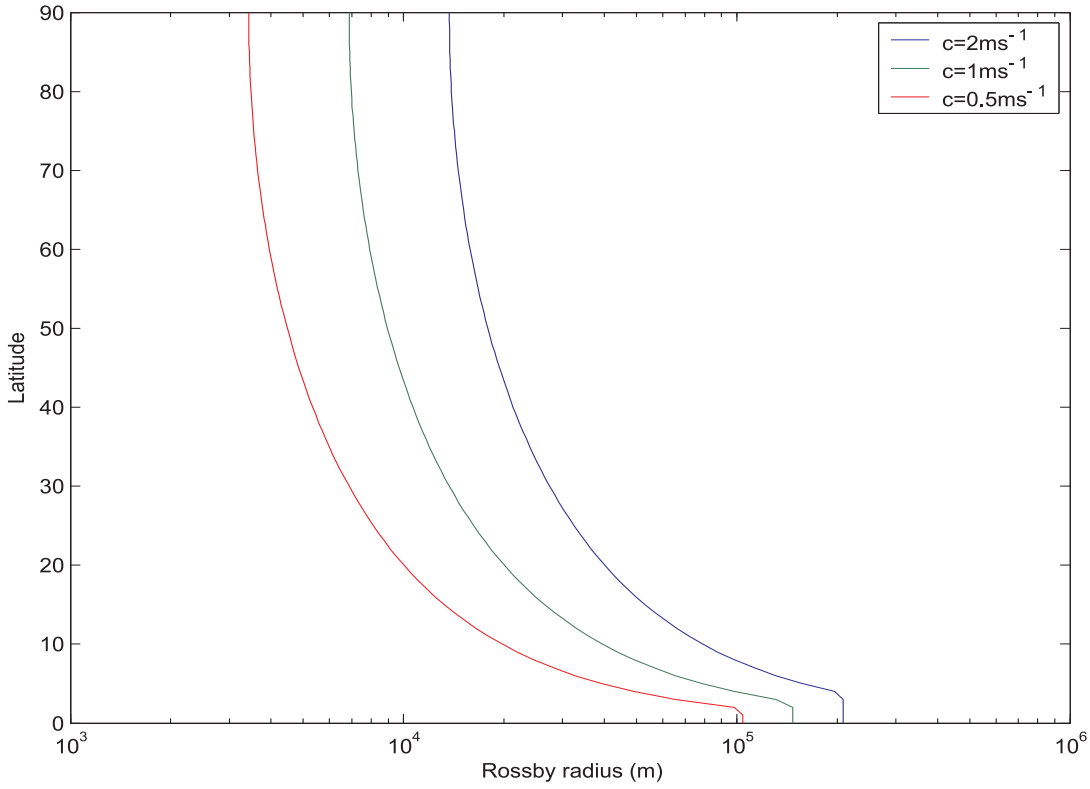

Fig. 1.1: Rossby radius with latitude for different values of c, including the equatorial Rossby Radius. The two solutions are merged at a distance of one equatorial Rossby Radius away from the equator.

than its barotropic counterpart due to the considerably smaller density difference between the layers. Wave speeds for the first baroclinic mode are typically $1-3$ m s^{-1}. Baroclinic modes give the departure from the depth averaged velocity.

Two forms of planetary waves are described here: Kelvin waves, which are coastally trapped, and propagate around the ocean boundary; and Rossby waves, which propagate westward across ocean basins. A third form of large scale wave is also mentioned, which is the coastal shelf wave. This wave follows topography, and is important where topography exists away from the coast.

1.2.1 Kelvin waves

Kelvin waves are coastally trapped gravity waves. In the NH (SH) Kelvin waves propagate anticlockwise (clockwise), with the boundary always to the right (left). Wave velocity is around $2-3$ m s^{-1} for the first baroclinic mode. Amplitude of the wave decays exponentially away from the boundary, with a decay scale of one Rossby radius, defined as $a = c/f$, where c is the wave speed, and $f = 2\Omega \sin\phi$ is the Earth's rotational frequency. The Rossby radius decreases with latitude, with a maximum value at the equator and a minimum at the poles (Fig 1.1).

The dispersion relation for a Kelvin wave propagating along a coastline is (*Gill* (1982), p.379):-

$$\omega = ck \tag{1.1}$$

where ω is the angular frequency, and k is the wave number.

1.2.2 Rossby waves

Rossby waves can be found propagating westward in the ocean, confined to a region between the equator and a critical latitude, beyond which the waves are unable to propagate. The critical latitude is not constant in the real ocean, but varies with longitude and wave velocity. For most locations, a typical value for the critical latitude is around 40°. Wave velocity depends strongly on latitude, with maximum velocities in the first baroclinic mode of around $1\ \mathrm{m\,s^{-1}}$ near the equator. The dispersion relation for Rossby Waves, which shows that all Rossby waves have westward phase velocity, is (*Gill* (1982), p.446):-

$$\omega = \frac{-\beta k}{(k^2 + l^2 + \frac{f^2}{c^2})} \tag{1.2}$$

where $\beta = 2\Omega \cos\phi / r$, k and l are the meridional and zonal wave numbers.

Rossby waves occur because at any point in the ocean the Coriolis force and the horizontal pressure gradient must be in geostrophic balance. Imbalances caused by changes in the system, for example density anomalies caused by fresh water or salt input, are compensated by the generation of Rossby waves.

Observed Rossby waves propagate faster than predicted using linear flat-bottom theory (*Chelton and Schlax*, 1996). Inclusion of the baroclinic mean flow into the theory is reasonably successful in reducing this discrepancy (*Killworth et al.*, 1997). The effects of bottom topography is also successfully shown to be locally important, although on a basin wide scale this effect more or less cancels out (*Killworth and Blundell*, 1999). *Killworth and Blundell* (2003) combine the effect of both of these adjustments to theory, and show that the predicted speeds agree well with satellite observations of planetary wave propagation.

1.2.3 Coastal shelf waves

Coastal shelf waves follow f/H contours, where H is the ocean depth. In other words, they propagate along sloping topography. Their behaviour is similar to Kelvin waves because they follow topography, and to a first approximation,

topography in ocean basins is largely coastal. Notable exceptions to this rule are topographic ridges along the ocean floor such as the Mid-Atlantic Ridge and the East Pacific Rise. In the presence of both stratification and topography hybrid waves, which are a combination of Kelvin and coastal shelf waves (referred to as 'coastally trapped waves' by *Gill and Clarke* (1974)), propagate (*Gill* (1982), p.415).

1.2.4 Equatorial propagation

There exists a special case for waves which propagate within the equatorial waveguide. The equatorial waveguide is defined as the region either side of the equator which is bounded by the equatorial Rossby radius. The equatorial Rossby radius is defined as $a_e = (c/2\beta)^{1/2}$, which for the ocean, assuming $c \approx 200$ $\mathrm{m\,s^{-1}}$, is around 2000 km. For the baroclinic mode, where $c \approx 0.5 - 3$ $\mathrm{m\,s^{-1}}$, the equatorial Rossby radius is 100 – 250 km.

Kelvin waves

Kelvin waves propagate along the equator, always in an easterly direction. In this unique case the Kelvin wave is not bounded by a coastline, instead the wave appears symmetric about the equator. An important result of this unique property is that a coastal Kelvin wave propagating equatorward along the western boundary, for instance in the northern hemisphere, forms a symmetric response about the equator. On reaching the eastern boundary the Kelvin wave will divert poleward in both hemispheres. This is one mechanism by which it is possible for energy from one hemisphere to cross the equator and excite a response in the other. The dispersion relation for equatorial Kelvin waves is the same as for coastal Kelvin waves, which is (*Gill* (1982), p.437):-

$$\omega = ck. \tag{1.3}$$

The first baroclinic mode Kelvin wave propagates along the equator at a speed of 2.8 $\mathrm{m\,s^{-1}}$, which means that it will take around 2 months to cross the equatorial Pacific, around 1 month for the Atlantic. The barotropic mode can propagate signals across the Atlantic Ocean in less than a day.

Rossby waves

It is also possible for Rossby waves to propagate within the equatorial waveguide. Rossby waves propagating within the equatorial waveguide will

always propagate westward. The dispersion relation for equatorially trapped Rossby waves is (*Gill* (1982), p.439):-

$$\omega = \frac{-\beta k}{(k^2 + (2n+1)\frac{\beta}{c})} \tag{1.4}$$

where n is the mode of propagation.

This comes from the general dispersion equation, which describes both Poincare and Rossby waves:-

$$\frac{\omega}{c}^2 - k^2 - \beta k/\omega = (2n+1)\frac{\beta}{c}. \tag{1.5}$$

1.3 The Tropical Atlantic

The tropical Atlantic is a complex region, with many prominent features in both the ocean and atmosphere. Interactions between the ocean and atmosphere play a significant role in the regional climate.

1.3.1 Ocean

The tropical Atlantic ocean current structure is complex. The major features will be briefly discussed here to give an idea of the general layout.

The North Equatorial Current (NEC) forms the southern part of the the North Atlantic subtropical gyre. It is a broad current found north of 10°N and has a westward mean velocity around 10 – 15 cm s^{-1} (*Richardson and Walsh*, 1986). Annual mean transport is 8.5 Sv (1 Sv = 10^6 m^{3}s^{-1}). Lowest transports occur during late boreal winter and spring (*Bayev and Polonskiy*, 1991). The maximum variation in transport occurs between June and January and has a magnitude of 1.5 Sv. The NEC also contributes around 12 Sv to the North equatorial Under Current at intermediate depths (around 100 – 300 m) (*Wilson et al.*, 1994). The NEC reaches peak values of 15 cm s^{-1} in boreal summer with a weakening to 10 – 12 cm s^{-1} during spring and fall (*Arnault*, 1987). The North equatorial Current feeds into the Guiana current, which feeds the Caribbean currents.

The South equatorial Current (SEC) has been traditionally shown to originate from the Benguela Current in the eastern south Atlantic. The current flows west towards south America, and is clearly defined as 3 separate branches (*Molinari*, 1982; *Stramma*, 1991). Upon reaching South America the current separates, forming the North Brazil Current (NBC) and the Brazil Current. The NBC heads north along the coast and the Brazil Current heads south. Velocities and transport vary depending on the individual branches.

The NBC closes the wind-driven equatorial gyre circulation and feeds a system of zonal countercurrents. It also provides a pathway for cross-equatorial transport of upper ocean waters as part of the Atlantic meridional overturning cell (*Johns et al.*, 1998). Large anticyclonic rings shed by the current propagate northwestwards along the South American coast (*Arnault et al.*, 1999; *Fratantoni et al.*, 1995; *Paris et al.*, 2002; *Schott et al.*, 1998).

The Guinea Current flows east at approximately 3°N along the western coast of Africa. Upon reaching the Gulf of Guinea (near 5°W), velocities close to 1 $\mathrm{m\,s^{-1}}$ can be obtained (*Richardson and Reverdin*, 1987). The North equatorial Countercurrent (NECC) and the Canary Current are its two main sources. Compared to other upwelling regions the Guinea Current is unusual. There appears to be no correlation between SST and wind patterns on seasonal timescales (*Longhurst*, 1962; *Bakun*, 1978). *Binet* (1997) suggests the seasonal upwelling in the thermocline is induced by geostrophic adjustment of isotherms (*Ingham*, 1970), Kelvin waves (*Picaut*, 1983; *Verstraete*, 1992), and cyclonic turbulent eddies (*Marchal and Picaut*, 1977) instead of local windstress.

The NECC lies between 3° – 10°N. It acts as the northern boundary for the SEC (*Peterson and Stramma*, 1991). The NECC is fed mainly by the upper layers (1000 m) of the NBC between 5° – 8°N (around 16 Sv). An additional contribution of around 8 Sv is provided by the NEC (*Wilson et al.*, 1994). The mean eastward velocity is around 15 $\mathrm{cm\,s^{-1}}$, increasing to speeds of more than 30 $\mathrm{cm\,s^{-1}}$ as it reaches the Guinea Current (*Arnault*, 1987). During the early months of the year the majority of the current's flow is reversed in the western part of the basin (*Arnault*, 1987).

Detailed descriptions of all surface currents in the Atlantic ocean are accessible on the ocean currents website (*Bischof et al.*, 2001).

1.3.2 Atmosphere

The atmosphere above the tropical Atlantic plays an important role in the state of the climate in the region. The dominant winds in the tropical Atlantic Region are the trade winds. The trade winds blow from the north-east in the northern hemisphere and the south-east in the southern hemisphere, and both have a significant westerly component. They meet at the Inter-Tropical Convergence Zone (ITCZ). The ITCZ is a long line of convergence, which is frequently responsible for heavy precipitation. It oscillates about the equator throughout the year, spending the majority of its time north of the equator (*Philander et al.*, 1996). When the ITCZ moves north over West Africa it brings with it warm moist air from across the Atlantic, which results in precipitation. The SST

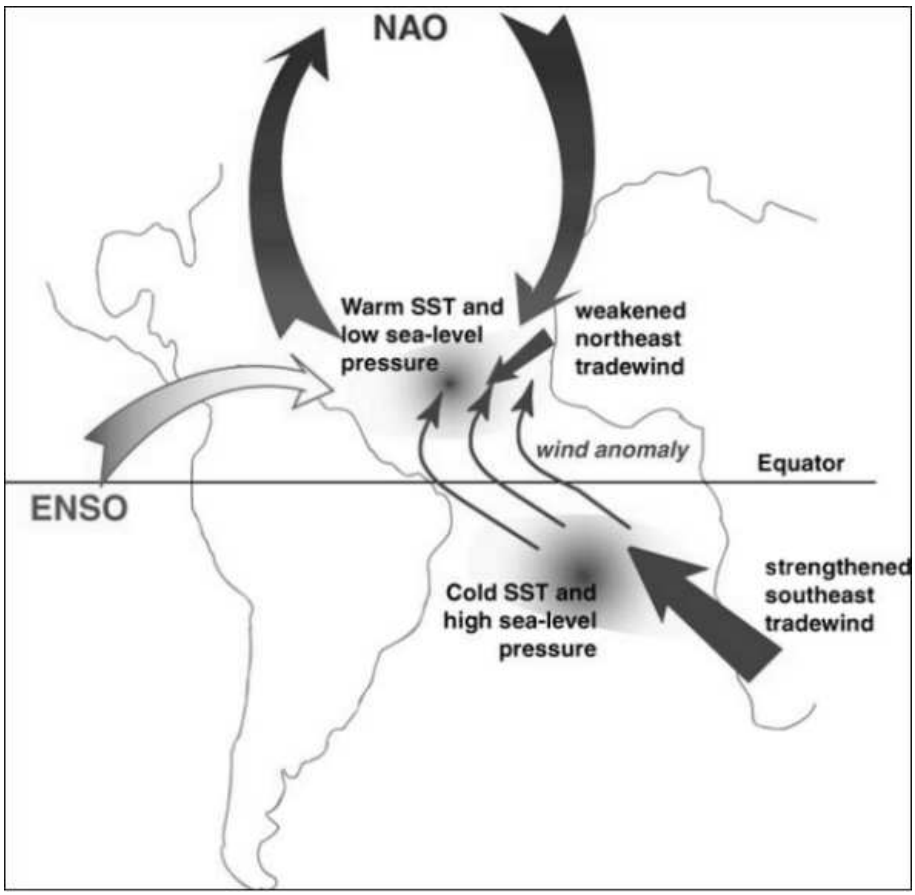

Fig. 1.2: Spatial location and some suggested driving mechanisms of the "Tropical Atlantic Dipole" (courtesy P. Chang.)

gradient between the northern and southern hemisphere hydrostatically controls the pressure, therefore determining the wind field and latitudinal location of the ITCZ (*Hastenrath and Druyan*, 1993; *Hastenrath and Greischar*, 1993). Consequently it is possible to generate a positive air-sea feedback associated with the ITCZ (discussed later).

1.4 The Tropical Atlantic Dipole

The TAD is a decadal oscillation of SST, occurring between 10° – 20° N and 0° – 20° S (Fig 1.2), with a maximum of around 0.5 – 1.5°C amplitude. Spatially, it covers a large area of the tropical Atlantic. The northern lobe of the TAD is generally smaller and better defined spatially, but often larger in amplitude.

One thing made clear by previous studies is that the tropical Atlantic region is influenced by several phenomenon of comparable importance, such as El Niño, the North Atlantic Oscillation and the Tropical Atlantic Dipole, which act on a wide range of timescales. Separating these phenomenon has proved difficult, and some of the wide variation in the conclusions drawn by the community may

be accounted for by the analysis of data from different periods of time during which the tropical Atlantic was dominated by different phenomenon.

The majority of research has been concentrated on the effects of tropical Atlantic SST anomalies on rainfall in regions such as the Nordeste and the Sahel (*Moura and Shukla*, 1981; *Lough*, 1986; *Folland et al.*, 1986; *Hulme*, 1992; *Rowell et al.*, 1995). Attempts have been made to identify the climate phenomena which cause floods and drought in these regions, but currently no mechanism has been identified which is able to explain why these phenomenon exist.

1.4.1 Observational evidence

Attempts to identify the TAD have used numerous satellite and Earth based observational datasets. Most have focussed largely on atmospheric quantities (Sea Level Pressure (SLP), Surface Air Temperature (SAT), Rainfall and Wind Stress) and SST. Observations of the ocean interior are limited both spatially and temporally.

Observational data prior to satellites was measured in-situ, either using buoys or sampling from ships. From here the data is often interpolated to a uniform grid using sophisticated statistical methods, and this data is often incorporated into reanalysis datasets. The number of available datasets increased dramatically around the late 1960's due to the introduction of satellites, explaining why so many studies have used 30 – 40 year datasets. Satellite observations provide both high spatial and high temporal resolution of SST, and the regular and expansive sampling makes the datasets an invaluable resource.

The vast majority of datasets used are relatively short (30 – 40 years) for identifying a decadal signal. A significantly longer timeseries is necessary to resolve a decadal signal with any confidence (*Dommenget and Latif*, 2002; *Carton et al.*, 1996). The longest observational dataset available is the GISST dataset (*BADCwebsite*, 2006) which runs from 1871 to 2003. The GISST dataset has been interpolated to a 1° x 1° grid from SST observations. Since February 2003 the GISST dataset has been replaced by the HadISST dataset. A 90 year section of the GISST data was examined by (*Dommenget and Latif*, 2000). EOF analysis of the unfiltered annually averaged data showed the TAD as the second mode, with 22.2% of the variance. The first EOF shows a basin wide mode, accounting for 33.7% of the variance. *Dommenget and Latif* (2000) suggest that 90 years may even be too short to reliably resolve a decadal signal. Considering the fact that so many studies have used such short datasets, it is understandable that such a wide variety of conclusions about the existence of the TAD exist.

Observed effects on local climate

The TAD interacts with the atmosphere, resulting in abnormalities in the rainfall pattern in both South America and West Africa. Correlation between seasonal rainfall in the Nordeste and tropical Atlantic rainfall indicates an out of phase relationship between SST anomalies in the ocean regions underlying the northern and southern hemisphere trade wind regions (*Hastenrath and Heller*, 1977; *Markham and McLain*, 1977; *Moura and Shukla*, 1981). Dry Nordeste years tend to occur when SSTs north of the equator are warmer than normal and SSTs south of the equator are colder than normal. Rainfall in subtropical west Africa is more complex but also displays considerable dependence on a similar out of phase variation of SST in the tropical Atlantic (*Lamb*, 1978; *Lough*, 1986; *Lamb and Peppler*, 1987). Rainfall increases when Northern Hemisphere subtropical SSTs are warm, and Southern Hemisphere SST are cold.

Despite the fact that it is relatively easy to generate long datasets using numerical models, there are few studies which have exploited this resource. Perhaps more surprising is the fact that although ocean models are able to provide variable fields for the ocean interior (T, S, east/north/vertical velocities, mixed layer depth, etc.) no analysis of these variables in relation to the TAD has been published. Analysis which considers only the SST signals and does not extend below the surface may provide a false impression of the physical mechanisms present (*Joyce et al.*, 2004). Heat exchange from the ocean to the atmosphere is not solely dependent on SST. For example, an area of high SST may have a lower rate of heat transfer to the atmosphere than an area with lower SST and greater wind velocity. *Joyce et al.* (2004) note that the interannual SST signal in the tropical Atlantic shows little correlation to the interannual heat flux forcing. There is even some degree of negative correlation near the African coast, suggesting that ocean advection is important in determining SST over much of the region.

1.4.2 Driving Mechanisms

Unlike the Pacific Ocean the tropical Atlantic is not dominated by a single mode of variance (ENSO). *Sutton et al.* (2000) identify four forced signals in the tropical Atlantic atmosphere. These are (a) the NAO, which is the dominant component of tropical Atlantic atmospheric variability, (b) a remote response to ENSO, (c) a response to the TAD SST pattern, and (d) a response to equatorial Atlantic SST anomalies. This study illustrates the difficulty of trying to identify the TAD and its driving mechanism(s). The atmosphere can be seen to respond to no less than four different signals, two of which are remote from the tropics and transmit their signal atmospherically (ENSO and NAO), and two of which are local influences

from the ocean that may themselves have remote driving mechanisms.

The strongest influence of ENSO in the northern tropical Atlantic has been found in a number of cases to be in boreal winter and spring (*Chang et al.*, 2000; *Curtis and Hastenrath*, 1995; *Enfield and Mayer*, 1997; *Harrison and Larkin*, 1998; *Giannini et al.*, 2000).

Czaja et al. (2002) compiled three separate timeseries to produce a 110 year timeseries running from 1882 to 1992. Analysis showed that in the northern tropical Atlantic remote forcing from ENSO was more significant at interannual timescales (2 – 7 years), but that the North Atlantic Oscillation (NAO) became the dominant source of remote forcing at longer timescales. *Enfield and Mayer* (1997) also investigated correlation between ENSO and the tropical Atlantic using the Comprehensive Ocean Atmosphere Data Set (COADS) dataset from 1950 to 1992. They found that ENSO and a region between 10°N and 20°N in the tropical Atlantic are significantly positively correlated with a time lag of 4 – 5 months on seasonal to interannual timescales. This result is again confirmed by *Handoh et al.* (2006), who looked at SST from the GISST dataset and windstress and sea level pressure (SLP) from the NCEP-NCAR reanalysis dataset (*Kalnay et al.*, 1996) between 1948 and 1999.

Carton et al. (1996) applied a model based on the GFDL-MOM code to try and identify the major processes in the tropical Atlantic. The model they used covered the Atlantic basin from 30°S to 50°N, with a 0.5° x 1.5° horizontal resolution in the tropics expanding poleward of 10° latitude to a uniform 1.5° grid at midlatitudes. It includes 20 vertical layers, with 15 m resolution in the upper 150 m. A 30 year intergration forced with monthly averages of daily windstress obtained from the COADS surface observation dataset was completed. Two dominant timescales responsible for SST variability in the tropical Atlantic were identified. The first is a decadal signal controlled by latent heat flux anomalies, which is primarily responsible for off-equator SST anomalies. It appears as a distinct oscillation of the order 10 – 12 years seen in the interhemispheric difference in SST' (defined as $T'_N - T'_S$, where T' is temperature anomaly) in both observational and model data. The dipole signal present in the northern tropical Atlantic is stronger than the signal in the southern tropical Atlantic. *Carton et al.* (1996) found that the decadal signal responded to changes in cloudiness, evaporation, local wind driven effects, remote effects due to changes in coastal upwelling, and changes in intrahemispheric heat transports. Varying winds, which affected latent heat loss from the surface, resulted in the largest changes. This suggests that the atmosphere does play an important role in the TAD. The second signal is a higher frequency (2 – 5 yr), located on the equator and dominated by dynamical processes.

SST anomalies in the equatorial Pacific arise through zonal shifts of excess oceanic

heat content (*Zebiak*, 1989). *Carton et al.* (1996) note that, in contrast to the Pacific, the SST anomalies in the Atlantic, particularly in the eastern side of the basin, are highly correlated with thermocline depth. If the TAD relies on a mechanism adjusting the thermocline (and therefore heat content) to adjust the SST then it may be largely confined to the eastern side of the basin.

Huang and Shukla (1996) note that SST anomalies appear to result from different physical processes. In one example, they find that close to the North African coast a reduction in upwelling results in a positive SST anomaly. The SST here is sensitive to small changes in the thermocline, but further west the SST proves to be less responsive to larger changes in the thermocline. To the west SST anomalies are strengthened by reductions in evaporative heat loss due to weakening of the trade winds. *Huang and Shukla* (1996) suggest that the anomalies in the tropics are associated with basin wide redistribution of heat content. This implies that decadal anomalies in the southern tropical Atlantic are strongly related to anomalies in the northern tropical Atlantic.

Liu (2002) relates extratropical Rossby waves to the maximum memory of the tropical ocean, suggesting wave propagation plays a significant part in tropical Atlantic variability. The memory of the tropical ocean is defined as the time for which a signal may remain present within the region, and therefore be able to influence the region. Due to the decrease of Rossby wave propagation speed with increasing latitude, higher latitude regions tend to have longer memories. Since higher baroclinic modes are progressively slower, it is possible that the tropical ocean may gain memory locally from these modes (*Liu et al.*, 2002). *Liu* (2002) also suggests that nonlinearity (*Munnich et al.*, 1991) and ocean-atmosphere coupling (*Jin*, 2001) may have an important part to play in the tropical ocean.

Zebiak (1993) notes that there is no such large scale north/south oscillation in the Pacific Ocean, which suggests that the processes which drive the TAD are either weak or not at all present in the Pacific Ocean. This indicates that in order to identify the driving mechanisms of the TAD it is necessary to locate mechanisms which are only present in the Atlantic, such as the strong (1PW) northward cross-equator heat transport found in the Atlantic (*Trenberth and Caron*, 2001) or the NH high latitude sinking.

Carton et al. (1996) highlight the conclusion by *Hayes et al.* (1991), which indicates the difficulty of identifying the dominant physical processes controlling SST within the strongly coupled ocean-atmosphere system. From this conclusion it is clear that simpler modelling studies are necessary in order to enhance our understanding, of the system.

Chang et al. (2000) note that tropical Atlantic variability is more complex than in the Pacific and may involve local feedbacks and interactions with other climatic

modes such as ENSO and the NAO. If, as is shown by *Sutton et al.* (2000), tropical Atlantic variability is to some extent dependant on external parameters, individual signals would not show as readily as ENSO. *Chang et al.* (2000) also note the strong importance of the cross-equatorial SST gradient to atmospheric circulation. *Chang et al.* (1997) suggest that the ocean would provide the negative feedback necessary to balance the atmosphere, generating a dipole oscillation. *Sutton et al.* (2000) do not support the suggestion that the tropical Atlantic dipole is a coupled ocean-atmosphere mode of variability.

Dommenget and Latif (2000) state that 'If ocean dynamics, such as wave propagation, convection, and advection are of minor importance for the generation of the SST variability in the tropical Atlantic, atmospheric forcing has to be the dominant process for producing SST anomalies.' . Research by *Dong and Sutton* (2002a); *Goodman* (2001); *Yang* (1999) suggests that wave propagation is significant in generating SST variability in the tropical Atlantic. *Liu* (2002) also provides argument against *Dommenget and Latif* (2000) by suggesting that both wave propagation and ocean dynamics play a role in the tropical Atlantic.

1.4.3 Evidence for high latitude forcing of the TAD

Dong and Sutton (2002b) consider heat transport and heat content variability in the north Atlantic, using a modified version of the HadCM3 climate model. They find that Ekman processes dominate interannual variability of the ocean heat transport. For lower frequency variability (decadal) variations in the THC and gyre circulations are more important. *Dong and Sutton* (2002b) concentrate on the north Atlantic but the lower extremity of the study is 15°N, which is well inside the tropical Atlantic region. *Dong and Sutton* (2002a) suggest that Kelvin waves propagating from high latitudes may play a significant role in tropical Atlantic variability. Kelvin wave propagation from high latitudes to the equator could enable the transfer of THC driven decadal variability from the North Atlantic to the tropical Atlantic.

Yang (1999) considered the possibility of extratropical influences such as water mass formation at high latitudes, generating cross-equatorial flow variability and leading to the creation of a gradient in SST by the process of advection. An adaptation of the GFDL-MOM model, with 0.5° x 1.0° horizontal resolution, is forced at high latitudes with a decadal salt forcing and produces a decadal oscillation about the ITCZ, located predominantly in the western basin. Yang suggests that since findings in previous studies tend to favour dipole locations in more central and eastern locations, there may be multiple dipole modes which are driven by different mechanisms.

CGCM	Time Resolution	No. of years	Spatial Resolution
ECHAM4-HOPE2	Annual mean, detrended	118	2.8125° x 2.8125°*
ECHAM4-OPYC	Annual mean, detrended	240	2.8125° x 2.8125°*
ECHAM3-LSG	Annual mean, detrended	700	5.625° x 5.625°
GFDL-MOM	Annual mean, detrended	1000	7.5° x 4.5°

* The ocean model has a meridional resolution of 0.5° within the region 10°N – 10°S

Table 1.1: List of CGCM's used by *Dommenget and Latif* (2000)

1.4.4 Disputed existence of the dipole

The scientific community is divided regarding the existence of the "Tropical Atlantic Dipole". Studies have been carried out on numerous datasets, from satellites, observations and model data, and the conclusions fall approximately equally into two main groups; either the dipole exists and plays a significant role in the tropical Atlantic climate, or decadal variability in the two hemispheres is uncorrelated with time. All studies agree that there is a significant amount of decadal variability in the tropical Atlantic. *Huang and Shukla* (1997) comment on the highly contradictory conclusions drawn in the literature from analysis of datasets using different statistical methods.

Houghton and Tourre (1992) examined a dataset of the tropical Atlantic between 1964 and 1988. Analysis showed that a dipole structure was present in the second EOF. The anomalies north and south of the ITCZ are not found to correlate significantly on a decadal timescale. The same result was concluded by *Enfield et al.* (1999); *Zebiak* (1993); *Dommenget and Latif* (2000). *Dommenget and Latif* (2000) argue that EOF analysis showing a dipole in the tropical Atlantic does not represent a physical mode. This argument is based on results from analysis of GISST data between 1903 and 1994, and results from four different general circulation models (GCM's), (Table 1.1).

In contrast, many papers conclude that the TAD is a real physical mode which affects not only the Atlantic Ocean itself, but also the surrounding land in the Nordeste and Sahel regions (*Weare*, 1977; *Moura and Shukla*, 1981; *Servain*, 1991; *Sutton et al.*, 2000; *Nobre and Shukla*, 1996; *Hastenrath and Greischar*, 1993; *Chang et al.*, 1997; *Carton et al.*, 1996; *Tourre et al.*, 1999). *Servain* (1991) found that using conventional EOF analyses the TAD is presented as a significant component of the tropical Atlantic variability. *Huang and Shukla* (1997) find well defined, predominantly off-equator decadal variations in the tropical Atlantic Ocean, which are as strong as the interannual variability.

Sutton et al. (2000) conclude that the TAD is better viewed as a sensitivity of the atmosphere to fluctuations in the cross-equator SST gradient. Latent heat

flux anomalies suggest a negative, not positive, feedback between the ocean and atmosphere. The atmosphere is considered to have a passive response to the SST anomalies. *Sutton et al.* (2000) point to remote forcing from ENSO and the NAO, atmospherically forced oceanic Rossby waves, and fluctuations in the meridional overturning circulation (*Yang*, 1999) as the main driving forces behind the SST anomalies.

Model studies of the TAD should be considered carefully. Previous studies have shown that high latitude sinking can influence the tropical Atlantic, and possibly lead to formation of an SST dipole (*Yang*, 1999; *Sutton et al.*, 2000). Model configurations which do not consider this influence may be missing a key feature of the mechanism. Careful consideration must also be given to interpretations of ocean only model integrations which are forced by atmospheric datasets. Atmospheric signals of the TAD which exist in the atmospheric datasets will be imposed onto the model ocean, possibly resulting in an SST dipole. Interpreting this as evidence that the TAD is atmospherically driven is dangerous, since there is no indication of how the TAD signal came to be in the atmospheric dataset. It is safer to consider model results from fully coupled global GCMs where forcing is provided solely through top of atmosphere (TOA) heat fluxes, or to use idealised experiments where the origins of anomalous signals can be traced.

Xie (2001) suggests that a plausible explanation for the lack of interhemispheric correlation in the tropical Atlantic would be a dipole and a monopole of similar amplitudes interacting, resulting in an apparent lack of correlation across the equator. To further this thought, it could be possible that influences of ENSO in the northern tropical Atlantic (*Czaja et al.*, 2002; *Enfield and Mayer*, 1997; *Handoh et al.*, 2006), or influences from the southern lobe of the NAO (*Czaja et al.*, 2002) may interact with the TAD to generate the same effect. This observation supports the argument made by *Carton et al.* (1996) that modeling studies are necessary to separate the competing mechanisms present in the tropical Atlantic ocean.

One thing that is largely agreed upon is that the cross-equator SST gradient is more important than individual anomalies in either hemisphere in influencing droughts in the Nordeste (*Hastenrath and Heller*, 1977; *Moura and Shukla*, 1981; *Hastenrath*, 1985; *Lough*, 1986; *Rao et al.*, 1993; *Harzallah et al.*, 1996; *Mehta*, 1998; *Chang et al.*, 2000). Clearly this stresses a greater significance on a cross-equator dipole, since the cross-equator SST gradient will be greatly enhanced compared to a single monopole of similar magnitude located in only one hemisphere. It also indicates that the magnitude of the individual poles does not necessarily have to be large to create a significant impact on the surrounding rainfall pattern.

Huang and Shukla (1996) use Principal Oscillation Pattern (POP) analysis as opposed to EOF analysis for two reasons. Firstly because the POP modes are calculated based on time periods, so that the analysis is equivalent to a

multivariate spectral analysis of vector time series (*Hasselmann*, 1988). Secondly because the POP modes are not necessarily standing oscillations, unlike those derived from EOFs, and propagation in the domain can be detected.

Chapter 2

Fundamentals of numerical models

2.1 Introduction

Numerical models today have been developed to suit many different tasks, ranging from high resolution eddy resolving models such as OCCAM (*Coward and de Cuevas*, 2005) to much faster integrating, lower resolution coupled climate models used to investigate climate changes over thousands of years, for example C-GOLDSTEIN (*Edwards and Marsh*, 2005). Many of today's models stem from the original ideas of *Bryan* (1969). *Semtner* (1974) and *Cox* (1984) expanded on the original work by *Bryan* (1969), leading to the the development of the GFDL MOM code. The MOM1.0 model and source code was released in 1990, and the latest version available today is MOM4.0, released in 2004. The GFDL MOM model code is arguably the most widely used ocean model today. MOMA, which is the ocean model used for subsequent chapters in this thesis, is a recoded version of MOM3.0 which has been adapted to run efficiently on array computers.

The following chapters of this thesis contain results derived from numerical models. This chapter provides an overview of some of the fundamental components of numerical models, such as the approximations used to simplify the equations, the actual equations solved, the model resolution and grid format, and important stability criteria. Introducing anomalies to a numerical model creates a geostrophic imbalance. Adjustment of the model as it returns to geostrophic balance causes wave propagation. It is important to understand how the models will respond to such anomalies, and how the response differs from theory. In this chapter the effects of horizontal resolution on Kelvin wave propagation are examined in an idealised model domain. For clarity, the focus of this chapter will be towards MOMA, but the approximations and stability criteria discussed are applicable to most primitive equation ocean models.

2.1.1 Approximations for the equations of motion

In order to make numerical models computationally feasible, it is necessary to make approximations which simplify the equations. Each approximation must be carefully considered to ensure that any alterations to the solutions of the equations are minimal. The equations must still represent the important large scale processes which occur in the ocean.

Three major approximations are used in order to simplify the equations and hence reduce the computational workload. Scale analysis is also used to eliminate very small terms. This means that, for little sacrifice, a significant gain in the speed of the model can be achieved. The approximations used are:-

Boussinesq approximation

Allows density to be treated as a constant, known as the Boussinesq density ρ_o, in all terms in the horizontal components of the equations of motion. However, in-situ density must be used when calculating the vertical components of the equations of motion which include a multiplying factor of g. The effects of density variations on the water mass are neglected, whilst the effects of weight are retained. This approximation is valid since changes in density with time are typically less than 2% of the depth averaged (Boussinesq) value of density within the ocean (*Gill* (1982), page 47).

Hydrostatic approximation

Allows the computation of pressure within the ocean from the hydrostatic equation. Thus, pressure is assumed to arise purely from the weight of the overlying water column and the pressure at the sea surface. Terms representing the Coriolis force arising from vertical motions (assuming the vertical scale of motion is much less than the scale height, which is always true for the ocean) can also be removed.

Incompressibility of seawater

The assumption that sea water is incompressible can be made, since advection of fluid parcels is much smaller than the speed of sound. This means that changes in density with pressure are negligible, which allows ρ to be eliminated from the equation of mass conservation.

Scale analysis

Allows some terms to be neglected. For example, the non-linear advective term, $a^{-1}u(\mathbf{u} \wedge \hat{z}) \tan \phi$, is associated with the curvature of the coordinate system and can be neglected. It vanishes when working on a plane, such as the f or β plane as the grid spacing becomes constant.

2.1.2 The equations of motion

Numerical models solve a set of equations known as the 'primitive equations', which are described in *Bryan* (1969). These equations describe the motion of water in a basin. Horizontal and vertical velocities, as well as concentrations of tracers (temperature, salinity) are calculated and stored at regular intervals throughout each integration. Additional fields, such as passive tracers and the free surface height in MOMA, may also be output if they are calculated in the model. The following equations are given in spherical polar coordinates, which is the form in which they are solved in MOMA (*Pacanowski and Griffies*, 2000).

The horizontal momentum equations are:-

$$u_t = -\nabla \cdot (u\mathsf{u}) + v\left(f + \frac{u \tan \phi}{R}\right) - \left(\frac{1}{R\rho_o \cdot \cos \phi}\right) P_\lambda + (k_m u_z)_z + F^u, \qquad (2.1)$$

$$v_t = -\nabla \cdot (v\mathsf{u}) - u\left(f + \frac{u \tan \phi}{R}\right) - \left(\frac{1}{R\rho_o}\right) P_\phi + (k_m v_z)_z + F^v. \qquad (2.2)$$

The 3D advection-diffusion equations are:-

$$s_t = -\nabla \cdot [\mathsf{u}s + F(s)], \qquad (2.3)$$

$$\theta_t = -\nabla \cdot [\mathsf{u}\theta + F(\theta)]. \qquad (2.4)$$

The hydrostatic equation is:-

$$P_z = -\rho g. \qquad (2.5)$$

The incompressibility and density equations are:-

$$w_z = -\nabla_h \cdot u_h, \qquad (2.6)$$

$$\rho = \rho(s, \theta, z). \qquad (2.7)$$

The coordinates are: latitude (ϕ), which is zero at the equator and increases northward; longitude (λ), which increases eastward from zero longitude

(Greenwich, England); and vertical z, which is defined as positive upwards, with zero at the surface of the ocean.

Constants used throughout are: Boussinesq density $\rho_o = 1035$ kg m^{-3}; acceleration due to gravity $g = 9.806$ m s^{-1}; mean radius of the earth $R = 6371 \times 10^3$ m; k is the vertical diffusivity; and the coriolis parameter $f = 2\Omega \sin\phi$, where $\Omega = 7.292 \times 10^{-5}$ s^{-1} is the angular velocity of the Earth.

Variables are: potential temperature θ; salinity s; longitudinal velocity u; latitudinal velocity v; time t; the velocity field $\mathsf{u} = (u, v, w)$; pressure P; the frictional terms $F^{u,v}$; and the diffusive terms $F(s, \theta)$, which include vertical and isopycnic mixing.

MOMA has an explicit free surface scheme, which allows vertical movement of the top of the surface layer. This is important for accurate modelling of the barotropic wave response. Barotropic waves are able to propagate naturally. In a rigid lid model the surface is not permitted to move vertically. Instead barotropic waves are seen as pressure against the rigid surface. Gravity waves propagate at infinite wave speed under rigid lid conditions, and the velocity of other barotropic waves, such as the Rossby wave, is also affected. Details of the explicit free surface scheme used within MOMA have been comprehensively documented by *Griffies et al.* (2001).

2.1.3 Vertical coordinates

The choice of which vertical coordinate system to use is fundamental. The Z-layer, or depth-level, vertical coordinate system is used in both MOMA, the ocean component of FORTE, and the HadCM3 ocean, which are both used in this thesis. In this system each level is fixed at a set depth, usually with several layers near the surface, and progressively increasing in thickness with depth. This coordinate system performs well in the surface layers where there is high resolution and strong wind-driven mixing. It is less successful at depth. Below the mixed layer the ocean water masses tend to follow isopycnals. The design of the Z-layer coordinates results in excessive diapycnal mixing and there are problems with mixing at channel outflows such as the Gibraltar Strait.

Alternative depth coordinate systems include terrain following (σ-coordinates) and isopycnic coordinates. In σ-coordinate models the depth of the levels is scaled between the surface and the bottom of the ocean. The levels near the bottom strongly follow the contours of the bottom topography. Levels nearer the surface are less strongly influenced by the bottom topography. In isopycnic coordinate models the depth layers follow density contours. There are significant improvements at depth, with no spurious diapycnal mixing, but resolution in the

surface mixed layer can be poor, and outcropping of the isopycnal layers through the surface leads to problems with mixing in the surface waters. To counteract these problems the Z-layer and isopycnic coordinate systems have been merged to produce a hybrid depth coordinate. In this system Z-layer levels are fixed for the surface 100 m or so. Below this they are relaxed to isopycnic coordinates. This system provides good resolution in the mixed layer and allows ocean water masses to follow isopycnals at depth. It is not yet clear whether hybrid coordinate ocean models give substantially improved results over Z-layer models.

2.1.4 The Ocean Grid

Numerical models solve the equations of motion on a grid. The simplest form of ocean grid is to use a fixed grid array with uniformly sized boxes, although several variations on this basic configuration exist. Higher resolution regions may be nested within the standard grid to enhance areas of interest, whilst maintaining much of the computational advantage of the lower resolution model. Some models use a standard grid with a rotated pole patch (eg CHIME (Coupled Hadley Isopycnic Model Experiment)) to eliminate the need for polar islands, which are otherwise essential prevent a singularity due to convergence of the grid lines. There are also models which employ adaptive grid meshes, such as ICOM (Imperial College Ocean Model), which is currently under development. The models used for this thesis only employ a fixed grid array.

There are a number of different rigid grid configurations. Parameters are offset by half a grid point to enable easier and faster integration whilst minimising errors. *Arakawa* (1966) discusses the benefits of different staggered grid configurations. In total there are 5 Arakawa grid configurations, labelled 'A' to 'E'. The Arakawa 'B' grid is by far the most commonly used format for Z-layer (or depth level) coordinate models. The Arakawa 'C' grid is commonly used for isopycnic (density level) models. In the fixed grid system the size of the grid boxes determines the model resolution. This is often given in degrees, which means that grid box size (in metres) depends on latitude and may cause problems with model stability, as discussed later.

Both HadCM3 and the MOMA model used in subsequent chapters utilise the Arakawa 'B' grid (Figure 2.1). The Arakawa 'B' grid is well suited for the intended use of MOMA, which was designed to run quickly on a fairly coarse resolution grid.

Geostrophy is better simulated on the 'B' grid due to the co-location of the velocity points. The 'C' grid also has a tendency to suffer worse from 'checkerboarding' at low resolutions. Side boundaries on the 'B' grid are

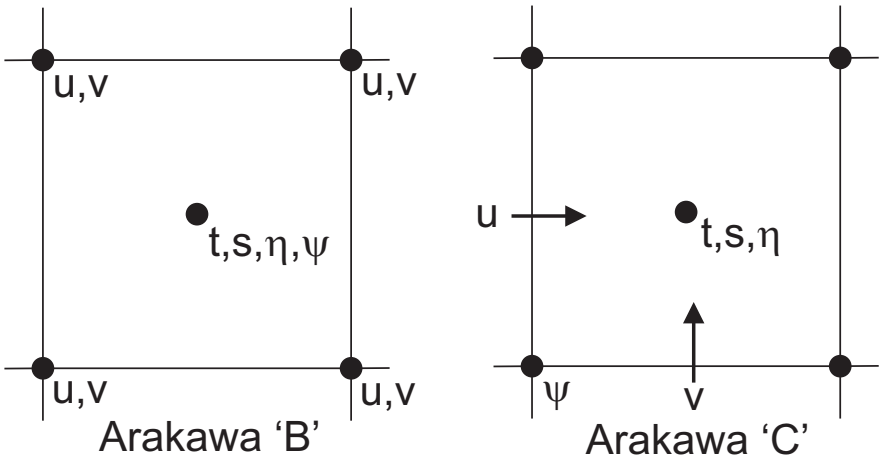

Fig. 2.1: Schematic showing the Arakawa 'B' and 'C' grids. Temperature (t), salinity (s), velocities (u,v), free surface height (η), and stream function Ψ are solved on an array of staggered grids, offset by 1/2 a grid point as illustrated.

naturally implemented using a no-slip condition, since both velocity points lie on the solid boundary. Narrow channels are better simulated on the 'C' grid, since they need only be 1 grid point wide to allow flow. The 'C' grid is also ideal for modelling gravity waves. Problems arise when coriolis is introduced because fv is calculated at a different point to fu (*Adcroft et al.*, 1999). This problem does not arise for 'B' grid models.

2.2 Model Stability

An important consideration when running all numerical models is numerical stability. There are several criteria that determine the stability of the model, and it is important to ensure that all relevant criteria are met.

Unstable model integrations can rapidly produce highly unrealistic values, which often results in the model integration failing. If the instability is less serious models can develop 'checkerboarding', where two grid point waves create a checkerboard effect with unrealistic, and sometimes large, differences between values occupying adjacent boxes. MOMA has a routine to filter checkerboarding, which reduces the problem considerably. Some parameters, most notably the Free Surface Height (FSH), are more sensitive to checkerboarding due to the construction of the numerical scheme.

2.2.1 The CFL condition

The first condition to consider is the CFL condition (Courant, Friedrich and Lewy). The CFL condition limits the timestep such that:-

$$\Delta t < \frac{\Delta_{min}}{v_{max} + c_{max}} \tag{2.8}$$

where Δt is the timestep, Δ_{min} is the minimum grid spacing, and v_{max} and c_{max} are current and wave velocity respectively.

MOMA requires both a barotropic and a baroclinic timestep. For the 1st baroclinic wave c_{max} is 3 m s^{-1}. A conservative value for v_{max} would be 15 m s^{-1}. This value is $\sim$10 times larger than currents found in the real ocean. It takes into account the localised increase in velocities that occurs during perturbation events and spin-up from a static basin, where initial currents can be large. For the case of the 1° idealised basin described later, Δ_{min} at 70°N is 38 km. The CFL condition provides a maximum baroclinic timestep of $\sim$2000 seconds. The barotropic timestep is two orders of magnitude smaller, since c_{max} is $\sim$100 times larger.

2.2.2 Munk boundary layer

It is also important to properly resolve the *Munk* (1950) boundary layer. For this to occur the diffusion must be greater than a critical value described by:-

$$A_m > \beta \Delta_{max}^3 \quad \text{where} \quad \beta = \frac{1}{R}\frac{\partial f}{\partial \phi}. \tag{2.9}$$

Under-resolution of the Munk boundary layer is most apparent in the free surface height field. Resolving the layer requires a minimum of one grid point within the layer. However, spurious diapycnal mixing associated with tracer advection may be reduced by ensuring two or more grid points are within the layer (*Griffies et al.*, 2000).

2.2.3 Horizontal diffusivity criteria

Tracer timesteps are also limited by the horizontal diffusive terms (*O'Brien*, 1986). The criterion is described by:-

$$\Delta t^T < \frac{\Delta_{min}^2}{8 A_h} \tag{2.10}$$

where A_h = horizontal eddy diffusivity (m^{2}s^{-1}).

A similar condition arises for the momentum equations, limiting the velocity timestep by:-

$$\Delta t^v < \frac{\Delta^2_{min}}{8A_m} \tag{2.11}$$

where A_m = horizontal eddy viscosity (m^2s^{-1}).

In both cases the restriction ensures that any diffusion is limited to one grid spacing per timestep. This is necessary to prevent model instability occurring.

2.2.4 Grid point Reynolds number

The grid point Reynolds number is another criteria to be considered. It is worth noting that this criteria is not essential for stability, but once an instability develops two gridpoint waves will appear and will remain until this criteria is satisfied.

$$A_m or A_h > \frac{u\Delta_{max}}{2} \tag{2.12}$$

Thompson et al. (1985) have shown the classical derivation of the Grid point Reynolds number criteria to be incorrect. As an alternative criterion they suggest:-

$$\Delta t^v > \frac{2A_m}{u^2_{max}} \tag{2.13}$$

2.3 Resolving Kelvin waves

An understanding of how successfully models are able to resolve and correctly model dispersive characteristics and velocities of planetary waves is important for this study. Successful resolution of planetary waves is dependent on the horizontal resolution and the grid format. The Arakawa 'B' grid provides superior spatial representation of sub-grid scale planetary waves (where the Rossby radius of deformation is smaller than the grid spacing) compared with the Arakawa 'C' grid, although significant temporal distortion occurs. The 'C' grid, which is also commonly used in numerical models, is superior to the 'B' for well resolved waves, although in many cases the 'B' grid is still preferred due to its ability to better resolve spatially the higher modes of propagation. Finite difference Rossby waves have been shown to be represented better by the 'B' grid in both resolved and under-resolved cases (*Dukowicz*, 1995; *Wajsowicz*, 1986).

Horizontal resolution is very important for the accurate reproduction of planetary waves. A minimum of 2 grid points are required for resolving any wave in the ocean such as Kelvin waves, which extend a distance of one Rossby

Radius away from the coast. The barotropic mode can be well resolved even with a low resolution model due to the large Rossby radius (1600 km at 60° for a wave speed of 200 $\mathrm{m\,s^{-1}}$). A resolution of at least 1/8th degree is required to resolve the 1st baroclinic mode, since the Rossby radius is 16km at 60N (Figure 1.1). Such a high resolution is computationally unfeasible for this study. In the equatorial waveguide the Rossby radius increases to >100 km, which enables Kelvin waves to be resolved with a 1° grid resolution.

Hseih et al. (1983) discuss the problem of resolving Kelvin waves in Bryan-Cox numerical models. They show how Kelvin waves are affected by model resolution, with well resolved waves (i.e. grid scales smaller than the Rossby radius) producing more accurate spatial representations and velocities closer to theory. Evolution of a Kelvin wave dispersion from a high latitude anomaly is shown for 3 different resolutions in an idealised MOMA basin (described in detail in chapter 4) (Figure 2.2). Kelvin wave velocity is significantly reduced in the 2° and 1° resolution models (Figure 2.2, a) – d)), where the Kelvin wave is poorly resolved, compared to the 1/4 degree resolution model (Figure 2.2, e) – f)). The spatial representation of the Kelvin wave is reasonable in all models, and it is clear that fine detail improves with resolution. The Kelvin wave velocity in the 1/4° model is approximately 1 $\mathrm{m\,s^{-1}}$, so the green curve in Figure 1.1 corresponds to the Rossby radius for these experiments. The largest affect of resolution on Kelvin wave velocity is between the well resolved case (1/4°), in which the Kelvin wave propagates at 0.85 $\mathrm{m\,s^{-1}}$, and the under-resolved case (1°), in which the Kelvin wave propagates at 0.4 $\mathrm{m\,s^{-1}}$. Once the Kelvin waves are under-resolved (1°) the velocity is more constant, and with a further reduction of resolution to 2° the speed of the propagating Kelvin wave reduces slightly to 0.32 $\mathrm{m\,s^{-1}}$. Discrepancy between the Kelvin wave velocity in the well resolved (1/4°) model and theory is attributable to the viscosity used in the model. The effects of viscosity on the speed of wave propagation are discussed in *Hseih et al.* (1983). The large extent of 'checkerboarding', or two grid point waves, in the 2° model shows that it suffers worst from poor resolution of the Kelvin waves. The 1° model shows a very similar evolution of the spatial structure of the wave response when compared to the 1/4° resolution model (Figure 2.2 f), Figure 2.3), although it takes twice as long to reach this stage compared to the 1/4° model.

For the purpose of this study it is computationally unfeasible to run a 1/4° model for all experiments, due to the long spinup time required to reach a steady state. It must also be noted that although the 1/4° model is able to resolve the first baroclinic mode waves at high latitudes, higher baroclinic modes will be under-resolved. The extensive two grid point wave response of the 2° model is not desirable, especially for the static basin experiments planned later where there will be no external forcings to damp them. However, the 2° model is capable of

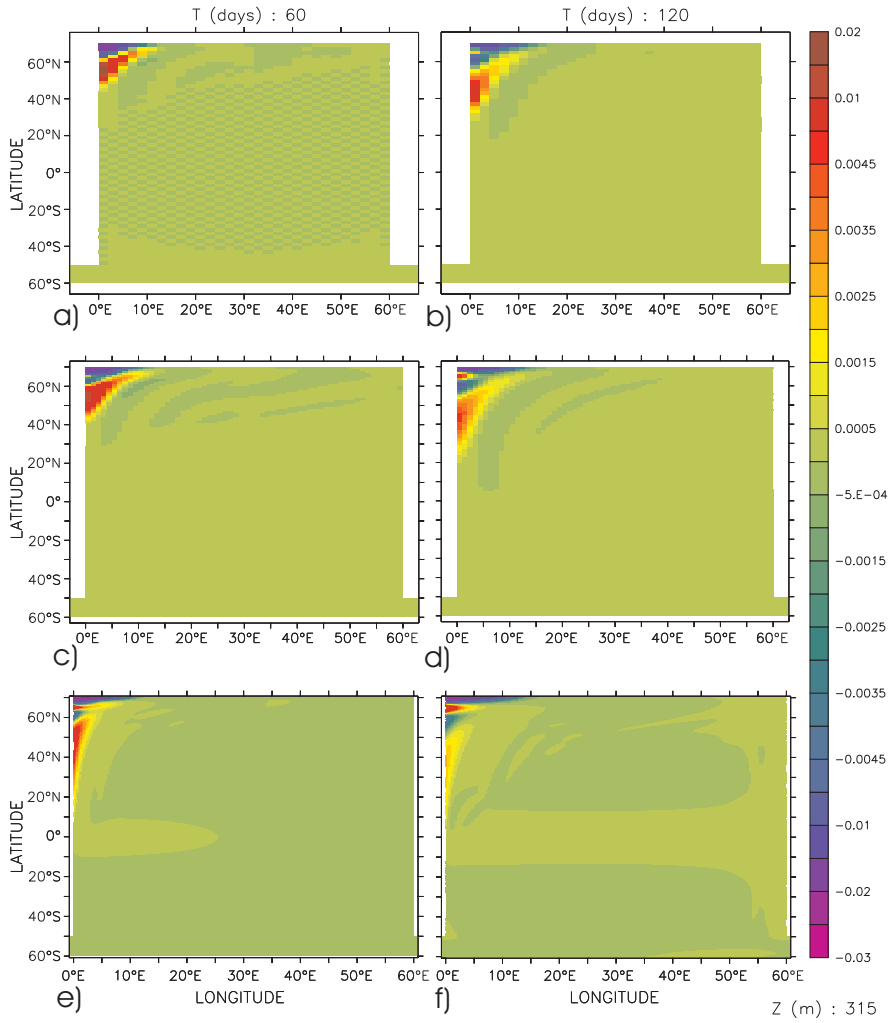

Fig. 2.2: Comparison of temperature anomalies (°C) at level 5 for 2° (a),b)), 1° (c),d)), and 1/4° (e),f)) resolutions after 60 days (left) and 120 days (right) of model integration.

producing a reasonable spatial representation of the wave response and therefore there will be confidence in the FORTE results presented later, although the time for the wave response to the anomaly will be considerably retarded. For the MOMA experiments a resolution of 1° will be used. Although wave velocity is considerably slower than theory, the spatial representation of the response is acceptable.

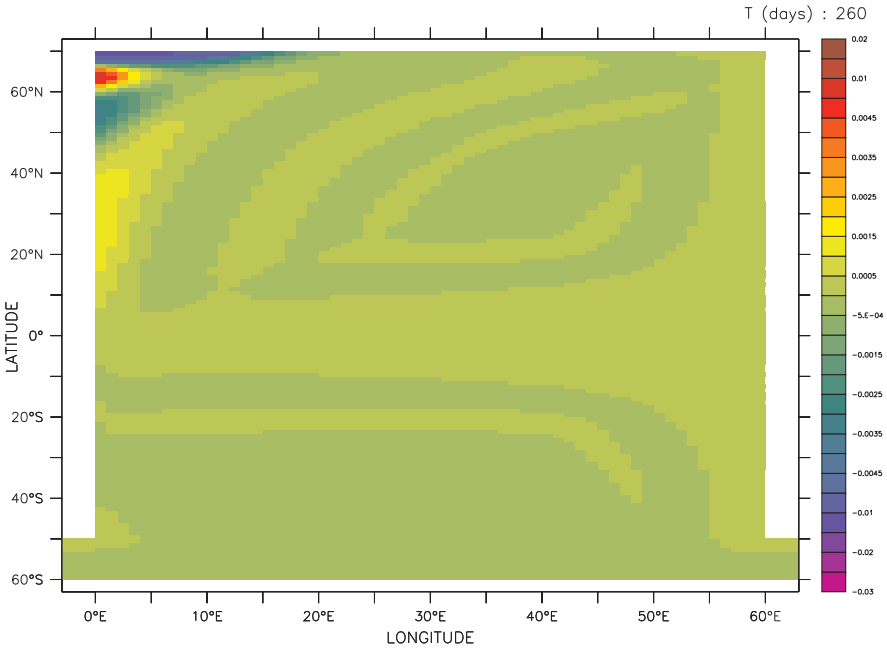

Fig. 2.3: Temperature anomaly response (°C) of the 1° static MOMA model after 260 days.

Chapter 3

The Tropical Atlantic Dipole in HadCM3

3.1 Introduction

One obvious flaw in many of the previous studies which have attempted to identify the TAD is the use of a short (30 – 40 year) dataset to try and identify decadal signals. The range of results suggests that the TAD may occur on a slightly longer than decadal timescale. For studies using only a 30 year dataset this means that there would be no more than 2 complete cycles of the dipole, which is close to the limit of frequency analysis. The use of short timeseries also means that very little confidence can be given to this frequency analysis.

The easiest solution to this problem is to use a longer dataset. Observational datasets are typically short due to the relatively short time for which observational methods enabling regular temporal and spatial sampling have been available, the primary one now being satellites. In situ measurements date back over 100 years, but they are very limited both spatially and temporally due to their dependence on shipping. Numerical model output provides us with a comprehensive and complete dataset, regularly sampled over the whole ocean for substantial lengths of time. Another key advantage of model output is that it is possible to retrieve parameters from anywhere within the model. This allows us to see the ocean interior in the same detail as we can see the surface, something observational techniques currently have no answer for. There are obvious provisos regarding the numerical model's ability to accurately reproduce the real ocean, and whether or not it is capable of modeling events such as the TAD.

A 100 year dataset from HadCM3, the UK Met Office's coupled climate model, is examined for evidence of the Tropical Atlantic Dipole. The HadCM3 model

Level	Depth (m)	Thickness (m)
1	5.0	10.0
2	15.0	10.0
3	25.0	10.0
4	35.1	10.2
5	47.9	15.3
6	67.0	23.0
7	95.8	34.5
8	138.9	51.8
9	203.7	77.8
10	301.0	116.8
11	447.1	175.3
12	666.3	263.2
13	995.6	395.3
14	1501.0	615.0
15	2116.0	615.0
16	2731.0	615.0
17	3347.0	615.0
18	3962.0	615.0
19	4577.0	616.0
20	5193.0	616.0

Table 3.1: Vertical levels in HadCM3's Ocean.

dataset provides a complete record of all fields of interest in the ocean and atmosphere at all depths for a period of 100 years, sufficient to begin confidently resolving the decadal cross-equatorial SST dipole. EOF and complex EOF analysis are applied to the depth levels within the model to separate patterns of variance from the data, and correlations of EOF timeseries from atmospheric fields and the different levels within the ocean are calculated.

3.2 HadCM3 and data

HadCM3 is the Hadley Centre's flagship model. It was developed in 1998 to succeed HadCM2. The details of the model are described by *Gordon et al.* (2000) and *Pope et al.* (2000). A significant distinction of HadCM3 from other coupled GCMs is that HadCM3 does not require flux adjustment (artificial heat/freshwater fluxes) to produce good simulations.

The ocean is a primitive equation model based on *Cox* (1984), utilising an Arakawa 'B' grid. It has a horizontal resolution of 1.25° x 1.25°, with 20 vertical Z-levels (Table 3.1). The ocean component employs a *Gent and McWilliams* (1990) mixing scheme and a rigid lid approximation.

The atmosphere has a horizontal resolution of 2.5° (lat) x 3.75° (lon), comparable

to a T42 spectral model. There are 19 vertical levels using a hybrid vertical coordinate system. Exchanges between the ocean and atmosphere components occurs daily.

The dataset used for this study was the 100yr COAPEC HadCM3 control integration, which was configured to run with pre-industrial CO2 levels (280 ppmv). Integration of the model from initial temperature and salinity conditions from *Levitus and Boyer* (1998); *Levitus et al.* (1998), and zero ocean velocity globally, for 400 years prior to the COAPEC run provides a stable climate close to reality with SST drift less than 0.01°C/century.

3.3 Data Analysis

Anomaly data is created by removing monthly means, which are averaged over the 100 year integration. This process removes the mean seasonal cycle from the data. A 3rd order 8 year low-pass butterworth filter is applied to the data, which removes all high frequency signals (seasonal and interannual) from the data, leaving only frequencies with periods greater than 8 years. Use of an 8 year low-pass filter allows analysis of the decadal modes of variability in the dataset. It is not necessary to use a bandpass filter on this 100 year dataset since an upper limit is naturally implemented at 50 years. It was found that imposing an upper limit at 20 years had little effect on the results. The first and last 4 years of the data were discarded to remove errors introduced by the filter. Filtering reduces the variance in the data considerably (Figure 3.1), with the greatest effect in coastal regions and along the equator where high frequency variability, such as the seasonal cycle dominates. Along the equator the effects of the seasonal cycle are significant as the ITCZ migrates north and south. The presence of the land and the shallow shelf seas influence the frequency spectrum in the coastal regions, giving more energy to seasonal and interannual timescales. In the basin interior, where the dipole maxima are located, around 30% of the variance remains.

3.3.1 Analysis methods

EOF (Empirical Orthogonal Function) analysis is a mathematical way of breaking information down into patterns of variance. Instead of the data being created from N separate samples in time, it can be built from spatial structures, or modes, that change in amplitude over time. For this work the EOFs were calculated using singular value decomposition. The data, Z, is organised into a matrix where the rows are temporal evolution of the columns, which each represent a single data point. Singular value decomposition breaks the data, Z, into 3 matrices:-

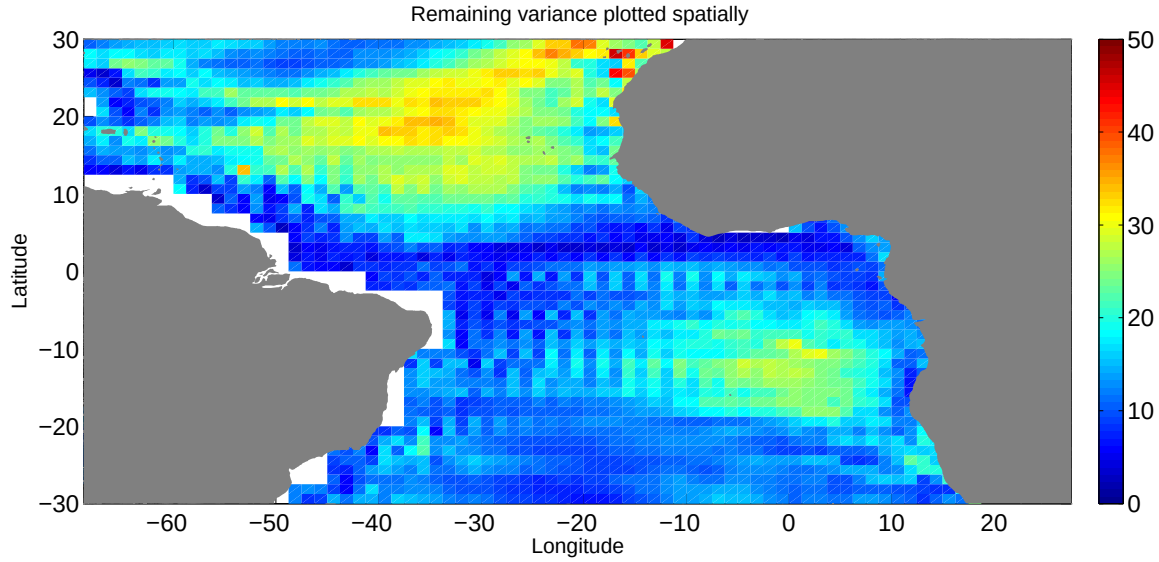

Fig. 3.1: Percentage of variance remaining (%) after application of the 8 yr low pass Butterworth filter to the tropical Atlantic SST from the COAPEC 100 yr HadCM3 dataset.

$$Z = U * D * V^t \tag{3.1}$$

where matrices U and V are orthonormal and matrix D is diagonal. The EOFs are contained in matrix V, whilst the timeseries for each EOF is computed by $U * D$.

EOF analysis is a reliable way of separating out signals with different spatial patterns, or that act on different timescales. In a typical dataset a large proportion of the variance can be explained with only a few EOFs. The method is also commonly used in data compression to reduce the amount of data necessary, whilst still retaining most of the information. When used for data analysis typically only the first few EOFs are of any significant interest. Beyond these the variance accounted for is small, so any patterns can be considered insignificant compared to the larger EOFs. EOFs where the percentage of variance explained is low and/or not significantly different to subsequent EOFs should be considered with caution as they are unlikely to show real patterns of variance. EOF analysis deals with the data mathematically, and as a result the patterns of spatial variance produced do not necessarily relate to any real phenomenon.

Great care has to be taken when interpreting EOFs. There has been much discussion in the literature over the correct interpretation of EOF results. *Dommenget and Latif* (2002) argue that attempts to show physical climatic processes such as the "Tropical Atlantic Dipole" and the "Tropical Indian Ocean Dipole" have resulted in false results due to the incorrect interpretation of EOF analysis. Their point is highlighted by a simple low-dimensional example. They show that it is possible to produce a dipole through EOF analysis that is purely an artifact of the orthogonality constraint. This argument was contested by

Behera et al. (2003) on the grounds that Dommenget and Latif's synthetic example modes explained near-identical amounts of variance. It is well known from *North et al.* (1982) that in such situations EOF analysis will lead to degenerate modes. However, it must be noted that in this case, as explained by *Dommenget and Latif* (2003) that the arguments presented by *North et al.* (1982) are not applicable. Degeneracy occurs only when statistical uncertainties are present, such as analysis of a finite timeseries. This results in uncertainties in the covariance matrix, which leads to uncertainties in the EOF eigenvalues. The synthetic dataset used for the simple low-dimensional example in *Dommenget and Latif* (2002) is absolutely accurate and contains no statistical uncertainties.

EOFs showing degenerate modes may be recognised as two patterns which carry approximately equal weightings of variance. Considering the fact that the tropical Atlantic is likely to be influenced by several competing signals of comparable strength, these papers highlight the level of caution needed in analysing and interpreting data. Careful filtering of unwanted signals will help ensure that erroneous conclusions are not drawn. EOFs showing degenerate modes can also occur when trying to analyse a propagating signal. EOF analysis is only able to identify stationary patterns of variance. If the data being examined is known to contain propagating signals it is better to proceed using complex EOF analysis.

Complex EOF analysis is a similar process to EOF analysis. Before the EOF analysis is applied a Hilbert transform of the data is carried out. Complex EOF analysis extracts propagating signals by recording both the amplitude and the phase of the signals. The technique can provide information on how EOF patterns change and move over time. The amplitude component of the complex EOF shows similar patterns to a standard EOF. The phase component indicates change in the pattern shown by the amplitude component. If the phase component is uniform over the area it suggests a stationary pattern. Change in the phase component shows propagation of the pattern shown by the real component. Visualising the evolution of a propagating signal indicated by the complex EOF analysis is difficult, so creating animations of the complex EOF images by multiplying them by their corresponding time series is a much easier way of visualising the data. Distance-Time (Hovmöller) plots are the conventional way of identifying propagating signals, but these only provide a two dimensional picture of how a signal may be evolving. Animating the complex EOF results can be very beneficial, enabling easy observation of the evolution of spatial patterns.

Before performing the EOF and complex EOF analysis the data were normalised by dividing each time series by its standard deviation, and detrended by removing a line of best fit of the form $y = mx + c$. This process removes model drift from the dataset, preventing it from appearing as a low frequency EOF

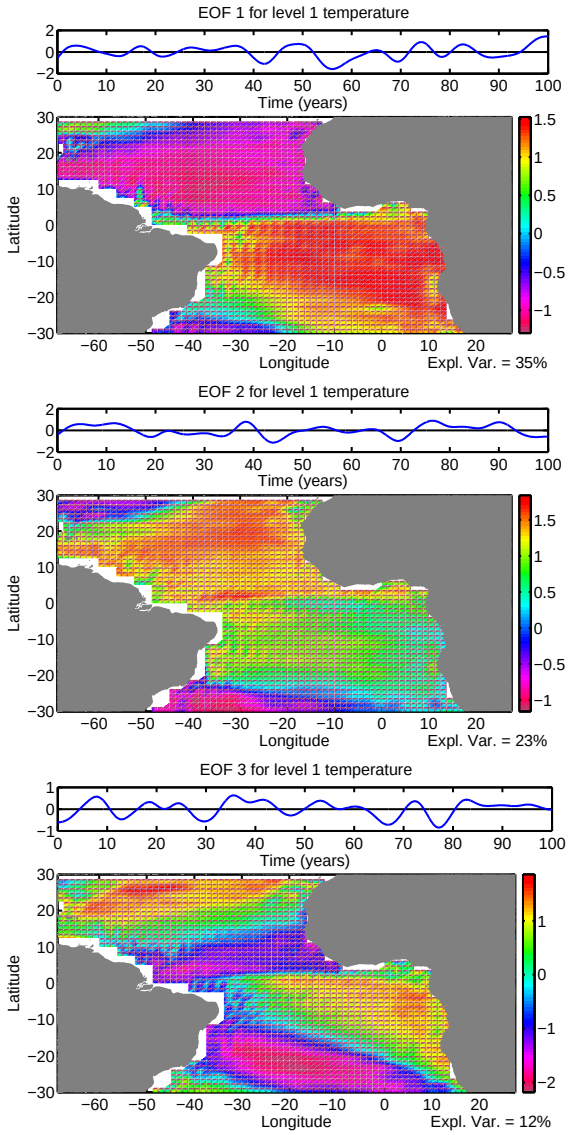

Fig. 3.2: First three EOFs of the level 1 (5 m) temperature field in the tropical Atlantic from the COAPEC 100 year HadCM3 dataset.

pattern.

3.4 Results

3.4.1 Spatial analysis

EOF (Empirical Orthogonal Function) analysis of the level 1 temperature shows a cross-equatorial dipole structure (Figure 3.2). The first mode, accounting for 35% is well separated from the second (23%) and third (11.5%).

Levels 2, 3 and 4 all show very similar patterns to level 1. This result is not unexpected because the surface layers are subject to significant wind mixing. At level 4 an interesting feature starts to appear (Figure 3.3). A curve, starting

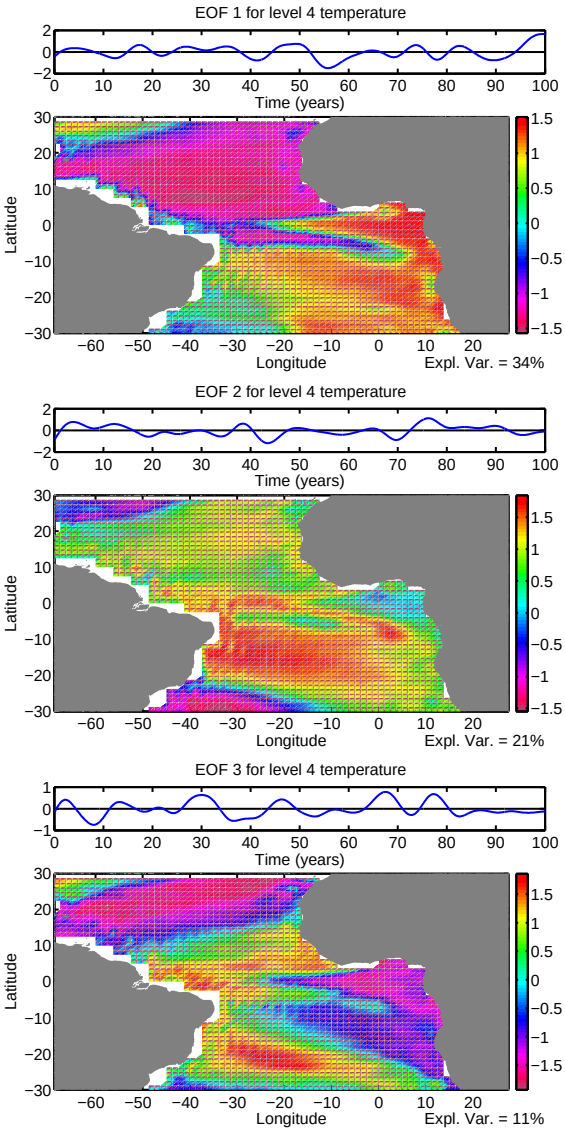

Fig. 3.3: First three EOFs of the level 4 (35 m) temperature field in the tropical Atlantic from the COAPEC 100 year HadCM3 dataset.

close to the equator in the western side of the basin and extending southward to around 10° at the eastern side of the basin, appears. The shape is similar to the pattern produced by a westward propagating Rossby wave, which can be seen in the previous chapter (Figure 2.3). Some hint of this curve is present in level 3 towards the western side of the basin. The curve becomes more prominent with depth, being shown most clearly at level 7 (Figure 3.4). In all cases the explained variance of the first EOF is distinct from the second and third.

Heat content was calculated for the upper 500 m and also for the full ocean depth. Results of the EOF analysis of the two fields are very similar, and the variability can be seen to exist predominantly in the surface waters. The results are very similar to the EOFs of SST, and it is clear that this approach reveals nothing new. The considerable difference in the surface and subsurface EOFs shows that two very different responses are occurring.

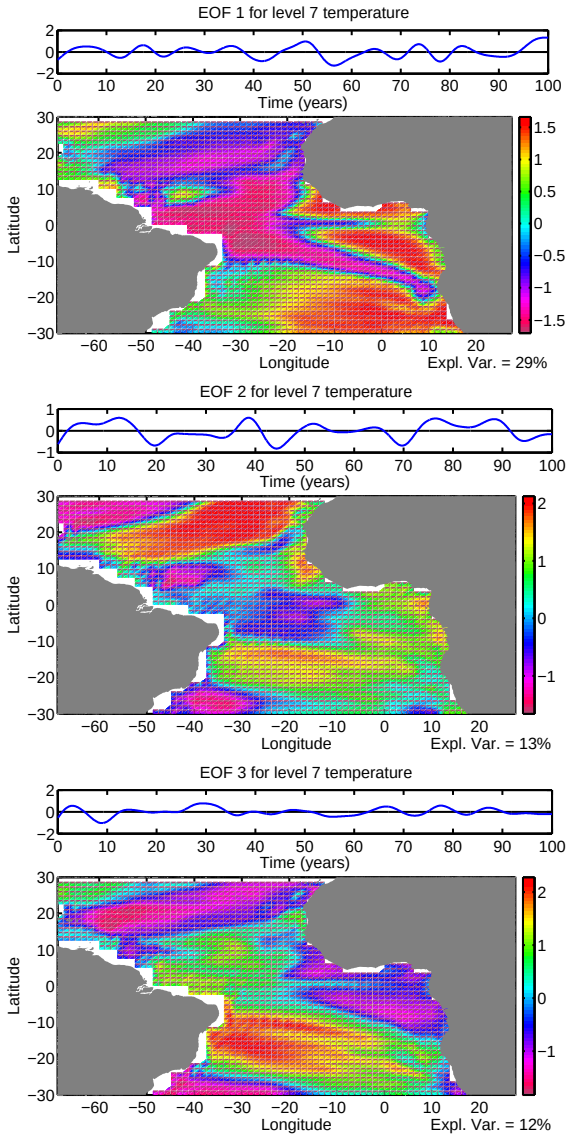

Fig. 3.4: First three EOFs of the level 7 (96 m) temperature field in the tropical Atlantic from the COAPEC 100 year HadCM3 dataset.

A Rossby wave shaped curve, which is a result of the dependence of wave speed on latitude, is visible in the EOF analysis of temperature in the subsurface levels, which suggests that a method of analysis able to resolve propagating signals would be beneficial.

Complex EOF analysis shows an almost identical pattern in the level 1 temperature (Figure 3.5). The first mode accounts for 41.5% (6.5% more than EOF analysis). Animation of the first mode reconstructed in time clearly shows that the signal is stationary. There is virtually no horizontal movement of the signal throughout the entire time series. The increase in explained variance is due to small movements and changes in the shape of the pattern being permitted.

Levels 2, 3 and 4 again show the same stationary pattern as the surface. At level 4 the Rossby wave like curve appears (Figure 3.6). The pattern can be seen most clearly, again, at level 7 (Figure 3.7). The Rossby wave like curve propagates from

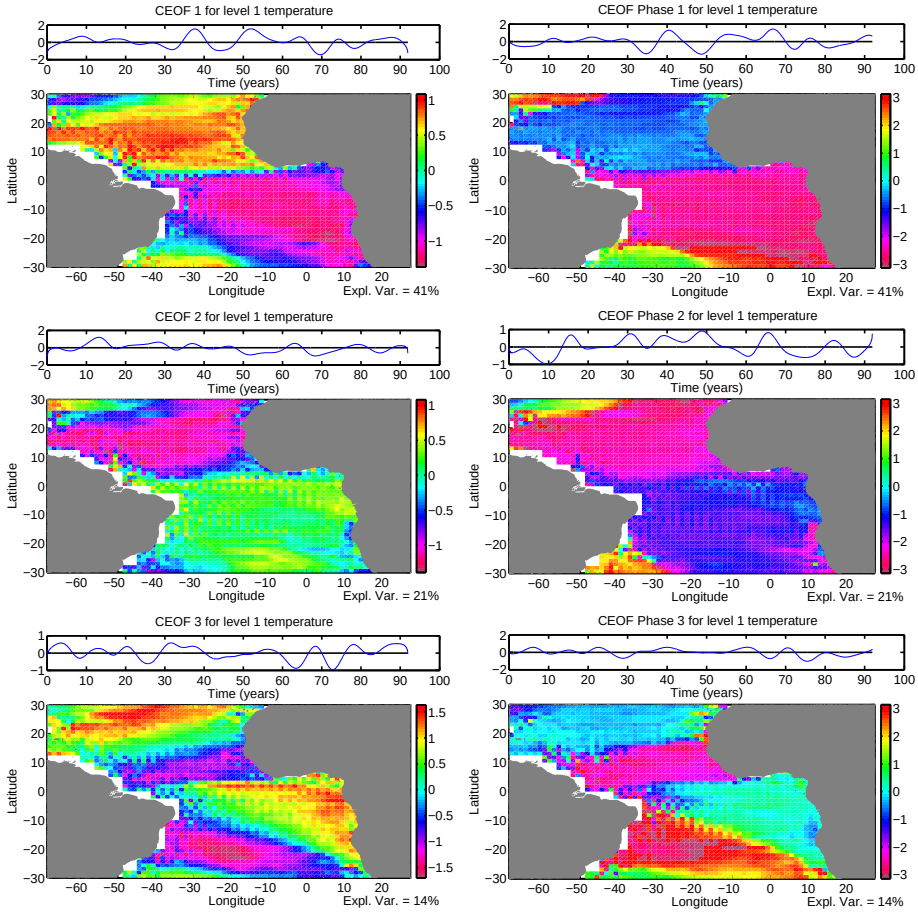

Fig. 3.5: Amplitude (left) and phase (right) components of first three complex EOFs of the level 1 (5 m) temperature field in the tropical Atlantic from the COAPEC 100 year HadCM3 dataset.

east to west. Animations of the reconstructed complex EOFs show this clearly. The wave is very slow, with velocity of approximately 1.5 cm s^{-1} it crosses the basin in about a decade. A first baroclinic Rossby wave propagating outside the equatorial waveguide would be expected to propagate with a velocity of 0.3 m s^{-1} (*Killworth and Blundell*, 2003), which would cross the Atlantic basin in 6 months. Some retardation of the wave speed would be expected due to the 1.25° horizontal resolution, which will only just resolve propagation in the equatorial waveguide, and also the necessarily high viscosity used in the model. However, this cannot account entirely for the difference between the observed and modelled wave velocities measured here, which suggests that the observed propagation in the model is either a higher mode, where wave speeds can be of the order of a few cm/s, or that it may be a forced wave propagation.

3.5 Atmospheric variables

The tropical ocean and atmosphere interact closely. The high sensitivity of the atmosphere to small changes in SST enables feedback processes to begin. Positive

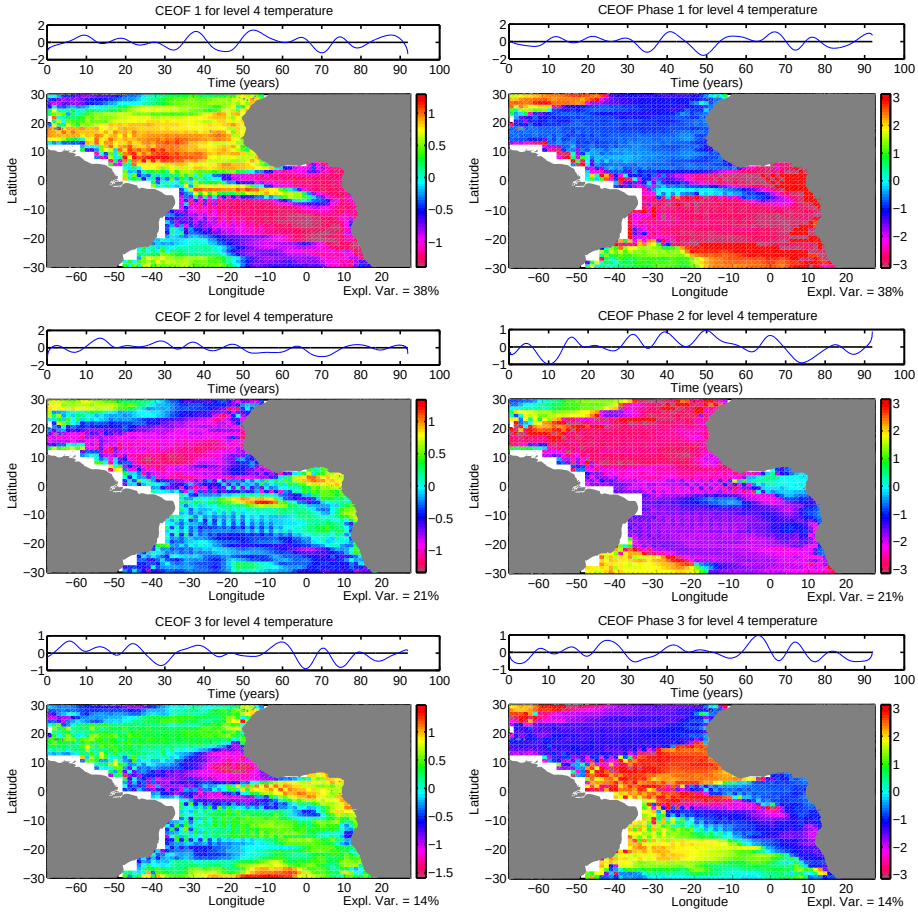

Fig. 3.6: Amplitude (left) and phase (right) components of first three complex EOFs of the level 4 (35 m) temperature field in the tropical Atlantic from the COAPEC 100 year HadCM3 dataset.

feedback between the ocean and atmosphere can result in strong anomalies which persist, and may influence other climate phenomena such as the NAO. Complex EOFs of the main atmospheric variables are shown here.

Complex EOFs of relative humidity show very little structure (Figure 3.8). The first EOF explains only 22% of the variance and shows variability about the equator, with no coherent structure off the equator. This signal may be weak evidence of decadal variability in the location of the ITCZ. Complex EOFs 2 and 3 show no obvious structure.

Complex EOFs of sea level pressure show strong dipolar patterns (Figure 3.9). The phase component of complex EOF 1 shows the signal to be stationary. The phase component of the dipole in complex EOF 2 shows that the signal to be propagating.

The surface air temperature complex EOFs are fairly noisy, but the first (34%) does show some evidence of a cross-equatorial dipole (Figure 3.10). The time series shows it to be more active in the second half of the century.

Complex EOF analysis of the zonal component of wind shows a clear dipole about the equator in the first complex EOF (Figure 3.11). The phase component

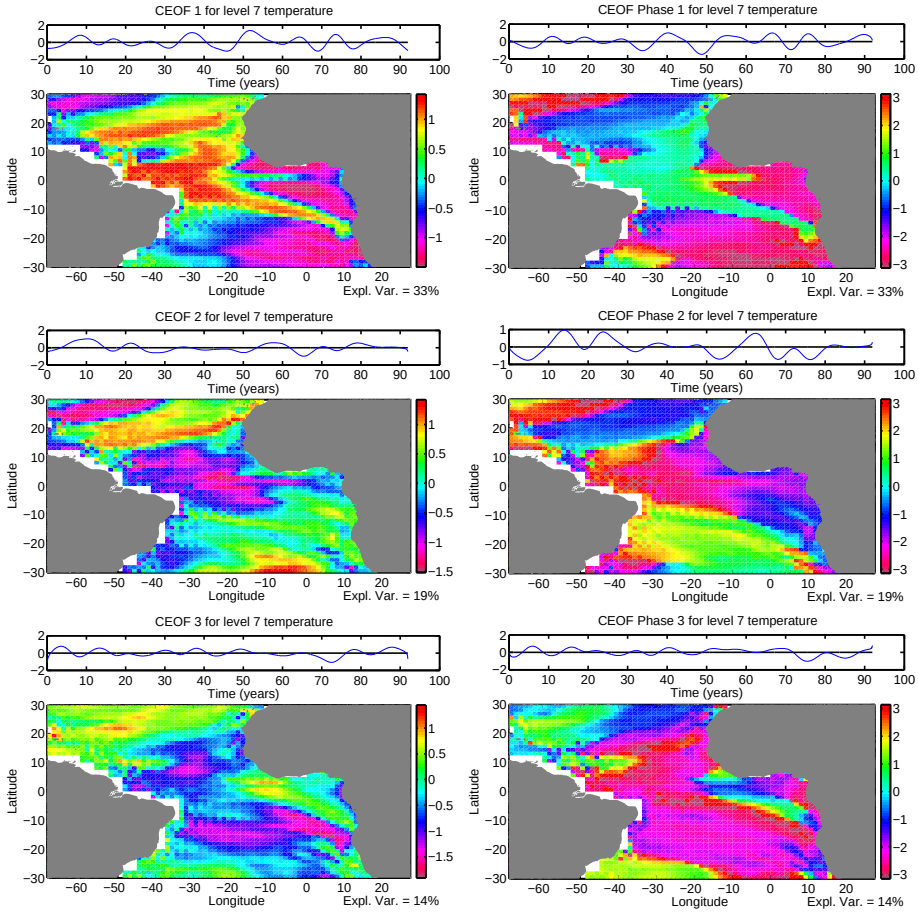

Fig. 3.7: Amplitude (left) and phase (right) components of first three complex EOFs of the level 7 (96 m)temperature field in the tropical Atlantic from the COAPEC 100 year HadCM3 dataset.

shows this to be propagating.

3.5.1 Correlation of EOF time series

In order to try and isolate the driving mechanism, cross correlation was performed on the time series from the complex EOF analysis on the atmospheric variables and the ocean temperature fields.

Cross correlation of the subsurface temperature fields with SST suggests that the signal originates from depth (Figure 3.12). Level 10 (350 m) leads the SST by 22 months, whilst level 7 leads the SST by 6 months. Interestingly, at level 5 the signal lags the SST by 7 months. The signal in the surface layers (levels 1 to 3) is coherent, arriving at the same time. It is possible that wind mixing at the surface rapidly distributes the upwelling signal over a larger area, resulting in the maximum correlation in the surface layers occurring before the maximum correlation at level 5. The complex EOF analysis shows that once the signal reaches the surface mixed layer it is rapidly mixed. The maximum lag at level 5 could also suggest that atmospheric signals are influencing the surface mixed

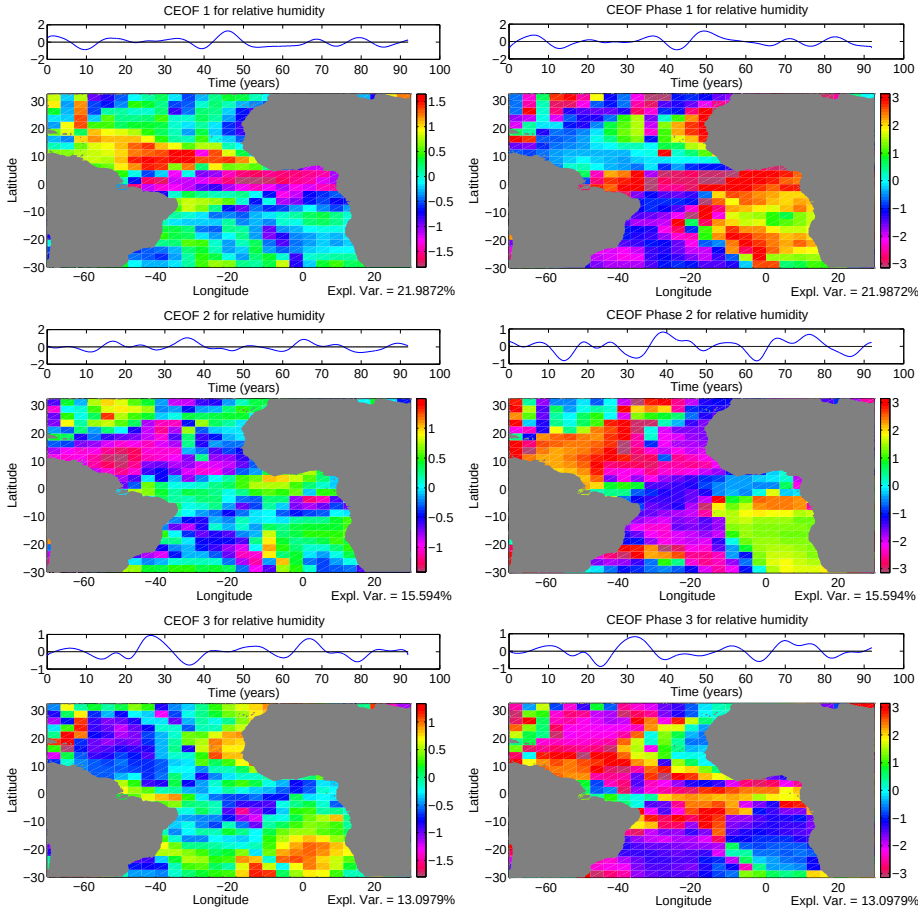

Fig. 3.8: Amplitude (left) and phase (right) components of first three complex EOFs of surface relative humidity in the tropical Atlantic from the COAPEC 100 year HadCM3 dataset.

layer.

Several ocean and atmosphere fields (SST, Ocean temperature at levels 4 and 7, SAT, Meridional wind velocities) show strong decadal dipole signals between years 30 and 60. Cross correlation of this time period gives almost identical results to the full time series analysis for the subsurface temperature layers in the ocean (Figures 3.12,3.13), but the results differ much more for the atmospheric variables (Figures 3.14,3.15). This indicates that the ocean temperature correlations are dominated by the strong signal seen at this point in the time series, but that the atmospheric variables are not so strongly dominated by the signal at this time. If the correlations are strongly dominated by the signal from a 30 year period, interpretation of the results must be considered carefully.

Cross correlation of the atmospheric variables shows the surface atmospheric temperature leading SST by 21 months. Meridional wind velocity is shown to lead by a further 6 months. However, sea level pressure lags behind SST by around 6 months. The maximum lead/lag times for the top 10 ocean layers and the atmospheric fields are illustrated in a schematic (Figure 3.16).

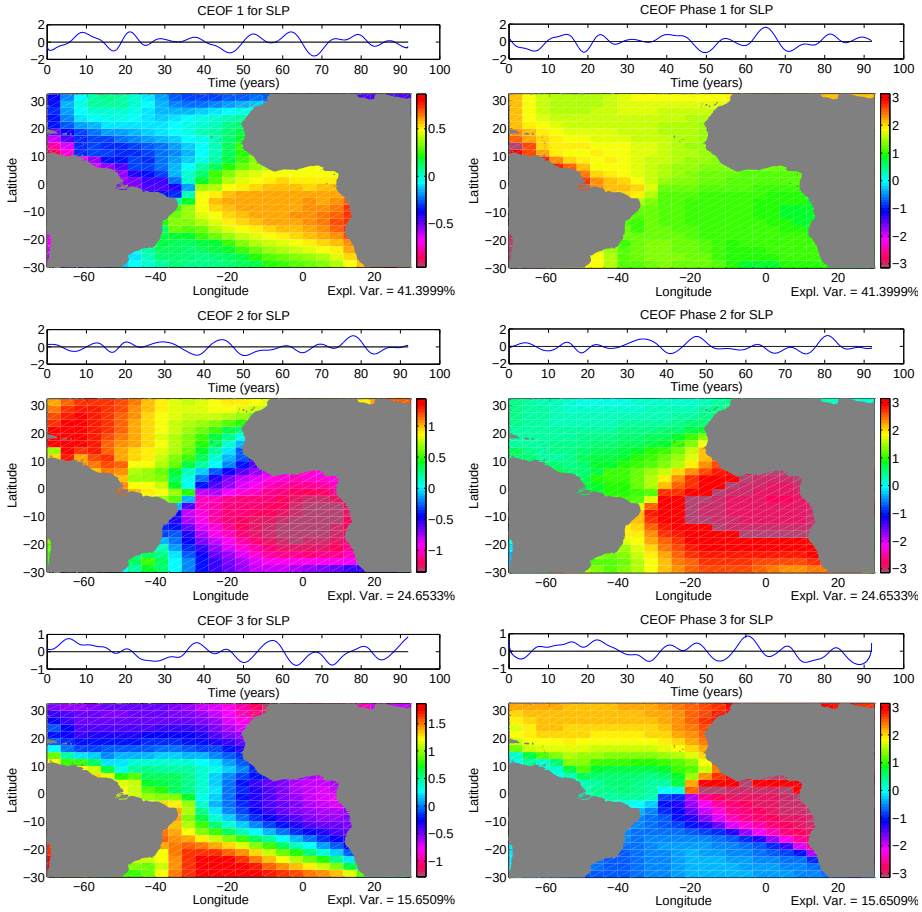

Fig. 3.9: Amplitude (left) and phase (right) components of first three complex EOFs of sea level pressure in the tropical Atlantic from the COAPEC 100 year HadCM3 dataset.

3.5.2 Vertical analysis

To confirm these findings, and get greater insight into the mechanisms involved, complex EOFs of vertical profiles were produced (Figures 3.17,3.18,3.19). These show the signal propagating from levels 8-10 upwards. The upper levels are readily mixed by the atmosphere so propagation of the signal from 50 m to the surface is very rapid, and not ideally resolved with the monthly model output.

Some instances of downward propagation from atmospherically induced surface anomalies occur, and the southern lobe of the NAO also affects the northern tropical Atlantic.

3.6 Discussion

Analysis of the tropical Atlantic in HadCM3 shows a cross-equatorial dipole structure in the surface mixed layer. The pattern, which is asymmetric at the surface becomes symmetric at depth and Rossby wave signatures are visible in the subsurface EOF and complex EOF analysis. The speed of these Rossby waves is very slow, at a few cm/s, suggesting that they are either a higher baroclinic

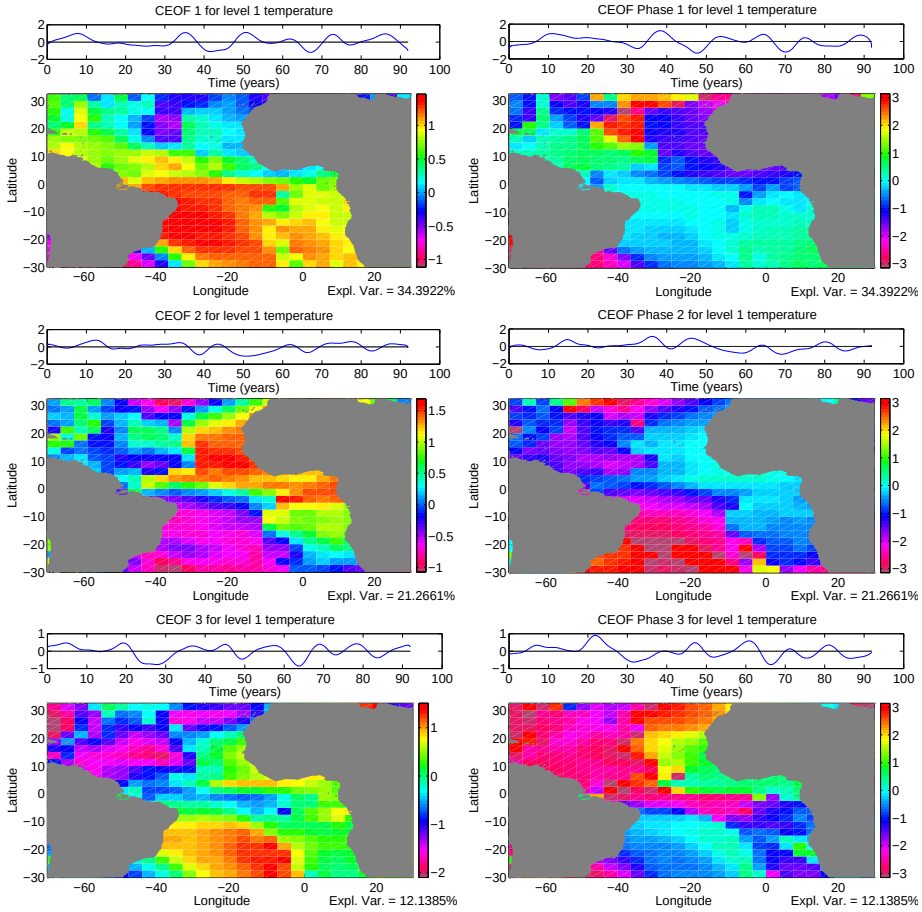

Fig. 3.10: Amplitude (left) and phase (right) components of first three complex EOFs of surface air temperature in the tropical Atlantic from the COAPEC 100 year HadCM3 dataset.

mode or a forced mode of propagation. The velocity of these waves will be slower than reality due to the resolution of HadCM3. From the vertical complex EOF analysis the Rossby waves can be seen to push the subsurface signal towards the surface as they pass, suggesting that the TAD is controlled by subsurface waves, which may have been initiated remotely by anomalous deep convection at high latitudes. Attempts to trace the path of the waves back from the equator to the high latitude North Atlantic were unsuccessful. Complex EOF analysis shows the surface signal to be almost stationary, with only slight variation in the dipole pattern seen along the equator and around the coastlines. Much more propagation appears in the subsurface in the form of Kelvin and Rossby waves. Lead/lag correlation of the ocean temperature EOFs and atmospheric variables shows that EOFs of some atmospheric variables lead the EOFs of temperature in the mixed layer by similar amounts as temperature EOFs at levels 8 and 9. The results of the cross correlation should be interpreted with care, since there are only 8 – 10 complete cycles of the decadal oscillation within the 100 year dataset. The similarity of the results obtained by analysing only the time period between 30 and 60 years compared to using the whole 100 year time series suggests that the results of the correlation are dominated by the two decadal cycles in this time

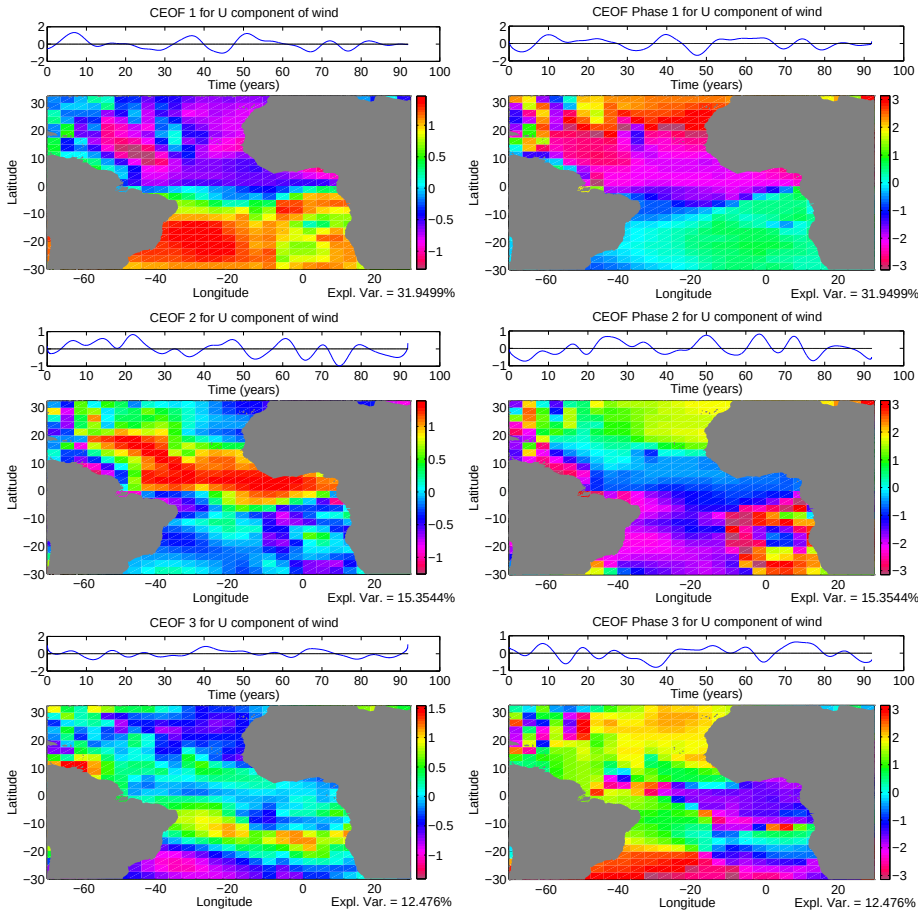

Fig. 3.11: Amplitude (left) and phase (right) components of first 3 complex EOFs of sea level zonal wind velocities in the tropical Atlantic from the COAPEC 100 year HadCM3 dataset.

period.

It is not obvious what is driving the subsurface Rossby waves. It is possible for coastally trapped waves to be generated by wind blowing across the surface of the ocean. This process could occur within the tropics or extra-tropics. An alternative suggestion is that Kelvin waves could be formed at high latitudes. *Dong and Sutton* (2002a) noted whilst investigating the effects of a sudden change in the THC in a modified version of HadCM3, the UK Met Office coupled climate model, caused by a large influx of freshwater into the northern Atlantic, that the model generated a cross-equatorial SST dipole oscillation in the tropical Atlantic. The triggering mechanism for the dipole is the southward propagation of Kelvin-like waves along the coast of N. America. The Kelvin waves are generated at the location of the high latitude sinking in the North Atlantic. Upon reaching the equator the Kelvin wave separates from the coast and follows the equator across the Atlantic to the west coast of Africa. Here the wave divides and travels both north and south along the coastline, generating Rossby waves which propagate into the interior of the ocean. This wave activity carries the signal much faster than advection, and the response from the initial wave generation

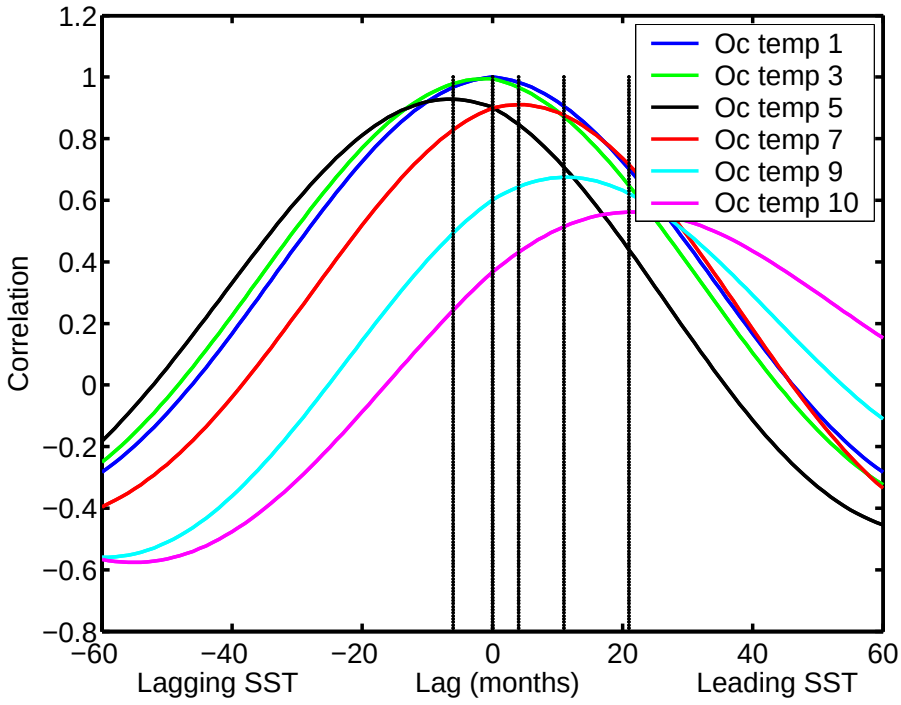

Fig. 3.12: Correlation of subsurface ocean temperature at model levels 3, 5, 7, 9 and 10 with SST for the complete 100 year time series. Autocorrelation of level 1 (SST) is included for reference.

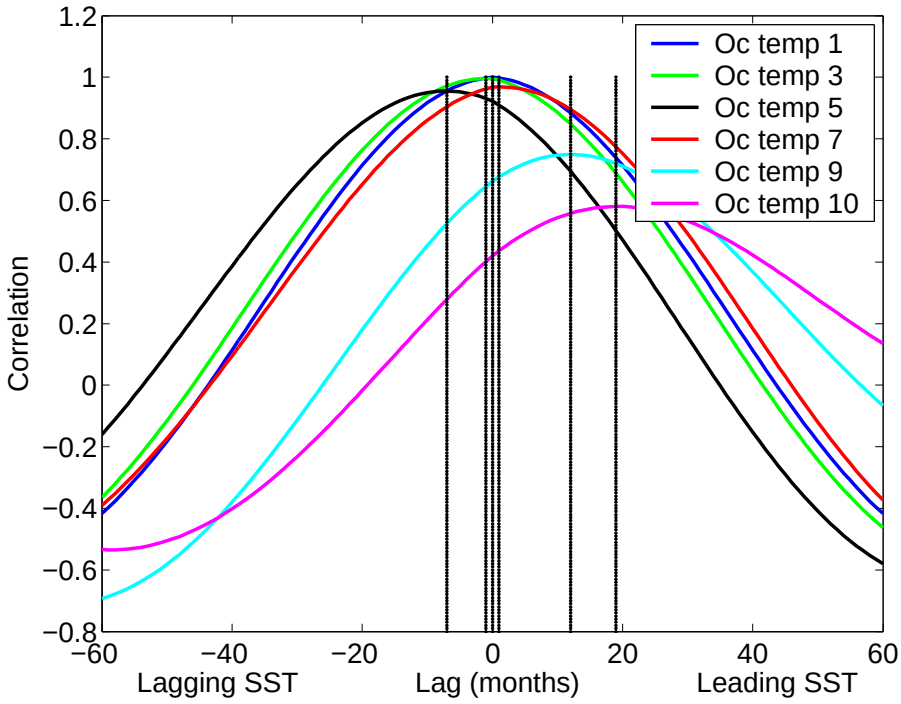

Fig. 3.13: Correlation of subsurface ocean temperature at model levels 3, 5, 7, 9 and 10 with SST for months 360-659 (years 30-55). Autocorrelation of level 1 (SST) is included for reference.

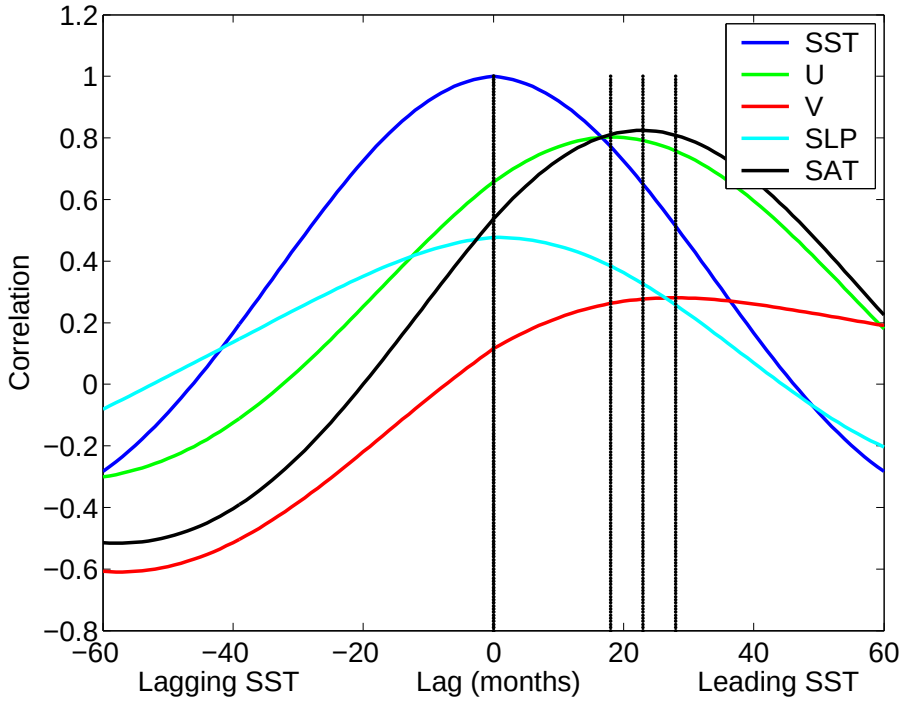

Fig. 3.14: Correlation of atmospheric variables (zonal (u) and meridional (v) wind, sea level pressure (SLP) and surface air temperature (SAT)) with SST for the complete timeseries. Autocorrelation of level 1 ocean temperature (SST) is included for reference.

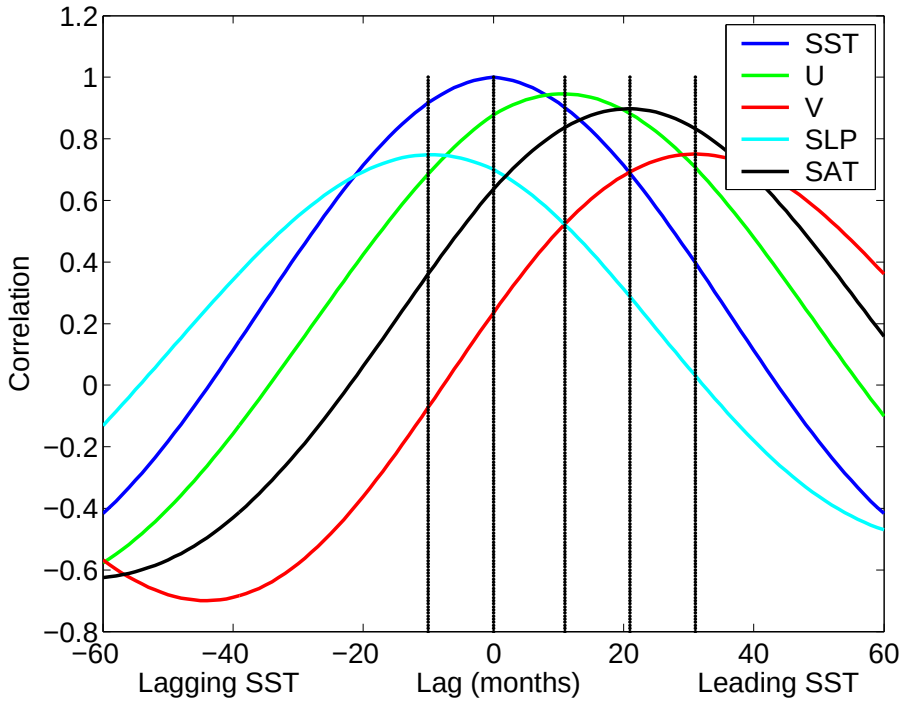

Fig. 3.15: Correlation of atmospheric variables (zonal (u) and meridional (v) wind, sea level pressure (SLP) and surface air temperature (SAT)) with SST for months 360-659. Autocorrelation of level 1 ocean temperature (SST) is included for reference.

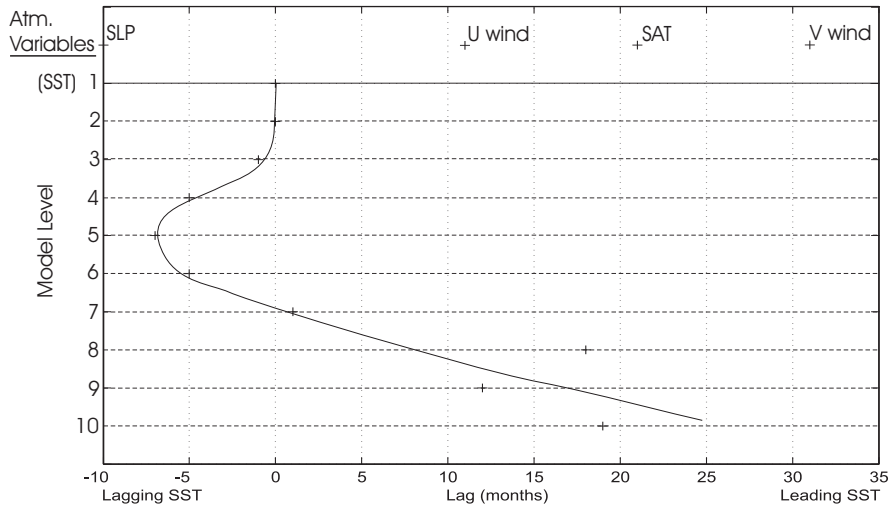

Fig. 3.16: Maximum cross correlation of subsurface ocean temperature with SST for the complete timeseries. A line of best fit indicates lead/lag with depth (model levels). Surface atmospheric variables are marked at the top of the diagram.

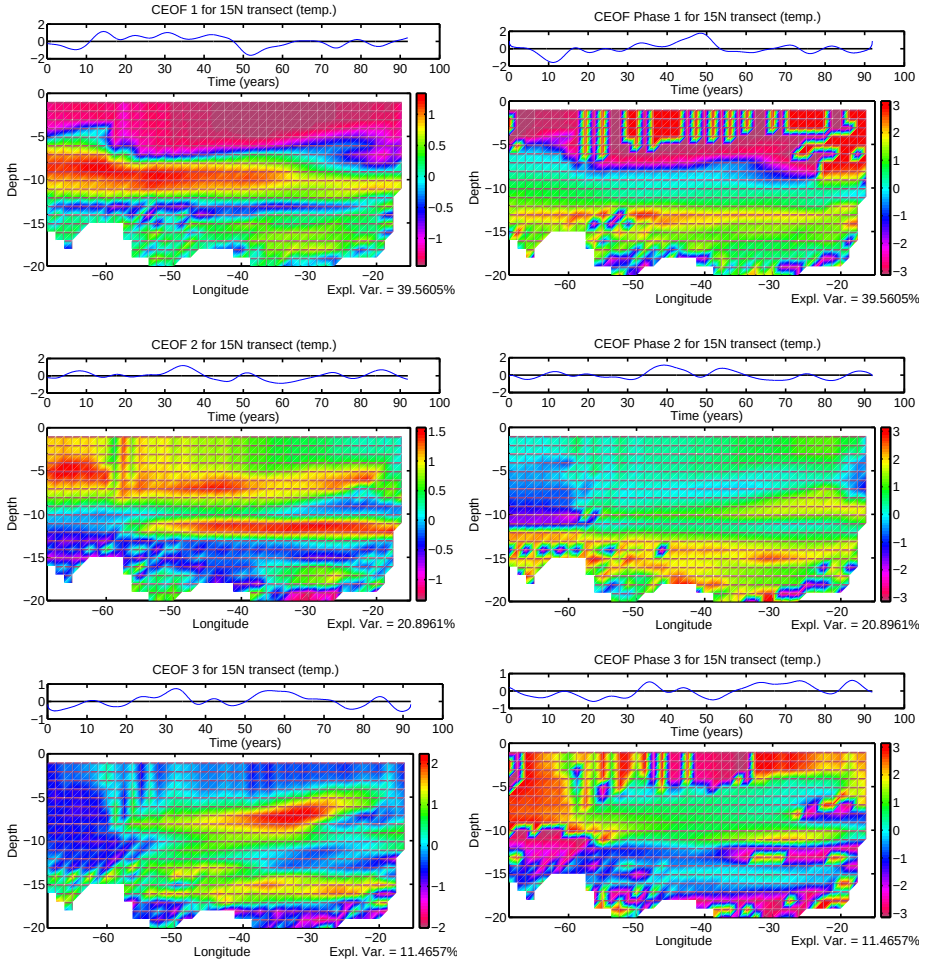

Fig. 3.17: Amplitude (left) and phase (right) components of the first three CEOFs of a vertical temperature profile across the Atlantic along 15°N from the COAPEC 100 year HadCM3 dataset. Data is normalised and an 8yr Butterworth filter applied.

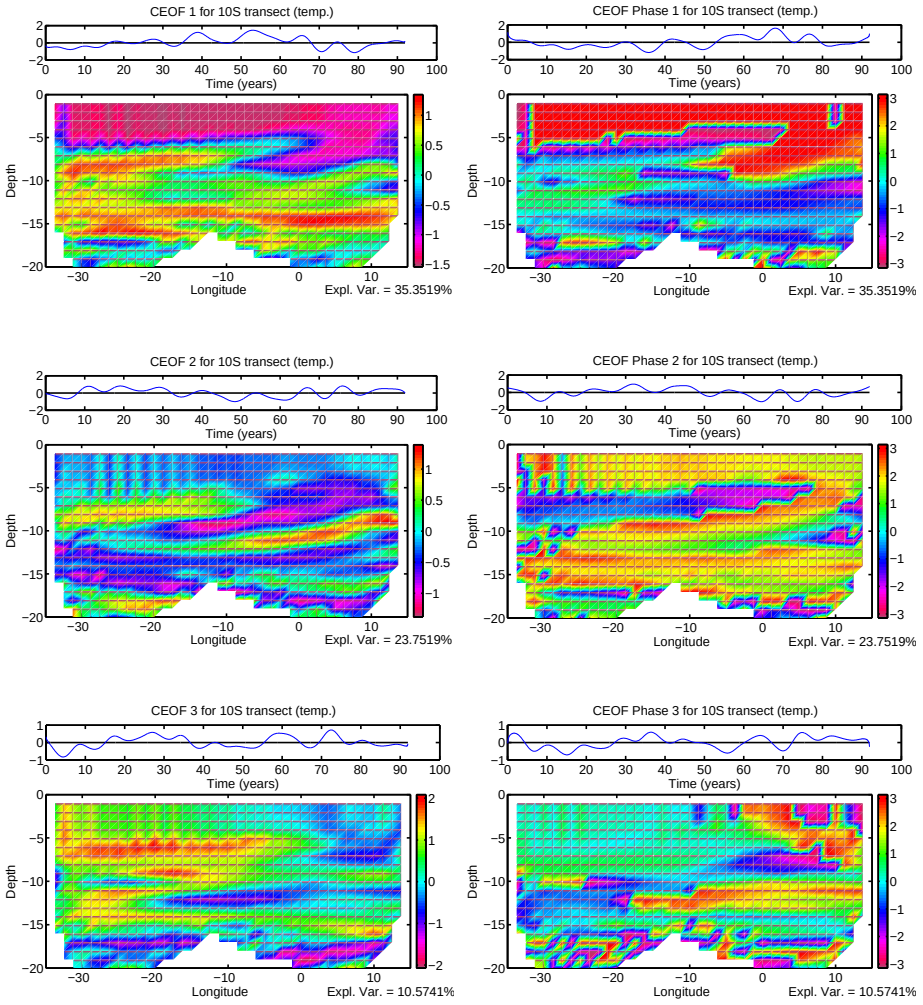

Fig. 3.18: Amplitude (left) and phase (right) components of the first three CEOFs of a vertical temperature profile across the Atlantic along 10°S from the COAPEC 100 year HadCM3 dataset. Data is normalised and an 8yr Butterworth filter applied.

at high latitudes occurs after only 4 – 6 years. Interestingly in this example the dipole causes a southward shift in the ITCZ and leads to the triggering of an El Nino event in the Pacific Ocean the following year. This observation suggests that the atmosphere is able to communicate signals between the tropical Atlantic and Pacific much more quickly than an ocean only response *Goodman* (2001). Goodman also notices what he describes as a curious feature developing at 30°N, 60°W. After 3 years of model time an initial decrease in thickness of the surface layer develops here, but after a further 2.5 years this is reversed and the anomaly becomes positive. It should be noted that *Goodman* (2001) uses a model with 4° x 4° resolution, which is much too coarse to be able to resolve Kelvin or Rossby waves.

It is also possible, as discussed in the literature, that other climate phenomena such as ENSO or the NAO could be forcing the wave response seen here in the subsurface tropical Atlantic. *Dong and Sutton* (2002a) find an atmospheric

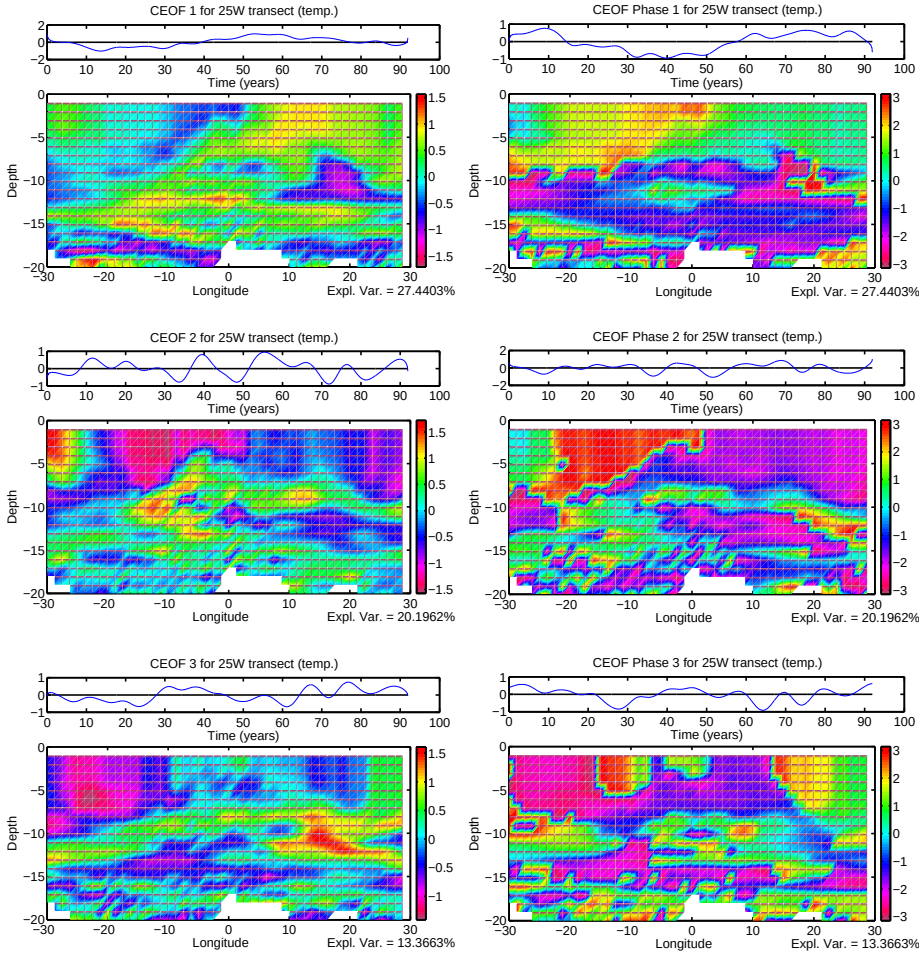

Fig. 3.19: Amplitude (left) and phase (right) components of the first three CEOFs of a vertical temperature profile through the tropical Atlantic along 25°W from the COAPEC 100 year HadCM3 dataset. Data is normalised and an 8yr Butterworth filter applied.

teleconnection between an Atlantic anomaly and the tropical Pacific in HadCM3. *Sutton et al.* (2000) and *Handoh et al.* (2006) show a correlation between ENSO and events in the tropical Atlantic, which suggests an equivalent teleconnection from the Pacific Ocean to the tropical Atlantic may be possible.

3.7 Summary

The results show an asymmetric cross-equatorial temperature dipole in the tropical Atlantic. The surface layers (1 – 4) all show a similar pattern, due to the occurrence of wind mixing, which distributes the anomaly uniformly throughout the wind mixed layer. In the subsurface layers examined, a Rossby wave like signal is visible, with spatial patterns which are much more symmetric about the equator. The development of an asymmetric surface response to a symmetric subsurface forcing mechanism is extremely interesting. It is not clear how the symmetrical response of the Kelvin and Rossby wave mechanism is able to

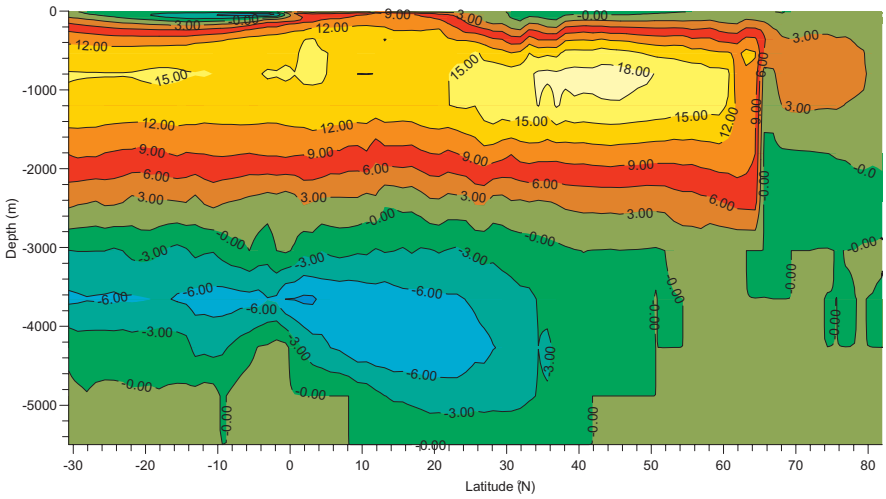

Fig. 3.20: Annual mean meridional overturning circulation (Sv) in the Atlantic Ocean in the COAPEC 100 year HadCM3 control run.

produce the asymmetric response in the surface mixed layer. Possible sources of asymmetry include ocean-atmosphere feedback, changes in the ocean circulation, the meridional component of the wind stress (through Ekman dynamics), or perhaps the distinct shape of the Atlantic basin.

Feedback between the ocean and atmosphere could give rise to equatorial asymmetry. The ITCZ migrates north and south of the equator throughout the year. A strong northward migration of the ITCZ would result in a reduction in the strength of the winds blowing over the northern tropical Atlantic. This would reduce atmospheric transport of heat away from the region, and the location of warmer air above the sea surface would enhance heating of the surface waters. It would also result in stronger winds blowing over the southern tropical Atlantic, drawing cool air across the surface and reducing the SST. It is not obvious how this process could force a decadal cross-equatorial SST dipole, and it does not explain the significance of the Kelvin and Rossby wave mechanism observed here in the subsurface.

Changes in the ocean circulation could impact on the tropical Atlantic in two ways. The meridional overturning circulation (MOC) is composed of a predominantly northward flow of water, mainly constrained within the western boundary currents, in the surface 1000 m and a similar southward flow at depth (Figure 3.20). Sinking of the northward migrating water occurs in the high latitude north Atlantic, where the water cools and sinks. Changes in the MOC would result in heat anomalies in the tropical Atlantic. A stronger MOC would draw warmer equatorial water into the northern tropics and cooler southern extratropical water into the southern tropics. This asymmetry could be forced towards the surface mixed layer by the Kelvin and Rossby wave response seen in the data.

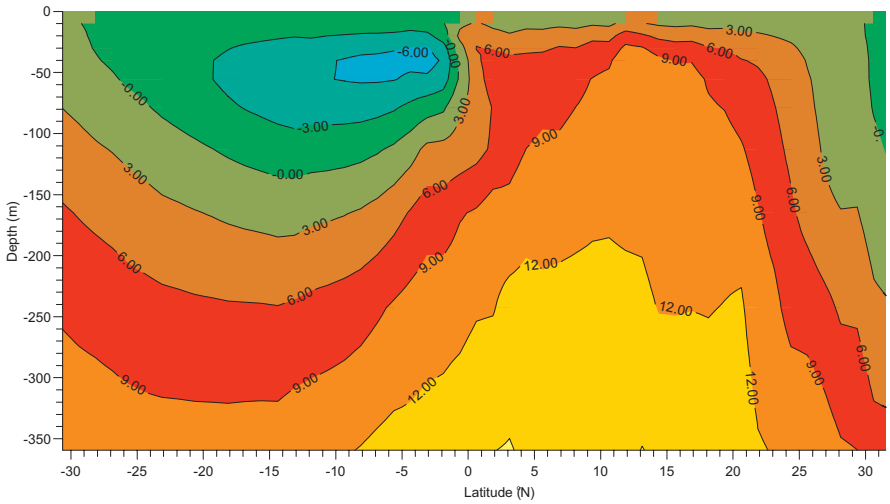

Fig. 3.21: Annual mean meridional overturning circulation (Sv) for the upper 360 m in the tropical Atlantic in the COAPEC 100 year HadCM3 control run.

Also visible in the tropical Atlantic are two shallow MOC cells, either side of the equator (Figure 3.21). Water upwells at the equator and is drawn poleward in both hemispheres by these cells. Sinking occurs at around 20°, and the water returns towards the equator at a depth of around 250 m. These cells broadly encompass the location of the TAD, and asymmetry occurring between them could easily result in formation of the TAD.

The driving mechanism for the Kelvin and Rossby waves cannot be determined due to the complexity of the HadCM3 model. Isolating the cross-equatorial dipole from the higher frequency mechanisms is possible with the use of filtering, but it is not obvious that the forcing mechanism will operate at the same frequency. There is potential for other baroclinic modes or perhaps even the barotropic mode of wave propagation to excite the low-frequency wave response seen in these results. The monthly data output available would not resolve faster wave mechanisms such as these adequately.

Due to the complexity of HadCM3, locating the driving mechanism of the TAD within the COAPEC 100 year dataset has proved unsuccessful. The TAD is one of several competing mechanisms that exist in the tropical Atlantic, and although filtering of the data has removed the higher frequency signals, there are clearly other processes still remaining besides the TAD. With a 100 year dataset, it is difficult to isolate a decadal signal like the TAD more accurately. One possible course of action would be to examine a longer dataset using the same techniques, but this is unlikely to provide any more insight into the driving mechanism behind the cross-equatorial SST dipole. An alternative approach is to attempt to reproduce the cross-equatorial dipole in an idealised model, eliminating all of the complicating factors which obscure the driving mechanism in HadCM3. It is clear from these results that internal wave propagation in the equatorial and

tropical regions plays a fundamental role in the production of a cross-equator dipole. Why a subsurface wave response that is symmetric about the equator should produce an asymmetric surface response is unclear. Feedback between the ocean and atmosphere may be important, but as a first step it is necessary to better understand the role of the ocean. An independent study of the Kelvin and Rossby wave mechanism using a much simpler model domain will enable careful analysis of the processes involved and hopefully highlight key factors which give rise to cross-equatorial asymmetry.

Chapter 4

Wave propagation and cross-equatorial asymmetry in an idealised basin model

4.1 Introduction

Analysis of the COAPEC 100 year segment of the HadCM3 model integration showed that a cross-equatorial asymmetric dipole with a decadal period exists in SST. In the subsurface there is a slow ocean wave mechanism active in the tropics, which is shown to lead the surface dipole. The complexity of HadCM3, and the monthly mean temporal resolution of the dataset, makes it difficult to trace the source of these subsurface waves.

In an attempt to simplify the problem and examine the ocean wave mechanism in more detail, an idealised ocean basin is configured. A series of experiments examine the Kelvin and Rossby wave response to a high latitude anomaly, and look at how the mechanism is capable of rapidly transmitting a signal from high latitudes to the equator. Initially the model is configured as a 'static basin', where all external forcings (latitudinal and longitudinal wind stress, temperature and salinity) are set to zero. The model response to the perturbation in this configuration is purely the response to the anomaly.

Following the experiments using the 'static basin', the model is integrated to equilibrium with all surface forcings applied. A reasonable meridional overturning is created, which bears a strong resemblance to the one seen in HadCM3. A decadal oscillating salinity anomaly is applied to the high latitude northern hemisphere, in an experiment similar to the one described by *Yang* (1999), to further explore the possibility of high latitude deep water formation as a potential driving mechanism for the TAD.

Level	Depth (m)	Thickness (m)
1	15.0	30.0
2	61.15	46.15
3	130.08	68.93
4	230.01	99.93
5	370.64	140.63
6	562.75	192.11
7	817.51	254.76
8	1145.46	327.95
9	1555.27	409.81
10	2052.38	497.11
11	2637.74	585.36
12	3306.83	669.09
13	4049.24	742.41
14	4848.89	799.65
15	5266.94	836.1

Table 4.1: Vertical levels in MOMA.

4.2 The MOMA model

The MOMA model (Modular Ocean Model Array) (*Webb*, 1996) is a primitive equation ocean model. It is a parallelised version of the GFDL MOM code (*Pacanowski and Griffies*, 2000), descended from the original work by *Bryan* (1969), *Semtner* (1974), and *Cox* (1984).

MOMA is a Z-coordinate primitive equation ocean model, which operates on an Arakawa 'B' grid. Horizontal resolution is easily configurable, providing the relevant stability criteria are adhered to. As discussed in Chapter 2, the horizontal resolution used for this study will be 1°. The model version used here has 15 vertical levels (Table 4.1).

MOMA employs a spherical grid with no pole patch, which means that the model is limited to 88° N/S. For the purposes of this study this limitation is unimportant. The model includes a free surface similar to that described in *Killworth et al.* (1991), as well as the *Gent and McWilliams* (1990) eddy parameterisation scheme, but without the bolus velocity terms.

Ocean dynamics are represented by the evolution of the salinity, potential temperature, and horizontal velocities, which are calculated through the equations described in Chapter 2. MOMA employs a leapfrog time stepping scheme, with a periodic Euler backward time step every 24 time steps. The use of the Euler backward time step prevents time splitting. A 'full cell' approach for bottom topography is used (Figure 4.1). This approach leads to spurious mixing of water masses in the boxes adjacent to the bottom, but is very easy and efficient to apply in the case of a Z-coordinate ocean model.

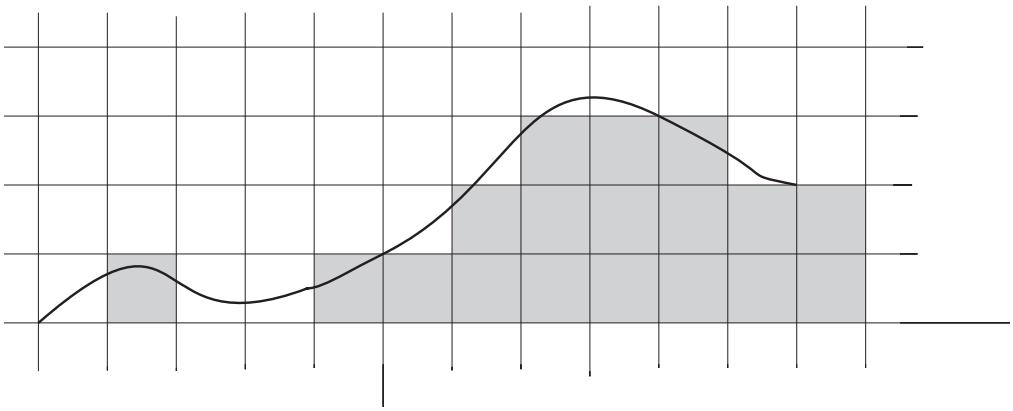

Fig. 4.1: Schematic showing 'full cell' approach to bottom topography. Smooth bathymetry (bold black line) is represented by solid cells (greyed) in the MOMA model.

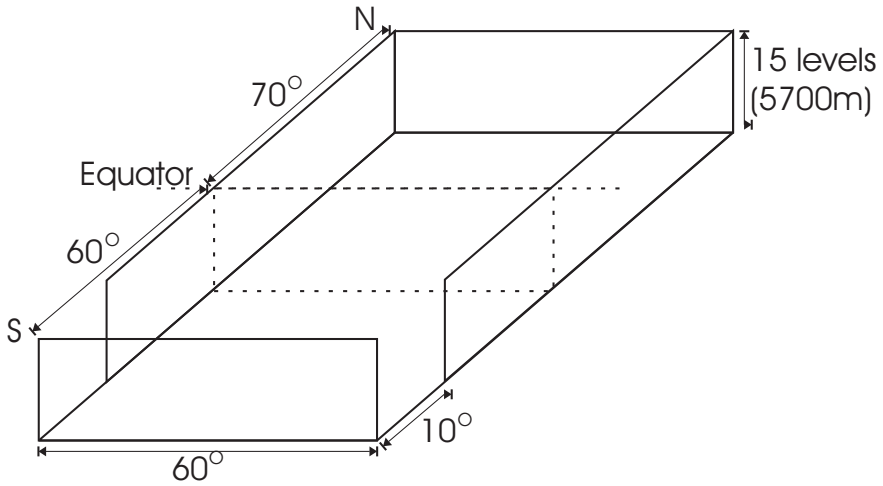

Fig. 4.2: Schematic showing the dimension of the idealised MOMA basin.

There is no explicit mixed layer scheme in MOMA, and a polar island is necessary because there is no pole patch. MOMA also has no ice model, but for the experiments carried out here using an idealised basin design this poses no problem.

4.2.1 Idealised basin description

The basin (Figure 4.2) extends from 70°N to 60°S. It is 60° wide at all latitudes. Due to the variation of the length of degrees with latitude, the basin is a sector from the surface of a sphere. A 10° wide cyclic ACC channel is open in the southern hemisphere from 60°S to 50°S. The idealised basin is of comparable dimensions to the Atlantic basin. The inclusion of high latitudes in both hemispheres allows for possible perturbation experiments in both the northern and southern hemispheres, whilst also negating the need for a sponge layer to damp strong propagating signals. The basin has no topography, and all coastlines are vertical. Depth is uniform at 5500 m throughout the basin.

4.3 'Static Basin' configuration

Some initial experiments were carried out using a 'static basin', in which no external forcings were applied. This enabled close examination of the Kelvin and Rossby wave propagation in MOMA, without interference from any other mechanisms, such as meridional overturning or background velocities, which will influence the propagation of planetary waves. The 'static basin' configuration also allowed close inspection of the model response to different perturbations.

Wind stress was set to zero in both the x and y directions, and temperature and salinity restoring forces were removed. A salinity of 34 was prescribed uniformly throughout the basin, and a temperature profile close to globally averaged *Levitus and Boyer* (1998) was prescribed vertically, and temperature was uniform horizontally. During the control run of the static basin no motion occurred in the basin. The temperature profile relaxes through diffusion towards a uniform temperature at all depths over time. The effect of this diffusion is removed in the analysis by taking a perturbation-control anomaly.

4.3.1 Introducing anomalies

The model was perturbed in order to propagate Kelvin waves equatorward along the western boundary. A 4° x 4° anomaly was placed in the upper left (North-West) corner of the basin. A control run is completed by initialising the model from a restart file. To produce the anomaly run the original restart file is altered to include the anomaly. The run is then completed by initialising the model from the modified restart file. This method means that the anomaly introduced is instantaneous. Forcing or restoration fields are not adjusted in any way, and the model is able to respond to the anomaly without further interference.

Three perturbations were tested: a) Quarter Sin wave, b) Half Sin wave, and c) Full Sin wave (Figure 4.3). Each perturbation was sinusoidal in the vertical. Horizontally the perturbations appear as a step in the temperature field. Experimentation with smoothing this step resulted in minimal difference, as the sharp step is smoothed rapidly by the model anyway.

For all data analysis, the control run was subtracted from the perturbation run (P-C) in order to remove the effects of the diffusing temperature profile and provide an anomaly field. The P-C data shows only the model response to the perturbation.

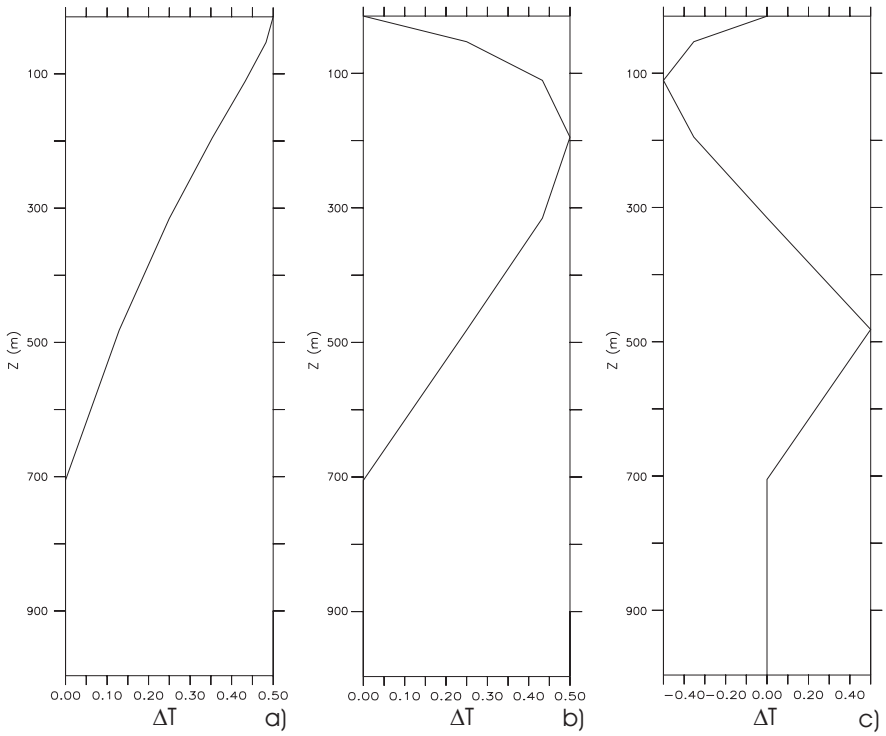

Fig. 4.3: Plot of temperature perturbation vs. depth (°C). Quarter sin (a)), half sin (b)), and full sin (c)) perturbations are shown.

4.3.2 Results

In the source region of the basin, a gyre circulation, formed through vortex stretching of the water column, appears. Vortex stretching occurs where the water column is stretched, in this case by warming or cooling of the water column. Positive (negative) stretching of the water column corresponds to cyclonic (anticyclonic) rotation to occur.

Increasing the temperature in a region at the surface of the model (Figure 4.3 a)) causes a reduction in the density. In response to the hydrostatic pressure change, upwelling occurs at the centre of the anomaly, initiating a radial flow away from the anomaly at the surface, and towards the centre of the anomaly at depth. To conserve potential vorticity, a rotational flow develops. At the surface this rotational flow is anticyclonic, corresponding to vortex squashing (Figure 4.4 a)). Vortex stretching occurs at depth (Figure 4.5 a)). Geostrophy requires an increase in the sea surface height above the centre of the anomaly (Figure 4.6 a)).

The full-sin anomaly results in the least disturbance of the FSH, minimising the barotropic response (Figure 4.6). This is because the positive and negative temperature anomalies introduced into the water column result in (approximately) equal and opposite vortex stretching responses. Another implication of this anomaly is that the forcing applied to the layers between the positive and negative temperature anomalies are subject to a stronger forcing

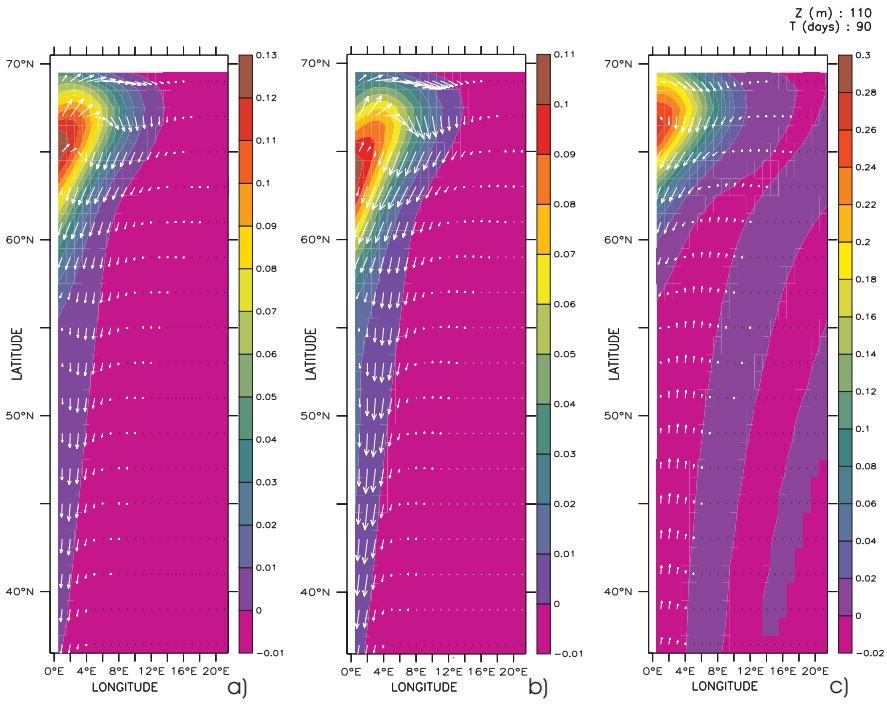

Fig. 4.4: Level 3 temperature anomaly after 90 days with velocity field overlayed for a) 1/4 sin, b) 1/2 sin, and c) full sin anomalies in the north west corner of the idealised MOMA basin. Full sin anomaly is *-1 to ease comparison.

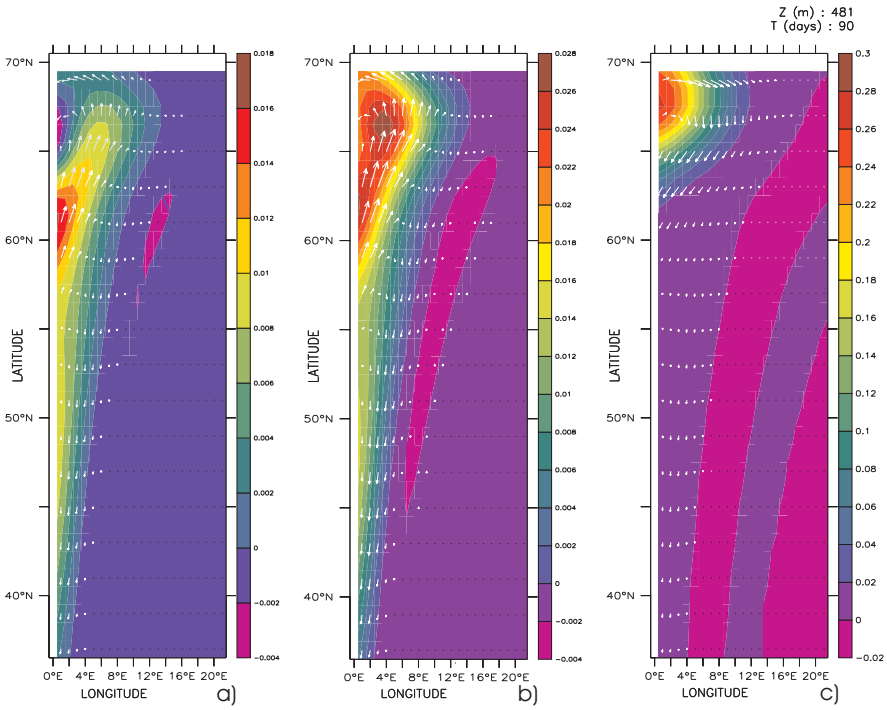

Fig. 4.5: Level 6 temperature anomaly after 90 days with velocity field overlayed for a) 1/4 sin, b) 1/2 sin, and c) full sin anomalies in the north west corner of the idealised MOMA basin.

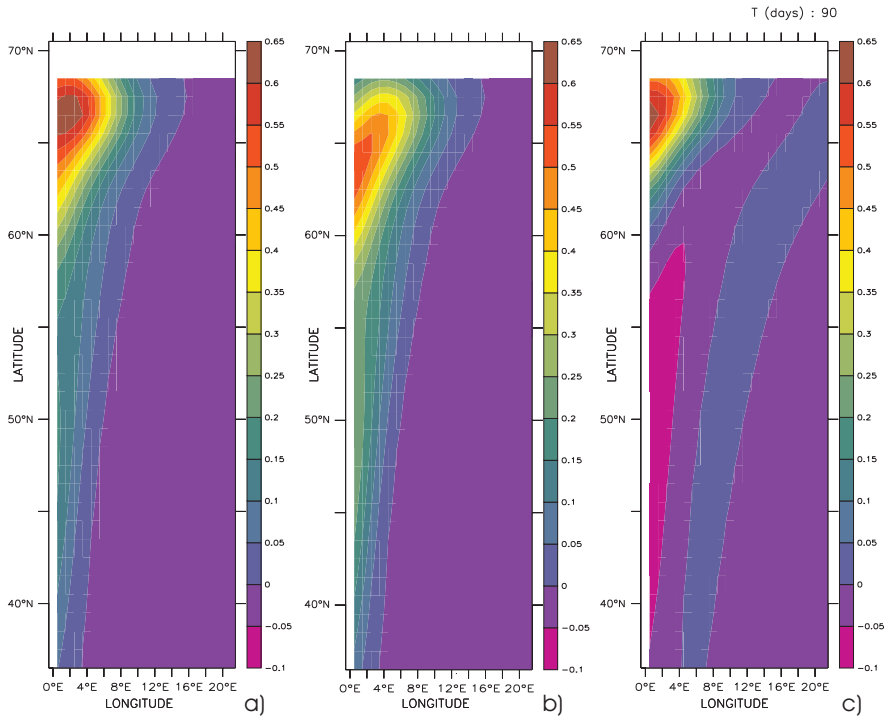

Fig. 4.6: FSH anomaly after 90 days for a) 1/4 sin, b) 1/2 sin, and c) full sin anomalies in the north west corner of the idealised MOMA basin.

than those affected only by a single sign anomaly, due to the positive and negative stretching working in unison. The vertical disturbance of the layers that arises from the vortex stretching is what initiates the Kelvin wave propagation equatorward along the western boundary.

The FSH anomaly in the 1/4 and 1/2 sin anomalies extend 20° further equatorward along the western boundary. Comparatively stronger southward flows are associated with this change in FSH (Figure 4.4). The magnitude of the perturbation was adjusted to try and minimise the effect of the gyre on the rest of the basin. This was necessary since in the static basin none of the usual forcing/restoration fields, that would normally return the model to its original state, apply. The model response to the perturbation was linear (ie η/H was very small).

The full-sin anomaly was chosen for analysis of the Kelvin and Rossby wave propagation because it minimises the influence of the gyre formed by the anomaly (Figure 4.5) as well as minimising disturbance to the free surface height, significantly reducing the barotropic response. It is also able to produce a stronger wave response than the other anomalies due to the opposite signs of the anomaly working in unison to displace the baroclinic layers within the ocean.

Analysis of a one year integration of the static basin shows clear equatorward propagation. Upon reaching the equator the signal forms an equatorial Kelvin wave. It then propagates across the basin towards the eastern boundary.

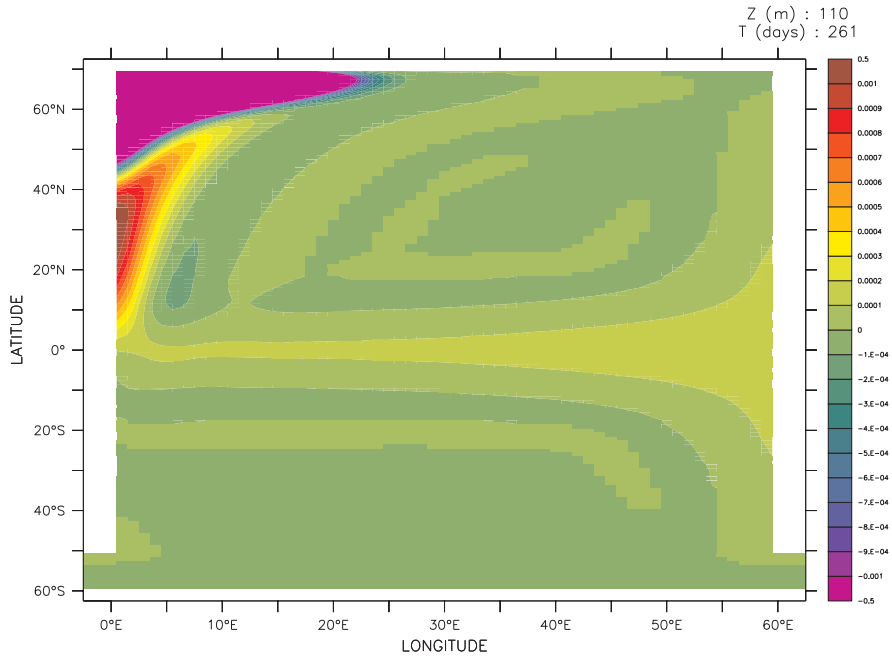

Fig. 4.7: Temperature anomaly seen at level 3 (110 m), 260 days after the introduction of the perturbation in the idealised MOMA basin.

On reaching the eastern boundary the signal diverges, creating two poleward propagating Kelvin waves, one in each hemisphere. As these Kelvin waves propagate poleward, Rossby waves form and propagate westward into the interior of the ocean, creating a symmetric signal about the equator (Figure 4.7).

It is possible to analyse the energy budget in this simple model easily. The idealised domain means that the JEBAR term is zero throughout. The barotropic and baroclinic energy at points every 15° along the path of the Kelvin wave shows the progression of the wave (Figures 4.8, 4.9). The barotropic response peaks after the baroclinic, suggesting that there is transfer of energy from internal to external modes.

There is evidence of a barotropic response visible in the baroclinic kinetic energy (Figure 4.9). Baroclinic kinetic energy on the equator peaks at the eastern boundary before the centre of the basin. This suggests there is conversion of energy from external to internal modes at the eastern boundary.

To allow the formation of any possible asymmetry to develop the integration was extended to 10 years. The only asymmetry present in the basin after 10 years of integration derives from experimental design. Locating the initial perturbation in the northern hemisphere results in obvious asymmetry along the western boundary north of the equator compared to the south. The other source of asymmetry arises from the existence of the open ACC channel in the southern hemisphere. Because the channel is cyclic, the Kelvin wave signal that propagates poleward in the southern hemisphere is able to propagate through the

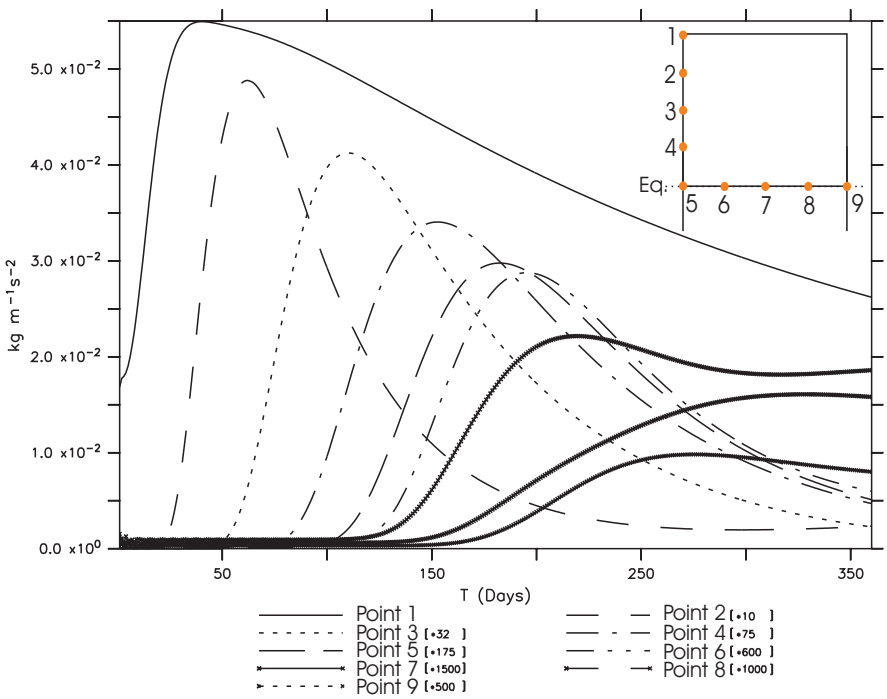

Fig. 4.8: Barotropic kinetic energy ($\mathrm{kg\,m^{-1}\,s^{-2}}$) against time for points selected every 15° along the western boundary and along the equator. Curves have been scaled to allow comparison between points.

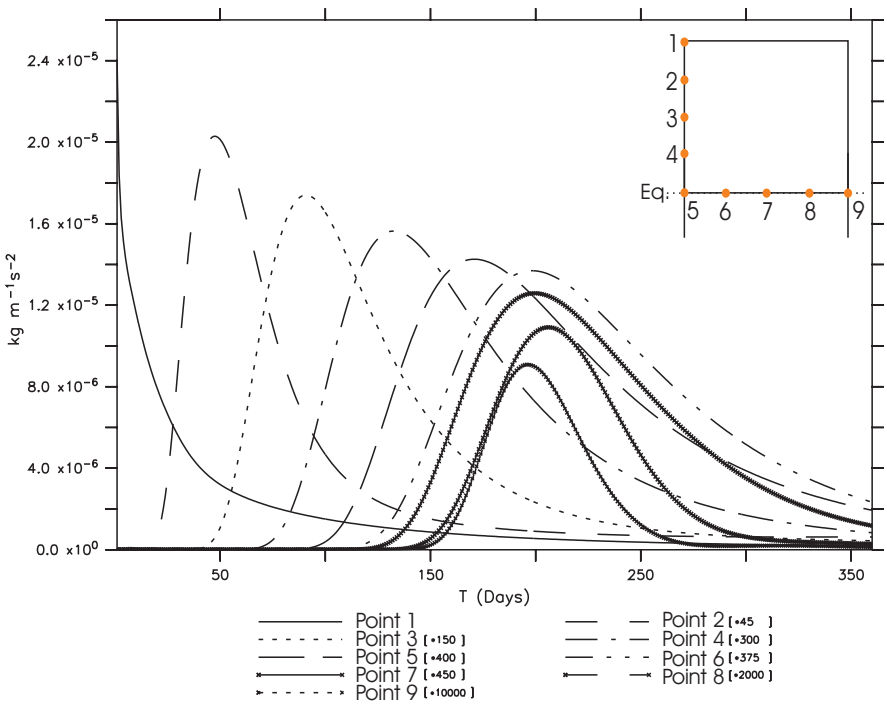

Fig. 4.9: Baroclinic kinetic energy ($\mathrm{kg\,m^{-1}\,s^{-2}}$) against time for points selected every 15° along the western boundary and along the equator. Curves have been scaled to allow comparison between points.

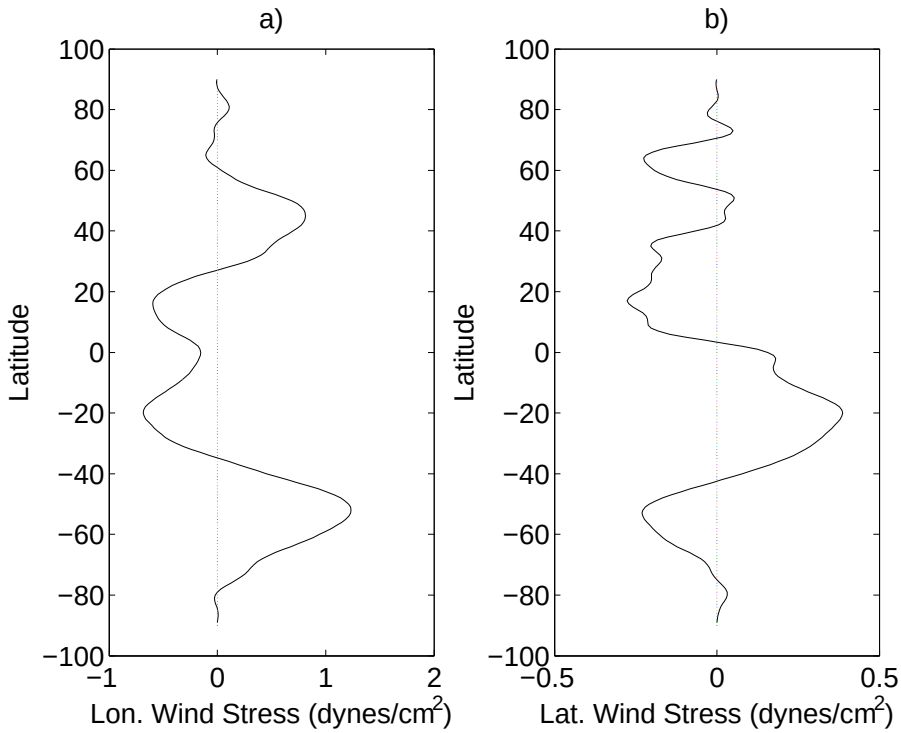

Fig. 4.10: Longitudinal (a)) and latitudinal (b)) wind stress forcing (dynes/cm^2) applied to the surface of the model (*Hellerman and Rosenstein*, 1983).

channel and then begin to propagate equatorward along the western boundary in the southern hemisphere. As a result the Kelvin wave signal in the southern hemisphere has a shorter distance over which to propagate compared to its northern counterpart. This shows that although the Kelvin and Rossby wave mechanism is capable of rapidly transmitting a high latitude signal to the equator, something else is required to create cross-equatorial asymmetry in the tropical Atlantic Ocean.

4.4 The basin with overturning

The idealised basin described above was also run with all forcing fields applied. Zonally averaged windstress from *Hellerman and Rosenstein* (1983) was applied to the surface of the ocean (Figure 4.10), and surface temperature and salinity were restored to zonally averaged Atlantic values of Levitus 1998 (*Levitus and Boyer*, 1998; *Levitus et al.*, 1998) with a period of 40 days (Figure 4.11).

The meridional overturning arising from these surface restoration fields was weak (max. 5 Sverdrups) and there was no cross equatorial flow into the northern hemisphere at the surface. In order to produce a more realistic overturning in the model, it was necessary to make linear adjustments to the surface salinity restoration field. These adjustments were made in small increments, and the model was integrated again after each adjustment until the overturning

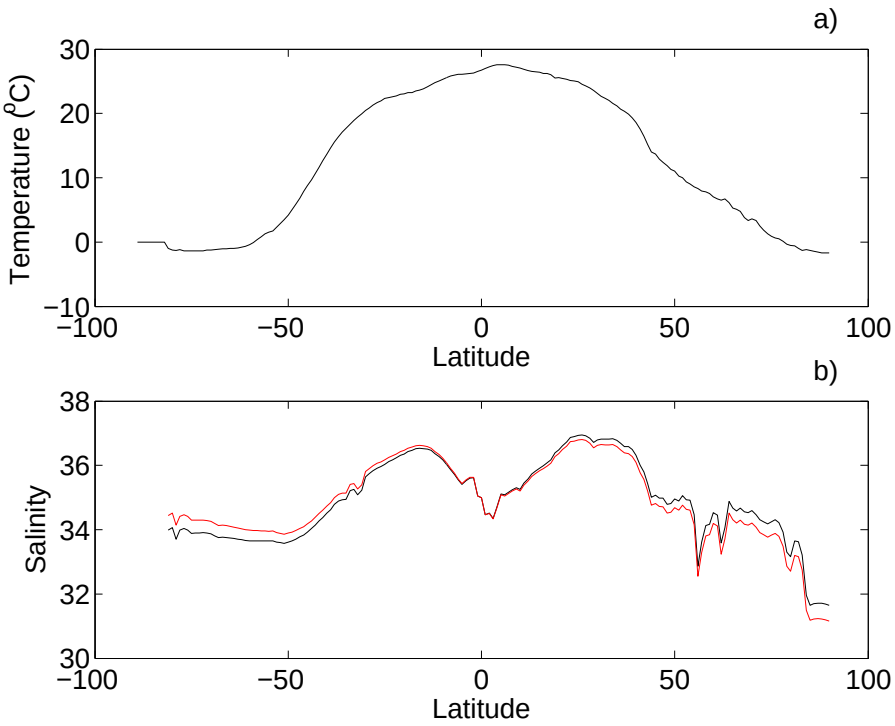

Fig. 4.11: Restoring values for a)SST (*Levitus and Boyer*, 1998) and b)SSS (*Levitus et al.* (1998) with a linear adjustment about the equator to increase salinity in the NH by 0.5 and freshen the SH by 0.5), shown in black. The original surface salinity data is shown in red.

stabilised. A total adjustment of $m = 1/180n - 0.5$ was applied to the surface salinity to achieve a satisfactory meridional overturning circulation. This resulted in a freshening of 0.5 at 90°S and a corresponding increase of salinity at 90°N. The total integration time was around 2000 years, with 100 years completed since the last adjustment to the surface forcing.

The meridional overturning circulation produced by the model is reasonable (Figure 4.12). The maximum overturning is 16 Sverdrups at 60°N, which is 2–3 Sverdrups weaker than the overturning in HadCM3 (Figure 3.20). In the northern hemisphere the idealised model shows a similar overturning circulation to HadCM3, with high latitude sinking occurring at 70°N in both models. The depth of the main meridional overturning cell is around 2000 m in both models. South of the equator the overturning in the idealised basin weakens considerably, whereas in HadCM3 the overturning remains strong and reasonably consistent to 30°S. The weakening of the circulation south of the equator in the idealised basin is largely due to the absence of a Pacific basin. Asymmetry of the temperature and salt forcing between the high latitude Atlantic and Pacific basins gives rise to strong overturning in the Atlantic basin, which crosses the equator into the northern hemisphere, sinks and returns at depth towards the Southern Ocean (*Mead*, 1989). The shallow meridional overturning cells in the tropical Atlantic are strong, with maximum values of 12 Sv compared to 6 Sv in HadCM3 (Figure 4.13).

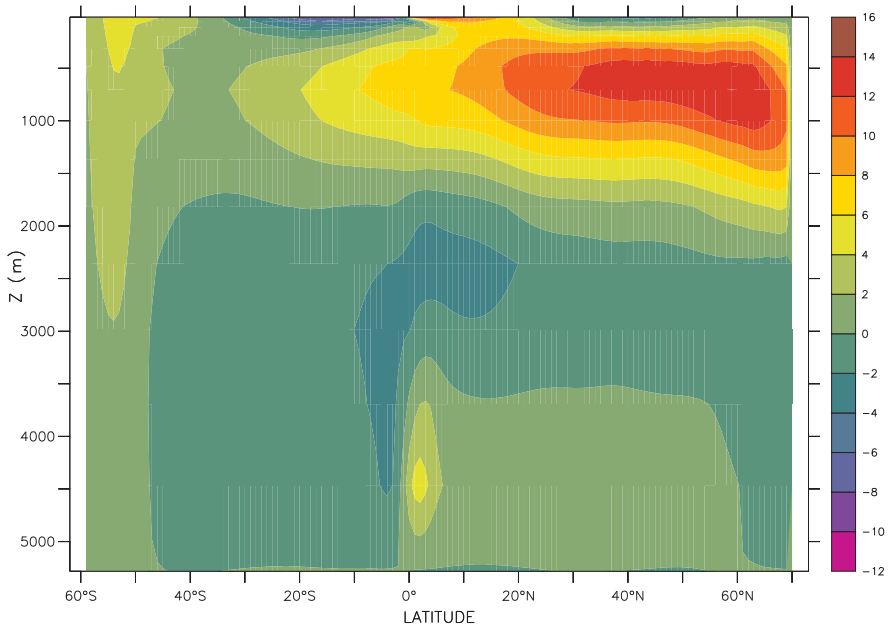

Fig. 4.12: Annual mean meridional overturning strength (Sv) for the Atlantic Ocean in the idealised MOMA basin after the spinup.

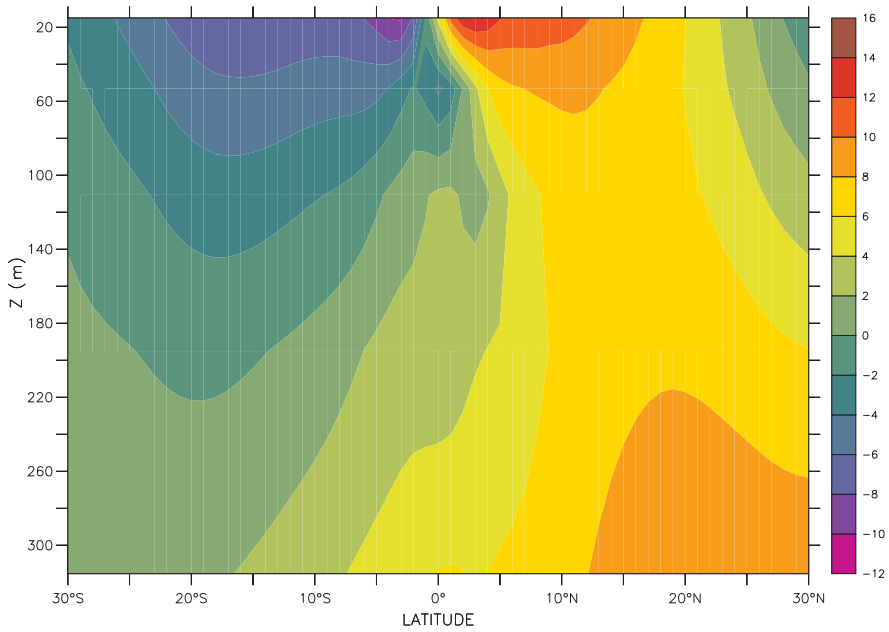

Fig. 4.13: Annual mean meridional overturning strength (Sv) in the upper 300 m of the tropical Atlantic in the idealised MOMA basin.

This may be due to a combination of strong surface restoration applied to the surface of the ocean and the absence of a Pacific basin, which would influence the MOC in the Atlantic.

4.5 Fluctuating overturning on a decadal timescale

Yang (1999) demonstrated that it was possible to form a cross-equatorial dipole in an idealised model basin by forcing the MOC to fluctuate. In this section, results from a model experiment similar to the one described by *Yang* (1999) are presented. Analysis of data from HadCM3 in chapter 3 showed that wave propagation in the tropics is likely to be important in the formation of the TAD. Idealised studies earlier in this chapter show that wave propagation in the tropics can arise from the introduction of anomalies in the high latitude northern hemisphere. These studies also reveal that formation of an asymmetric cross-equatorial SST dipole cannot arise from wave propagation alone. It is possible that the cross-equatorial dipole identified by *Yang* (1999) arose through interaction of the wave mechanism with fluctuations in the MOC.

4.5.1 Method

A sinusoidal salt forcing with a peak amplitude of 0.3 and a decadal period is introduced to the surface salinity restoring boundary conditions north of 67°N. The sinusoidal salt forcing produced an overturning strength which fluctuates by +/- 1.5 Sv with decadal period (Figure 4.16 a)). The model was integrated for 50 years, giving 5 complete cycles of the anomaly. In the idealised basin configuration this proves sufficient to identify clearly the response of all model variables.

4.5.2 Results

All model variables fluctuate with a decadal period in response to the perturbation. The focus of the analysis is primarily on the tropical region.

Tropical SSTs fluctuate with the overturning (Figure 4.14). North and south of the equator the SST fluctuations are almost synchronised in time. Evidence of cross-equatorial asymmetry can be seen by subtracting the signal in the southern tropical Atlantic from the signal in the northern tropical Atlantic (Figure 4.15). This asymmetry does not derive from different mechanisms driving the south and north tropical SST signals. It shows that one hemisphere, in this case the southern hemisphere, is responding more strongly to the decadal forcing than the northern hemisphere. This is seen more clearly when comparing the anomalous maximum meridional overturning in the shallow tropical cells (Figure 4.16).

The strength of the temperature signal is stronger at depth, by up to two orders of magnitude, compared to the signal at the surface. The strong surface restoration dampens the signal in the surface layers.

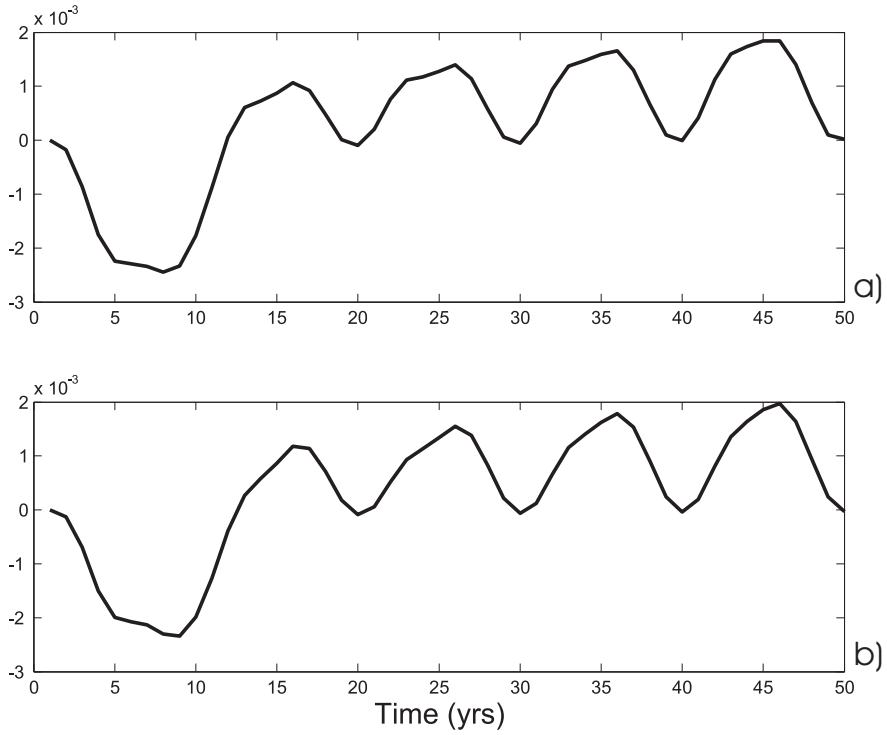

Fig. 4.14: Time series of temperature anomalies (°C) for a) north tropical area averaged SST (0–10°N,0–20°E), b) south tropical area averaged SST (0–10°S,0–20°E).

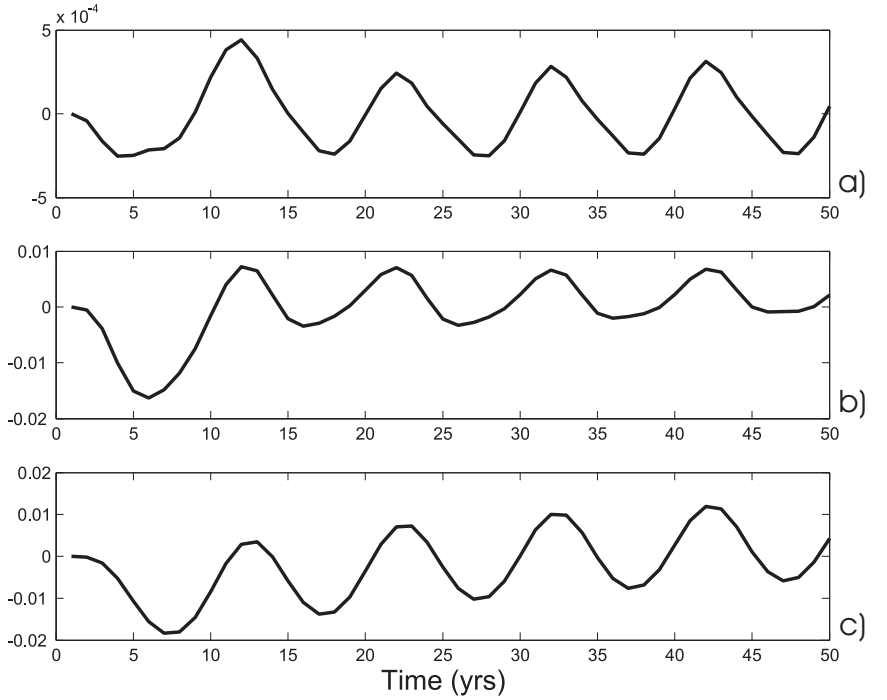

Fig. 4.15: Time series of NH temperature anomalies - SH temperature anomalies (°C) for a) SST, b) level 5, c) level 7.

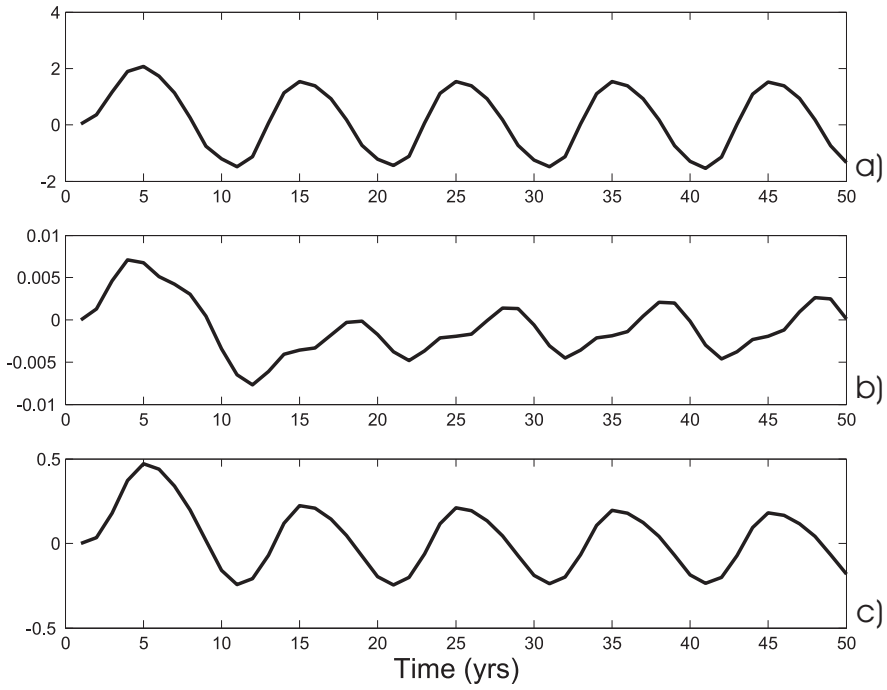

Fig. 4.16: Anomalous maximum meridional overturning strength (P-C) for a) MOC, b) NH shallow tropical MOC, c) SH shallow tropical MOC. Units are Sv.

The shallow meridional overturning cells either side of the equator display evidence of an asymmetric response to the overturning forcing applied. The southern hemisphere shallow MOC cell fluctuates synchronously with the main MOC circulation. There is a lag of 6–12 months between the high latitude forcing and the tropical response. The northern hemisphere shallow MOC cell also fluctuates, but does not show a clean sinusoidal oscillation. The peak values of the overturning lag the peaks of the main meridional overturning signal by 3 years. This is consistent with the timescale discussed by *Yang* (1999), where the delay between the high latitude forcing and the tropical response is equivalent to 1/4 of the forcing period plus the time take for the coastal Kelvin wave to propagate (around 6 months). The same lag does not occur in the southern tropical shallow MOC cell in this experiment.

The southern hemisphere shallow MOC cell oscillates by +/- 0.2 Sv, which is more than 10% of the variability seen in the main MOC cell. In the northern hemisphere shallow MOC cell the oscillation is much weaker, around +/- 5 x 10^{-3} Sv. This suggests that the mechanism which transfers the signal to the northern cell is weaker than that which drives the southern cell. This is interesting, since the deep overturning is much stronger in the NH than it is in the SH, and also the source of the oscillation is located close to the northern boundary. The closer proximity of the northern hemisphere shallow MOC cell to the stronger NH MOC overturning and the source of the forcing would usually result in a stronger response compared to the SH shallow MOC cell.

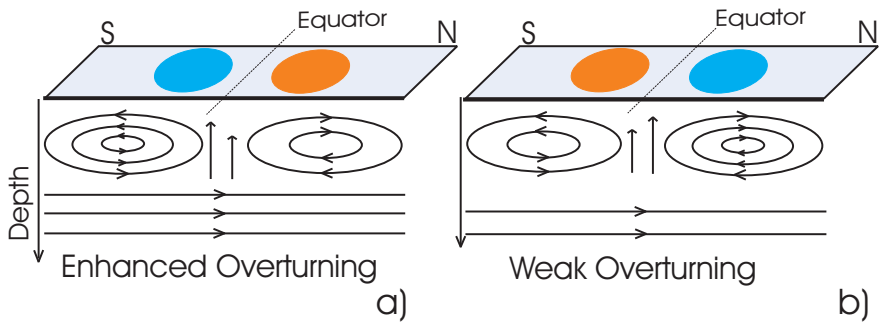

Fig. 4.17: Schematic showing a mechanism to produce cross-equatorial asymmetry in the tropical Atlantic. The cases for a) stronger overturning, and b) weaker overturning, are shown.

Stronger southern hemisphere shallow MOC cell overturning is closely correlated to stronger deep overturning (Figure 4.16). This could be explained by a transfer of momentum from the deep MOC cell to the SH shallow MOC cell. Where the cells meet, both are flowing north towards the equator. An increase in flow in the main MOC will act to increase the overturning in the SH shallow MOC cell, whilst at the same time retarding the overturning in the NH shallow MOC cell. In the case of an enhanced main MOC cell (Figure 4.17 a)), upwelling at the equator is preferentially drawn south into the southern tropical shallow MOC cell, and gives rise to a cooler area south of the equator. In the northern tropical Atlantic, a reduction of northward flow at the surface bringing cool equatorial upwelled water north leads to a warming, which may be enhanced through positive feedback interaction with the atmosphere in the real world. A weakening of the deep meridional overturning circulation leads to the reverse, with stronger overturning in the northern tropical Atlantic drawing a larger volume of cool equatorial upwelled water north, cooling the are north of the equator, and a weaker southern shallow MOC cell drawing less equatorial upwelled water south.

In addition to this, equatorward propagation at the bottom of the shallow tropical MOC cells would draw cool water towards the equator. This water may be lifted up into the cells through Kelvin and Rossby wave activity and mixed by the wind. Weaker overturning of the shallow cells would result in less cool water being drawn equatorward, thus reducing the effect of this mechanism. Wind mixing would lead to the signal rapidly being uniformly mixed throughout the surface mixed layer, as is seen in the HadCM3 results.

4.5.3 Discussion

For this experiment, changes in the strength of the meridional overturning are most important, whereas in HadCM3 the role of the Kelvin and Rossby waves

appears to be far more significant. This may be due to the strength of the fluctuating overturning signal dominating the model. The shallow tropical MOC cells are much stronger in the idealised basin model than those seen in HadCM3. A possible explanation for why an asymmetric cross-equatorial SST dipole does not readily appear is that the surface restoration is too strong to allow such asymmetry to develop. Temperature and salinity are restored to Levitus 1998 values over a period of 40 days, whereas the overturning fluctuation is set at 10 years. This suggests that feedback between the ocean and atmosphere is an important component of the TAD's formation and structure.

The tropical SST asymmetry shown here in this tropical idealised basin experiment arises from the southern hemisphere responding more readily to the fluctuating overturning signal created in the MOC.

The model responses in the northern and southern hemispheres are in phase with each other, however, the southern hemisphere shallow MOC cell is of larger amplitude, displaying stronger maxima and minima than its northern hemisphere counterpart. Consequently, asymmetry between the two hemispheres can arise from subtracting an area averaged value from the northern hemisphere from the equivalent area in the southern hemisphere. EOF analysis of the data identifies this signal as a cross-equatorial dipole structure, which is misleading because the actual signal does not vary asymmetrically about the equator. This highlights another example of why EOF analysis, discussed in chapter 3, must be interpreted with care.

4.6 Summary

In the first part of this chapter the wave response of an idealised model to high latitude forcing is examined. Kelvin waves are seen to propagate equatorward along the western boundary in the northern hemisphere. On reaching the equator they propagate along it to the eastern boundary. No cross-equatorial asymmetry occurred in the tropical region of the model, even after 10 years of integration. This indicates that the wave mechanism alone is unable to drive a cross-equatorial dipole. A previous publication by *Yang* (1999) suggests that a cross-equatorial asymmetric dipole can be established in an idealised model by forcing a pulsing MOC. An experiment similar in design to *Yang* (1999) is set up. This study confirms that pulsing of the meridional overturning circulation driven from high latitudes is capable of influencing the structure of the equatorial and tropical ocean. The decadal variability is transferred to the shallow meridional overturning cells either side of the equator. The SST can be seen to vary symmetrically about the equator, synchronously increasing

and decreasing. Further examination shows that it is possible to determine an asymmetric oscillation about the equator, which arises due to the stronger response of the southern tropical MOC cell to the sinusoidal forcing of the MOC.

The results suggest that the boundary conditions that have necessarily been imposed on the model are restricting the freedom of the model to respond to the salinity forcing applied at high latitudes. The surface relaxation timescale of 40 days is two orders of magnitude shorter than the period at which the MOC anomaly is forced. As a result, signals in the surface layers are significantly reduced. A solution to this problem would be a further study using an idealised coupled model, which would permit the surface of the ocean more freedom to respond to the subsurface signal from the MOC circulation. It would also allow ocean-atmosphere interaction, which is potentially important for the formation and strength of the TAD signal. At this time, with no experience of configuring coupled climate models, this study is beyond the scope of this project.

One question that must be asked following these experiments is whether a barotropic wave response to a high latitude anomaly is able to influence the tropics. The experiments in this chapter focus strongly on the propagation of baroclinic Kelvin waves from the high latitudes to the equator. The baroclinic Kelvin waves are able to transmit a signal from high latitudes to the equator over a timescale of 6 – 12 months. Barotropic waves have potential to transmit a signal far quicker, on a timescale of days to weeks.

The experiments presented in this chapter have considered only the ocean response. The role of the atmosphere in transmitting a signal from high latitudes to the equator also has yet to be examined. It is reasonable to assume that the atmosphere could transmit a signal from high latitudes to the equator much faster than the ocean.

Chapter 5

Rapid climate responses in a fully coupled GCM

5.1 Introduction

The previous chapters have examined the baroclinic wave response as a means of propagating a signal from high latitudes to the tropics. Barotropic wave propagation is far faster (hundreds of $\mathrm{m\,s^{-1}}$) than baroclinic wave propagation (a few $\mathrm{m\,s^{-1}}$). It is also obvious that the atmosphere has good potential for transmitting signals around the globe very rapidly. In this chapter, the relative roles of the ocean and atmosphere in transmitting a signal from high latitudes to the equator and tropics is examined with the aid of a fully coupled climate model.

Considerably more research has been published on teleconnections between the equatorial Pacific and high latitudes than between the Atlantic and high latitudes. A number of previous studies suggest atmospheric teleconnections between the strength of the El Niño-Southern Oscillation (ENSO) index and Antarctic sea ice extent (*Karoly*, 1989; *Simmonds and Jacka*, 1995; *Harangozo*, 2000; *Yuan and Martinson*, 2000). Evidence of an ocean teleconnection between ENSO and the Southern Ocean is much more scarce. *Peterson and White* (1998) and *Cai and Baines* (2001) identify a slow ocean teleconnection linking the Antarctic Circumpolar Wave to ENSO. More recently some research has demonstrated a plausible barotropic wave mechanism connecting the tropical Pacific and the Southern Ocean. *Ivchenko et al.* (2004) demonstrate a mechanism by which it is possible for the ocean to rapidly transmit a response, from a high latitude anomaly to the equator, using an ocean only model with an idealised Pacific basin and Southern Ocean domain. *Richardson et al.* (2005) found evidence to suggest the existence of the mechanism outlined by *Ivchenko et al.* (2004) in HadCM3.

Determining the relative importance of the ocean and atmosphere in transmitting this signal to the tropics is clearly important.

In this chapter, the initial rapid response of the coupled ocean-atmosphere system to a salinity anomaly in the Weddell Sea is examined to see if it is possible for the *Ivchenko et al.* (2004) mechanism to operate in a coupled climate model with realistic topography.

A coupled climate model (FORTE) allows wave propagation to be excited within the ocean. Use of a mixed-layer version of the model removes the ocean's dynamic response, preventing wave propagation. Comparison of the full-ocean model to the mixed-layer version separates the atmospheric and oceanic responses to the anomaly.

Analysis of the kinetic and potential energy of the ocean component of the model reveals a complex barotropic wave response which transmits energy from the source region to the western equatorial Pacific. A second response to the anomaly is seen in the NH high latitudes, transmitted through an atmospheric teleconnection.

Some of the material presented in this chapter has already been published as an article in GRL (*Blaker et al.*, 2006), and a reprint of this paper is included as Appendix B.

5.2 Model Description

FORTE is a fully coupled climate model developed at NOC,S (*Sinha and Smith*, 2002; *Smith et al.*, 2004).

5.2.1 The Ocean

The ocean component of FORTE is MOMA. The code is identical to that used for the idealised basin experiments, discussed in chapter 4. The ocean is a global domain with a horizontal resolution of 2° x 2° and 15 vertical levels. Realistic bottom topography and land masses are included in the model (Figure 5.10). In uncoupled mode, SST and SSS are restored to Levitus 1998 climatology (*Levitus and Boyer*, 1998; *Levitus et al.*, 1998) over a period of 40 days. Latitudinal and longitudinal wind stresses are restored in the same way to *Hellerman and Rosenstein* (1983) wind stress climatology.

Ice is represented in FORTE using a simple ice model. Water freezes at -2° and the salt disappears. Although not optimal, ice is present within FORTE, and the important effects on heat and freshwater exchange between the ocean and atmosphere are captured.

5.2.2 The Atmosphere

FORTE has a T42 spectral atmosphere based on primitive equations, with a horizontal resolution of 2.5° x 3.75°, and 15 σ-coordinate vertical levels. Temperature, humidity, vorticity and divergence are the prognostic variables given. The wind field is diagnosed from the vorticity and divergence variables. Convection within the model is calculated using a *Betts and Miller* (1993) scheme, which incorporates 3 cloud levels: high, medium and low. In uncoupled mode, the atmosphere exchanges temperature and freshwater fields with a 25m deep mixed layer slab ocean.

Surface boundary conditions over land regions are dealt with using the same land-surface scheme that the model employs when run uncoupled. Over ocean regions the 25 m deep mixed layer slab ocean (temperature only) used in uncoupled mode is replaced by daily averaged SST fields derived from MOMA.

5.2.3 The coupled model

Exchanges between MOMA and IGCM3 occur daily through OASIS (*Terray et al.*, 1999). The surface restoration and wind stress fields used by MOMA in stand alone mode are replaced by equivalent fields generated by IGCM3, which are passed through the coupler, OASIS. IGCM3 provides radiative, sensible and latent heat fluxes, which are calculated from the previous day's SST to replace MOMA's temperature restoration. Salinity restoration is replaced by freshwater flux provided by IGCM3. The fields are passed through OASIS, where they are adjusted to the correct resolution and format for MOMA. Windstresses are also passed to MOMA through OASIS in the same manner.

The climate produced by the model is close to steady state, with a global averaged SST drift of 0.3°C/century. The annual mean SST is reasonably well reproduced, when compared with *Levitus and Boyer* (1998) (Figures 5.1, 5.2). For the mixed-layer model experiments the ocean is replaced with a single layer slab ocean, which is able to exchange heat and fresh water with the atmosphere, but has no dynamics. The annual mean SST is again reasonable when compared with *Levitus and Boyer* (1998) (Figure 5.3), although it is consistently too cool for most latitudes, but does not show cooling at the equator relative to the tropics, which results from upwelling. Comparing the zonally averaged annual mean SST, FORTE is in reasonable agreement with *Levitus and Boyer* (1998), although the Southern Ocean is warmer than it should be (Figure 5.4).

Salinity is also well represented in FORTE compared with *Levitus et al.* (1998) (Figures 5.5, 5.6). The Southern Ocean is too salty by 0.5 at the surface, along with

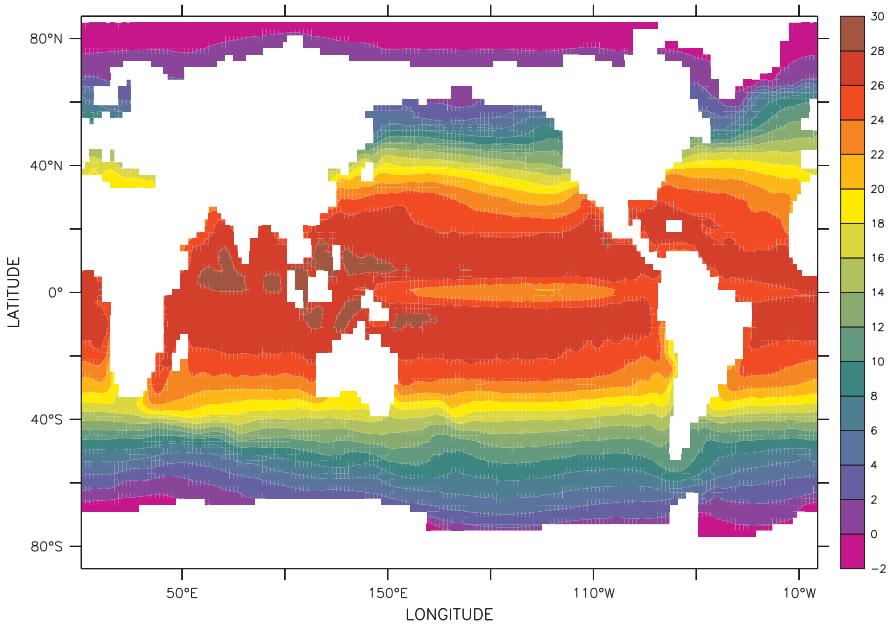

Fig. 5.1: Annual mean SST (°C) for the full ocean version of FORTE after 80 years of control integration.

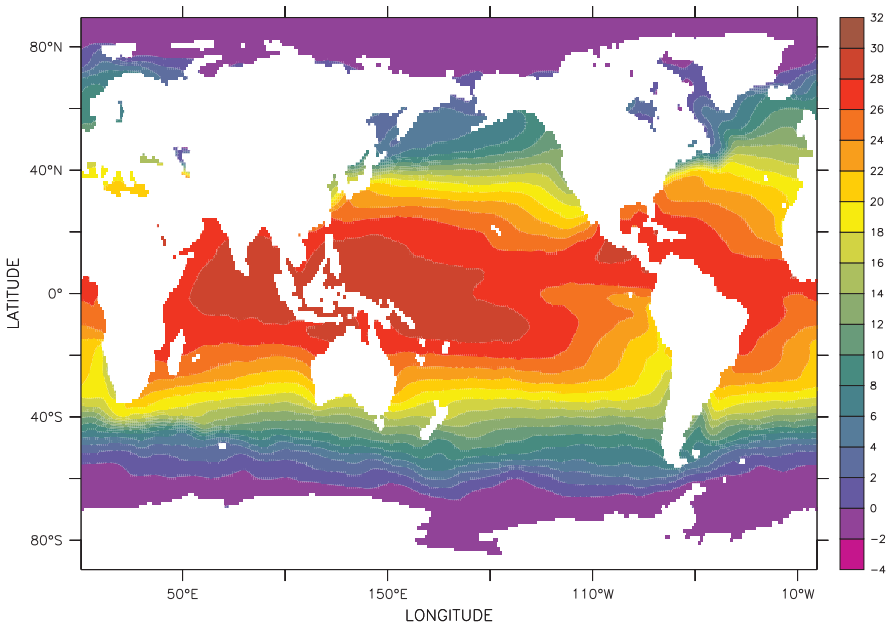

Fig. 5.2: Annual mean SST (°C) from the *Levitus and Boyer* (1998) dataset.

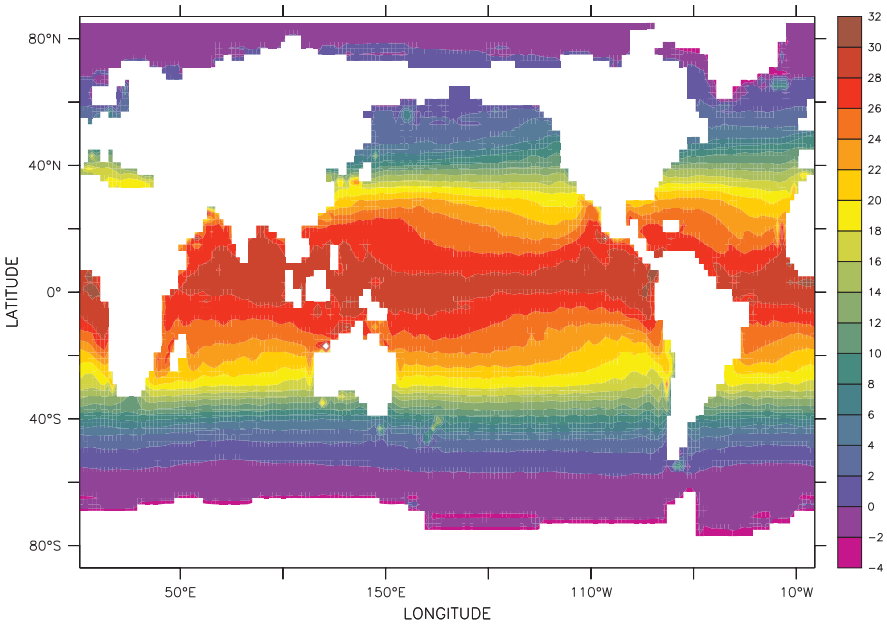

Fig. 5.3: Annual mean SST (°C) for the mixed layer version of FORTE.

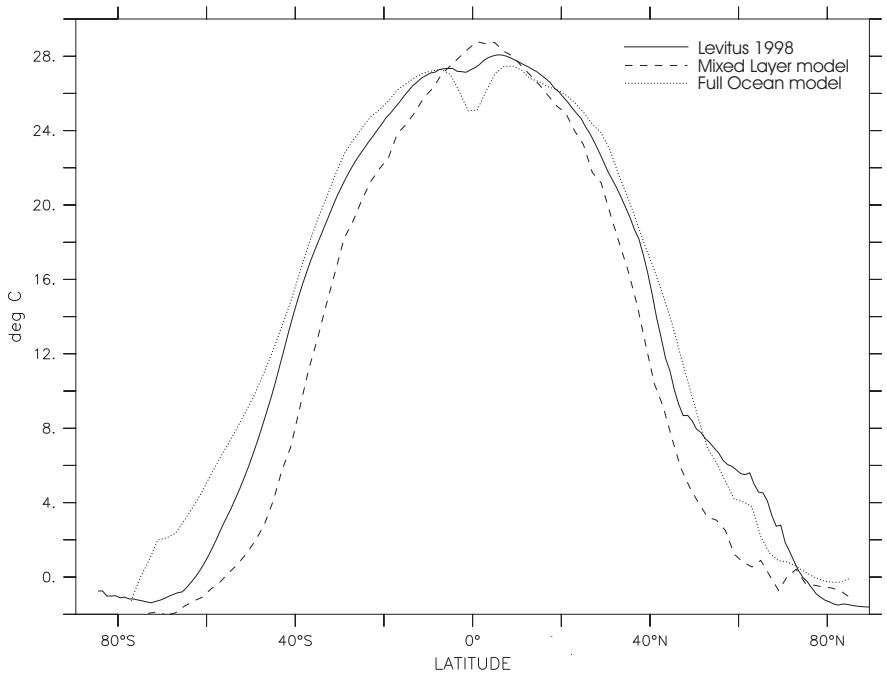

Fig. 5.4: Comparison of zonally averaged SST (°C) for *Levitus and Boyer* (1998), full ocean FORTE after 80 years of control integration, and mixed layer FORTE.

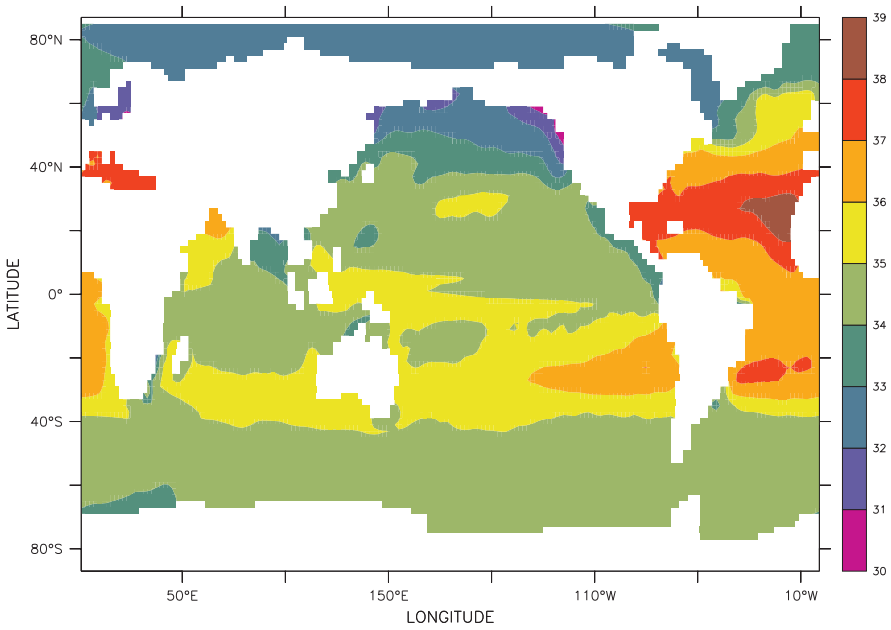

Fig. 5.5: Annual mean SSS for the full ocean version of FORTE after 80 years of control integration.

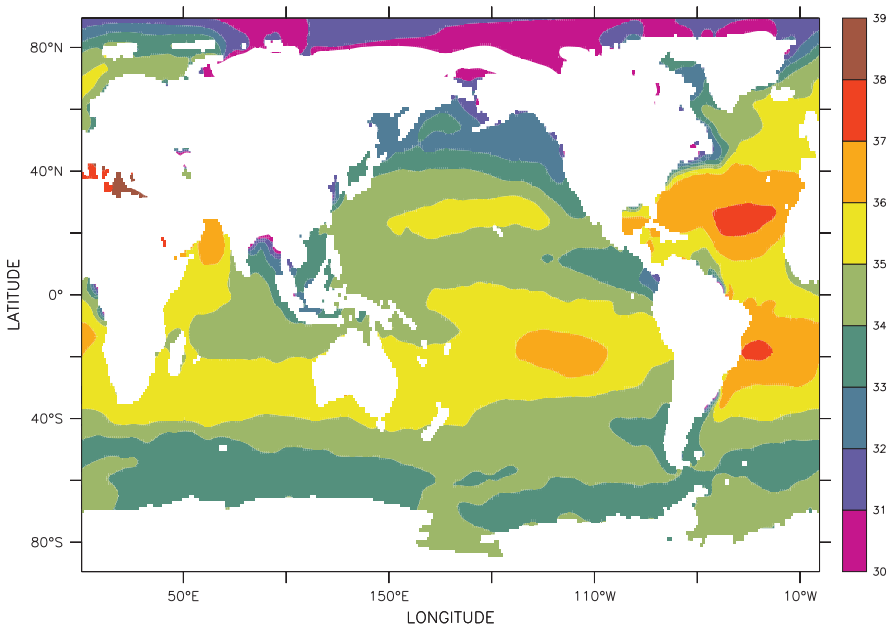

Fig. 5.6: Annual mean SSS from the *Levitus et al.* (1998) dataset.

the equator and some of the northern hemisphere high latitudes (Figure 5.7). Salt is not represented in the mixed-layer model.

Meridional overturning is well represented in the FORTE ocean. The Atlantic ocean shows a strong MOC, with a maximum of 25 Sv, 30°N at 1000 m depth (Figure 5.8). The Pacific ocean shows weak upwelling throughout the northern hemisphere (Figure 5.9).

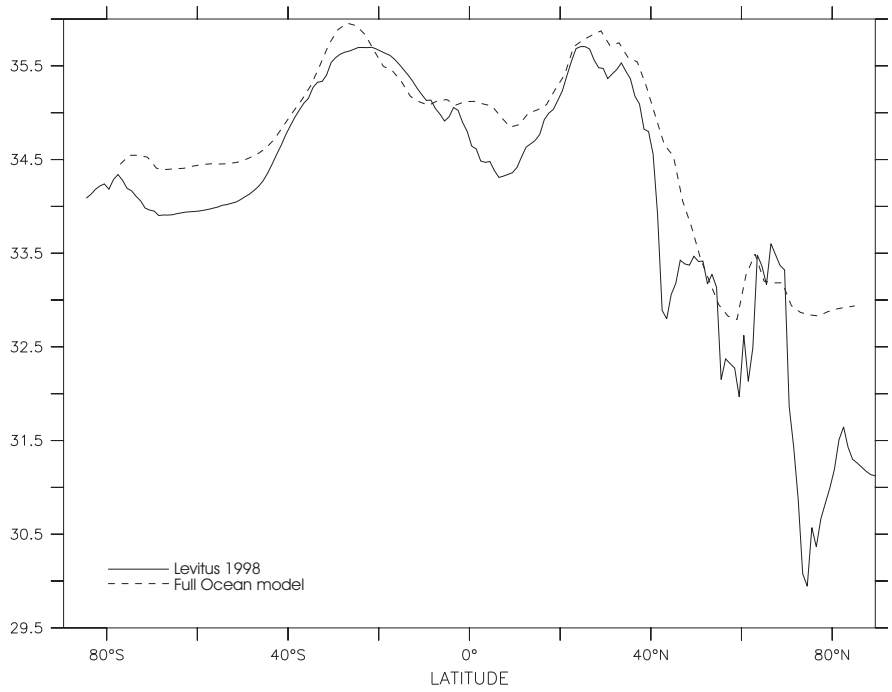

Fig. 5.7: Comparison of zonally averaged SSS for *Levitus et al.* (1998) and the full ocean FORTE.

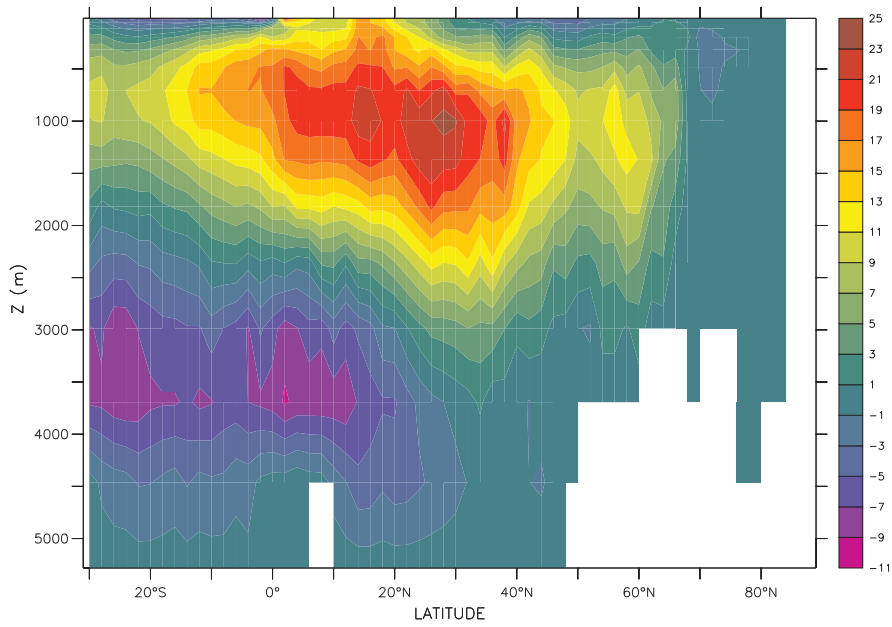

Fig. 5.8: Annual mean Atlantic meridional overturning circulation (Sv) in FORTE after 80 years of control integration.

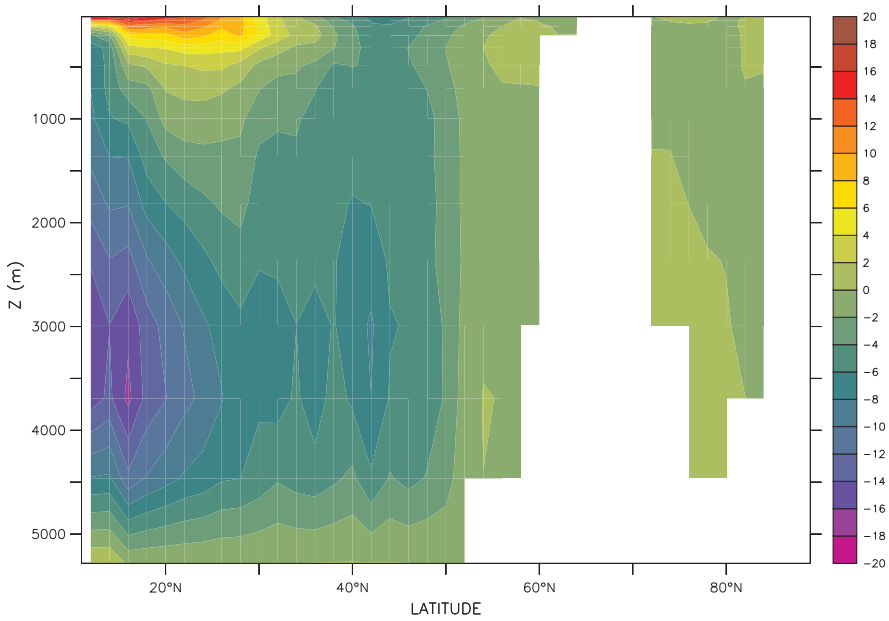

Fig. 5.9: Annual mean Pacific meridional overturning circulation (Sv) in FORTE after 80 years of control integration.

5.3 Perturbation experiments

A positive salinity anomaly was added to the Weddell Sea (60°W – 0°W, 78°S – 58°S, Figure 5.10). The location of the anomaly was chosen to approximately match that of *Ivchenko et al.* (2004), so that it was possible to qualitatively compare the results produced here to those in the idealised basin case. The upper 500 m of the region were fixed to a salinity of 36 for 30 days. At each timestep the salinity values within the region were reset to 36 during the calculation of the tracer advection and diffusion. After 30 days this constraint was removed and the model was permitted to evolve freely for the remainder of the integration. Salinity anomalies in the Southern Ocean result from sea ice formation and melting, and substantial anomalies of both sign have been observed in the Weddell Gyre occurring on a quasi-quadrennial cycle (*Venegas and Drinkwater*, 2001).

Importantly, the salinity anomaly creates a density gradient which interacts with topography to produce a barotropic wave response through the JEBAR (Joint Effect of Baroclinicity And Relief) effect (*Ivchenko et al.*, 1997). Without topography the $\partial H/\partial x$ term in the JEBAR equation (Equation 7.5) vanishes and JEBAR becomes zero. The close proximity of the density gradient to bottom topography, which arises from the deep convection caused by the positive salinity anomaly, enhances the JEBAR effect.

Richardson et al. (2005) find evidence of a barotropic response using a circumpolar freshwater anomaly in HadCM3. It is possible that a similar barotropic response

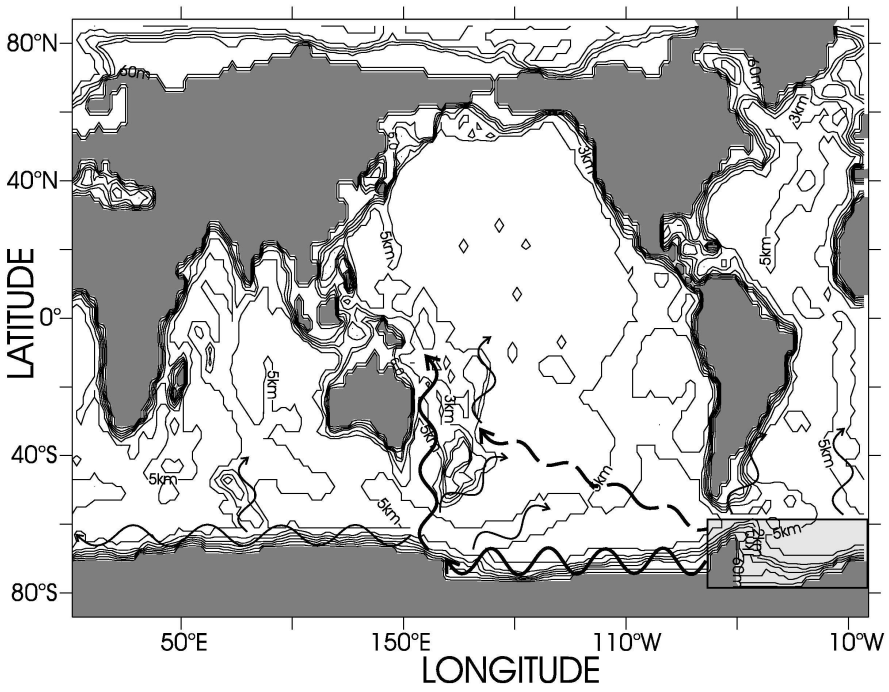

Fig. 5.10: Land mask and ocean topography from the FORTE model. Contours show depth in metres. The Weddell Sea anomaly is shaded grey. Arrows indicate the paths of the barotropic waves propagating from the anomaly. The main Kelvin wave (solid) and Rossby wave (dashed) paths discussed in the paper are in bold.

could arise from anomalies in wind stress, changes in the strength of the ACC, or high latitude SST anomalies.

Anomalous convection in the Weddell Sea may also result from open ocean polynya formation (*Gordon and Comiso*, 1988). Open ocean polynyas are regions in the sea ice where the sea surface is exposed to the atmosphere. Heat and moisture loss to the atmosphere results in strong convection, which allows the polynya to persist. Open ocean polynyas occur less frequently than sea ice concentration anomalies, but are potentially able to create much stronger anomalies. Polynyas can also form near coastlines, where offshore winds blow sea ice away from the coast as it forms, keeping the surface of the ocean exposed to the atmosphere. These are more frequent (often seasonal) and are known as coastal polynyas, but do not produce the same deep convection as open ocean polynyas. It is not possible to simulate an open ocean polynya within FORTE due to the crude ice model, which forms ice when the water temperature falls below -2°.

The positive salinity anomaly applied to FORTE equates to an average increase in salinity of 1.25 throughout the source region. This is stronger than is realistically possible, but it is only applied for a short period of time. Interannual variability of SSS with amplitudes as large as 0.5 has been observed at Rothera Station, just west of the Antarctic Peninsula (*Hickey and Weaver*, 2004). *Ivchenko et al.* (2004) experimented with different magnitudes of salinity anomaly, ranging from 0.25

to 2, and applied the anomalies for durations ranging from two months to a year. The model responses varied in amplitude and the time at which the peak signal arrived at the equator varied from three to seven months, but all model results were qualitatively similar.

The salinity anomaly in the full-ocean model results in strong SST anomalies within the anomaly region. The mixed-layer ocean and atmosphere are not capable of responding directly to salinity anomalies, so in order to provide the mixed-layer atmosphere with a forcing equivalent to that received by the full-ocean model atmosphere, the SST anomaly from the source region is stored daily and imposed onto the mixed-layer model ocean in the same location.

A 5 run ensemble was completed for the 360 day control and perturbation runs in both the full-ocean and mixed-layer models, with monthly mean output of the diagnostic fields. Analysing the ensemble mean, as opposed to an individual integration, reduces the level of atmospheric variability, whilst maximising the signals which arise from the ocean anomaly. Atmospheric variability affects both the atmosphere and the surface mixed layer of the ocean and can obscure the signal from the ocean anomaly, making it difficult to trace the propagation. The same ocean restart field was used for each ensemble member. For each member, a perturbation was introduced to the atmospheric restart field by advancing the atmospheric model by one day. Two 5 day runs (control and perturbation) of the full-ocean version of the model were also completed with data output every 20 minutes. The high temporal resolution enables the barotropic wave response to be resolved. The first run (BTR-1) covered days 0 – 5, and the second (BTR-2) covered days 30 – 35. These high temporal resolution runs were not ensembles. Anomaly fields are defined as the difference between the perturbation run ensemble mean and the control run ensemble mean.

5.4 Results

Use of the high temporal resolution run (BTR-1) allows detailed examination of the initial response over the first 5 days. Deep convection can be seen as an immediate response to the salinity anomaly, because the ocean in this region is weakly stratified. Rapid overturning leads to significant changes of both sign in the source region SST within a day. The free surface height drops rapidly in the Weddell Sea, reaching its minimum after a few days. The perturbation to the free surface excites a rapidly propagating barotropic wave response which propagates across the Pacific in a day (Figure 5.11), and can be seen to reach all areas of the global ocean within a few days.

Introducing the salinity anomaly creates a density anomaly in the surface waters,

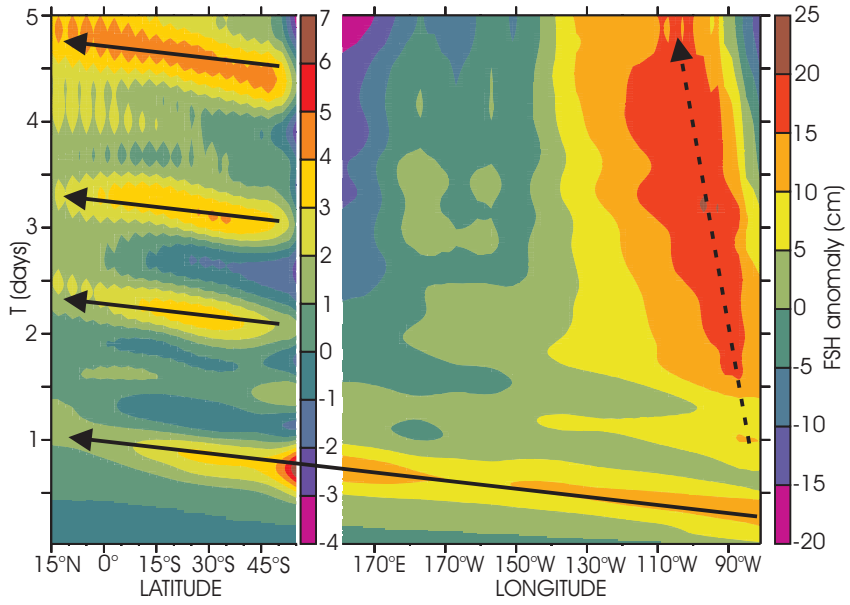

Fig. 5.11: Distance-Time plot of Free Surface Height anomaly (cm) along 60°S and 160°E for the initial 5 days after the introduction of the salt anomaly to the Weddel Gyre for the FO model run (BTR-1) of the FORTE coupled climate model. Barotropic Kelvin waves are indicated with solid arrows. The baroclinic Kelvin wave response is indicated with a dashed arrow.

which initiates a gravity wave which propagates at a speed of $c = \sqrt{gh} = 225\ \mathrm{m\,s^{-1}}$. Following this initial response, barotropic Kelvin waves propagate along the coast of Antarctica and equatorward along the Atlantic coast of South America. The delay between the initial wave response and the first Kelvin waves suggest different forcing mechanisms operate for the different waves.

Barotropic Rossby waves propagated directly across the Pacific basin to the western boundary in the idealised basin experiment run by *Ivchenko et al.* (2004). In FORTE topography has a significant effect on the propagation of barotropic Rossby waves. The East Pacific Rise weakens the propagating signal, although barotropic Rossby wave energy can still be seen crossing the Pacific and reaching the western boundary.

Wave energy is channelled along the Southern Ocean in the form of coastally trapped barotropic Kelvin waves. The Kelvin waves propagate with a velocity of 125 $\mathrm{m\,s^{-1}}$. The velocity should be 225 $\mathrm{m\,s^{-1}}$, almost double that observed in the model. The discrepancy is largely due to the unavoidably large viscosity used in the model (*Davey et al.*, 1983). The no-slip condition that is naturally implemented in the Arakawa 'B' grid also reduces the velocity of the modelled waves (*Hseih et al.*, 1983). The barotropic wave response is well resolved, even with a 2° resolution ocean model, so the wave velocity is not dramatically affected by the coarse resolution of the FORTE ocean.

Energy is removed from the Southern Ocean by a succession of barotropic waves

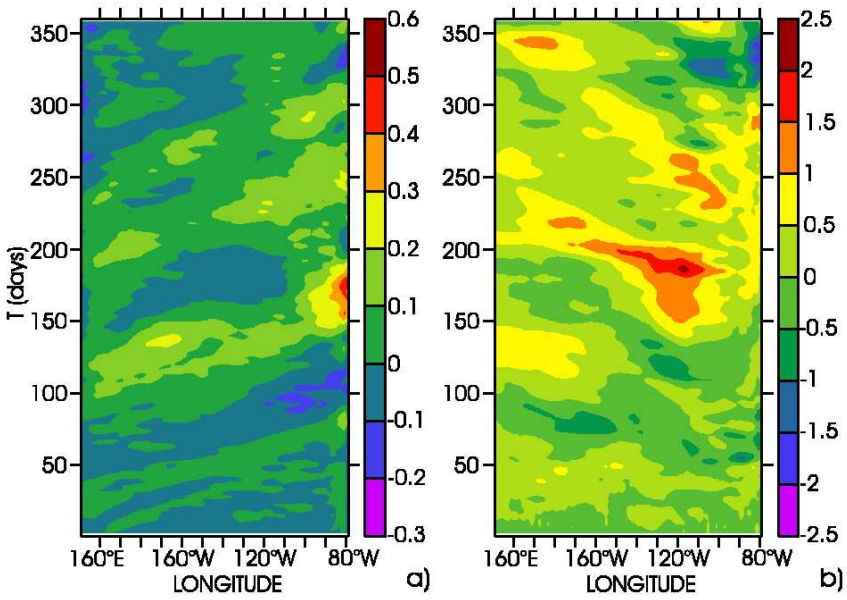

Fig. 5.12: Longitude-Time plot of a) subsurface temperature anomaly (500 m), b) SST anomaly along the equatorial Pacific for the first 360 days after the introduction of the salt anomaly to the Weddel Gyre for the FO model run (BTR-1) of the FORTE coupled climate model.

which are seen to propagate along ridge features such as the Mid-Atlantic Ridge and the East Pacific Rise. Barotropic waves follow topographic ridges across the Southern Ocean to Australia and New Zealand and follow the western boundary of the Pacific to the equator (Figure 5.11). The clearest barotropic response comes from the start of the perturbation. Successive waves are weaker, but are still clearly visible. The waves have a period of around 1 day. Examination of the second high temporal resolution run (BTR-2), not shown, reveals that the same barotropic response persists. The strongest response remains in the Southern Ocean, although wave propagation can clearly be seen in the Pacific, Atlantic and Indian ocean basins. Energy reaches the western boundary of the Pacific in the barotropic mode through both Rossby wave and Kelvin wave propagation.

Data from the lower temporal resolution full-ocean model simulation show baroclinic Kelvin waves propagating eastwards along the thermocline at the equator, crossing the Pacific in 70 days (Figure 5.12a), which agrees with theory. Propagation begins almost immediately after the start of the run. The waves reflect from the eastern boundary as a series of Rossby waves that are easily visible in the SST (Figure 5.12b). Propagation of these Rossby waves does not begin until the Kelvin wave first arrives at the eastern boundary. The mixed-layer model response displays no evidence of such a disturbance in the SST.

The full-ocean model shows significantly more response in the equatorial and tropical region than the mixed-layer model, whilst similar responses in the Southern Ocean and the NH high latitude ocean occur in both models

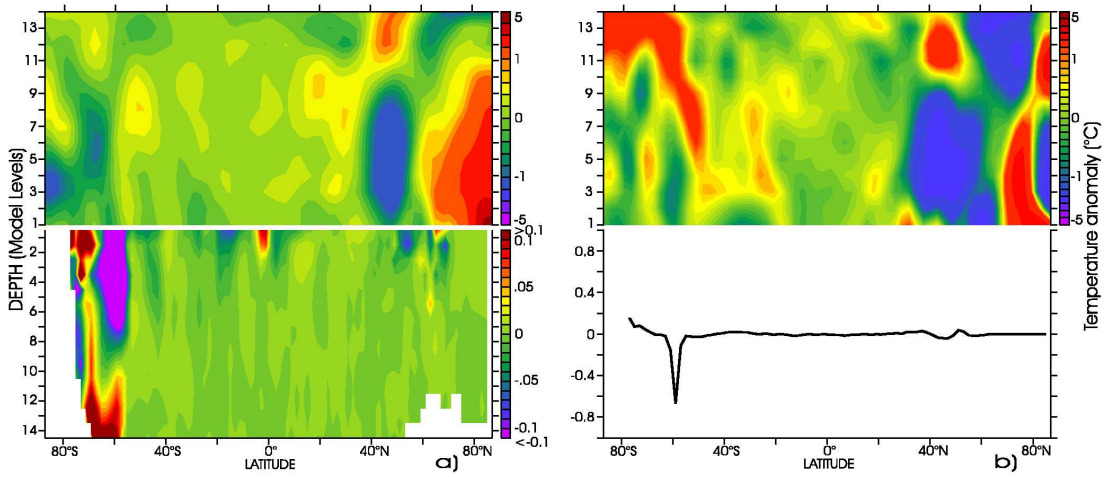

Fig. 5.13: Snapshot of zonally averaged temperature anomalies (°C) one month after the introduction of the salt anomaly to the Weddel Gyre for ocean (lower) and atmosphere (upper) in a) the full-ocean model, and b) the mixed-layer model.

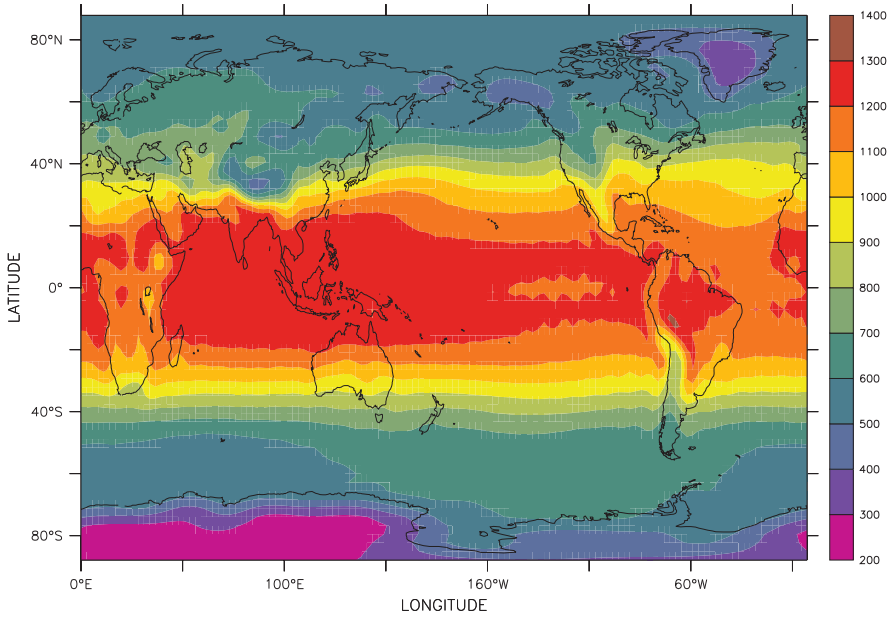

Fig. 5.14: Temporally and vertically averaged atmospheric temperature variance for the 360 day control integration of the full-ocean model.

(Figure 5.13). Equatorial SST anomalies greater than 0.1°C appear after one month in the full-ocean model, similar in magnitude to the anomalies seen in the NH high latitudes. The mixed-layer model has no distinguishable temperature anomalies in the equatorial region at this time. The NH response seen in both models also appears one month after the start of the integration. The signal at the equator in the full-ocean model continues to strengthen until the peak SST anomaly occurs after 180 days. No significant signal is seen in the tropical atmosphere until this time.

Atmospheric temperature variance in the control integration is much greater in

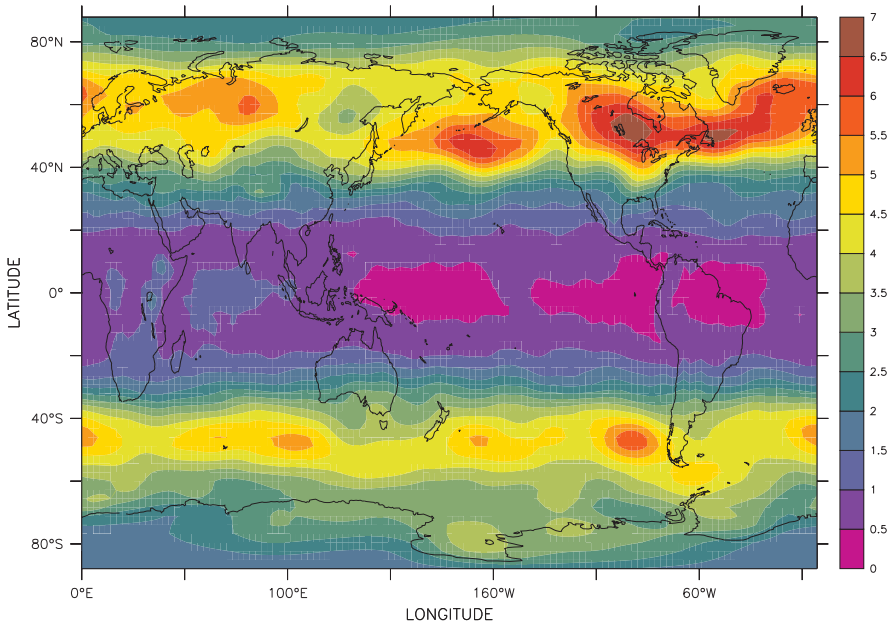

Fig. 5.15: Temporally and vertically averaged anomalous atmospheric temperature variance (perturbation - control) for the 360 day integrations of the full-ocean model.

the tropics due to strong temperature changes and the latitudinal shift of the ITCZ (Figure 5.14). The anomalous atmospheric temperature variance is largest in the extra-tropics and high latitudes (Figure 5.15). Equatorial and tropical atmospheric temperature anomaly variation in the full-ocean model is very small, compared with anomalies in excess of 1°C seen in the extra-tropics and polar regions. Atmospheric responses to the perturbation are similar in both the full-ocean and mixed-layer models throughout the duration of the run (Figure 5.13). The first remote atmospheric temperature response to the perturbation is seen in the NH high latitudes. This response appears after 30 days in both the mixed-layer and full-ocean models, with the NH high latitude atmosphere influencing the SST below it within 2 to 3 days. Following the path of the anomalies in the atmosphere over time suggests the existence of a 'bridge' over the tropical latitudes. The first anomaly appears in the source region. It then extends upwards and equatorwards before descending to produce an anomaly in the high latitude NH surface air temperature, quickly resulting in an SST anomaly. Energy crosses the equator from south to north as a wave propagation along the top of the model atmosphere (*Tomas and Webster*, 1994). The 'bridge' can be seen to form before the anomaly has dispersed around the high latitude southern hemisphere, which takes around 50 days. No significant equatorial SST response occurs in the ML model (Figure 5.16).

Heat storage in the mixed-layer model is far smaller than in the full-ocean model, resulting in anomalously large SSTs which can produce a positive feedback with the overlying atmosphere. This results in the mixed-layer model having higher

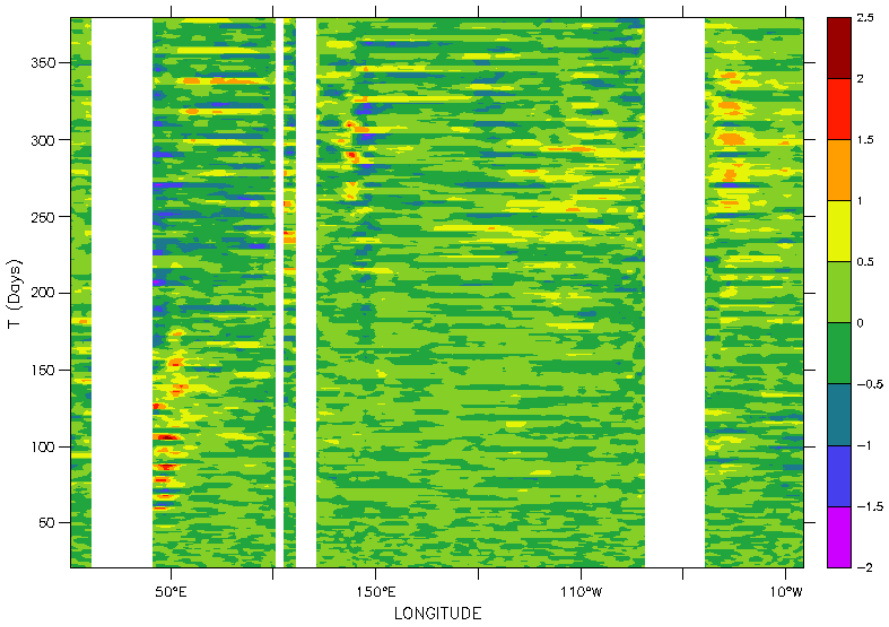

Fig. 5.16: Hovmöller plot of equatorial SST anomalies (°C) for the first 360 days after the introduction of the anomaly to the Weddel Gyre in the mixed layer model. The Rossby wave response returning from eastern Pacific boundary, which is seen in the full-ocean model, does not exist.

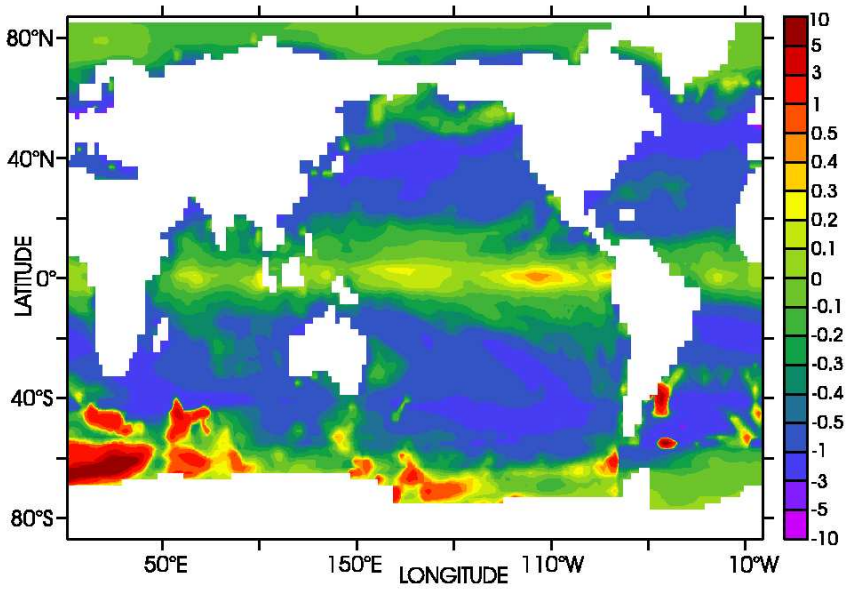

Fig. 5.17: Time and ensemble averaged values of anomaly of T^2 (T^2(FO) - T^2(ML)) in units of °C^2, with a non-linear scale. Data is averaged over the 360 day integration starting from the introduction of the positive salinity anomaly to the Weddel Gyre. Positive(negative) values indicate larger FO(ML) anomalies.

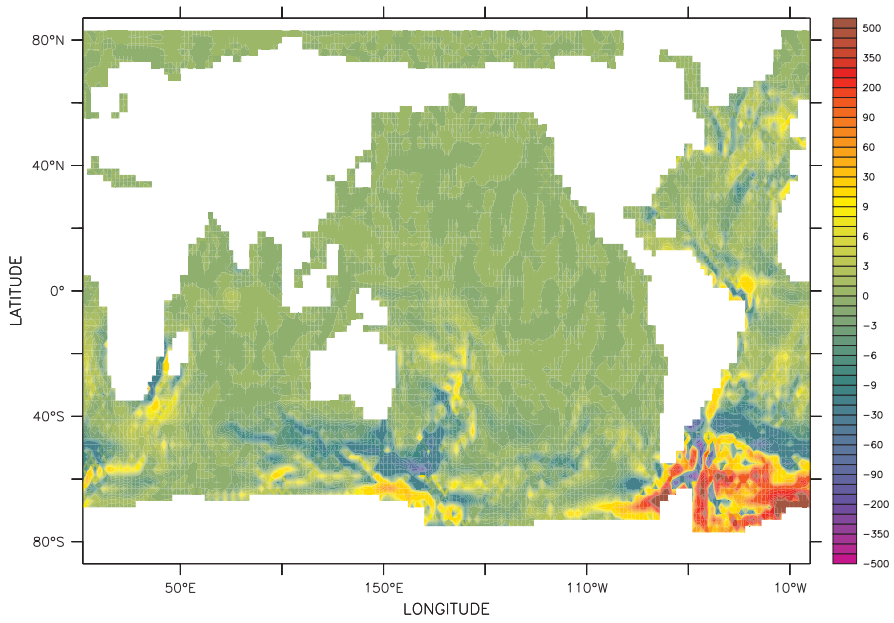

Fig. 5.18: Barotropic kinetic energy (kg m^{-1} s^{-2}) 50 days after the introduction of the positive salinity anomaly to the Weddel Gyre in the FORTE model.

amplitude SST variance compared to the full-ocean model, which is able to advect and diffuse heat into a far greater volume of water and prevent the occurrence of excessive SSTs. The high temperature variance in the mixed-layer model dominates the mid-latitudes (Figure 5.17). The greater response of the full-ocean model to the anomaly in the Southern Ocean is clear. It is also seen to dominate the equatorial region, as well as some locations in NH high latitude Pacific and Atlantic. Topographic features which extend equatorward from the Southern Ocean, such as the Mid-Atlantic Ridge and the Kerguelen Archipelago, also show high levels of energy.

5.5 Energy budget analysis

Analysis of the kinetic and potential energy of the ocean is used to help clarify the complex process of wave propagation and energy exchanges occurring in the Pacific. Volume averaged values of barotropic and baroclinic kinetic energy, available potential energy and potential energy anomaly are calculated throughout the domain.

All energy fields show strong signals in the source region of the anomaly, starting immediately. Within 14 days the barotropic kinetic energy has propagated around Antarctica, extending away from the Southern Ocean along topographic ridge features such as the Crozet and Kerguelen archipelagos and the Mid-Atlantic Ridge. The signal strengthens over time, and is well defined after 50 days (Figure 5.18). Although the perturbation is only active for 30 days the peak

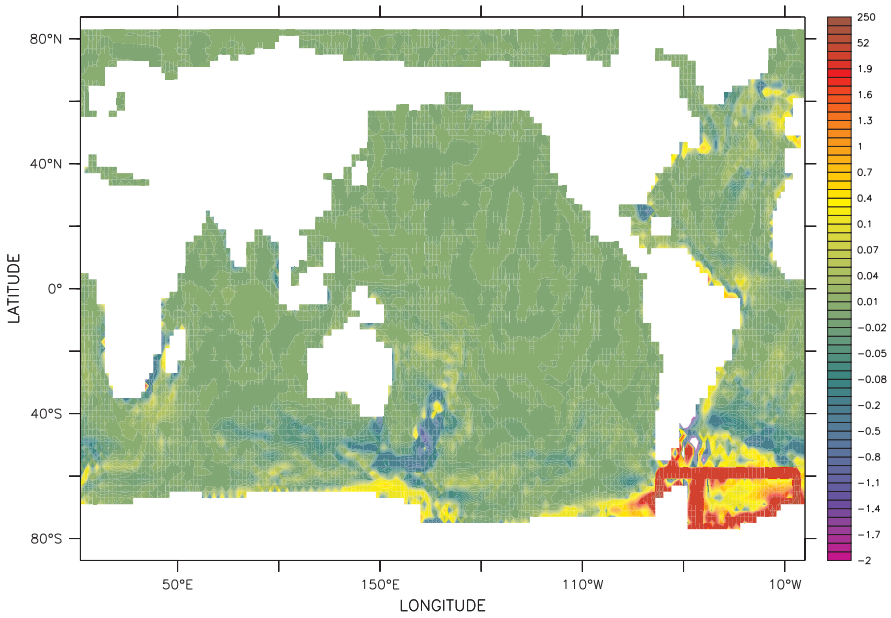

Fig. 5.19: Baroclinic kinetic energy ($\mathrm{kg\,m^{-1}\ s^{-2}}$) 50 days after the introduction of the positive salinity anomaly to the Weddel Gyre in the FORTE model.

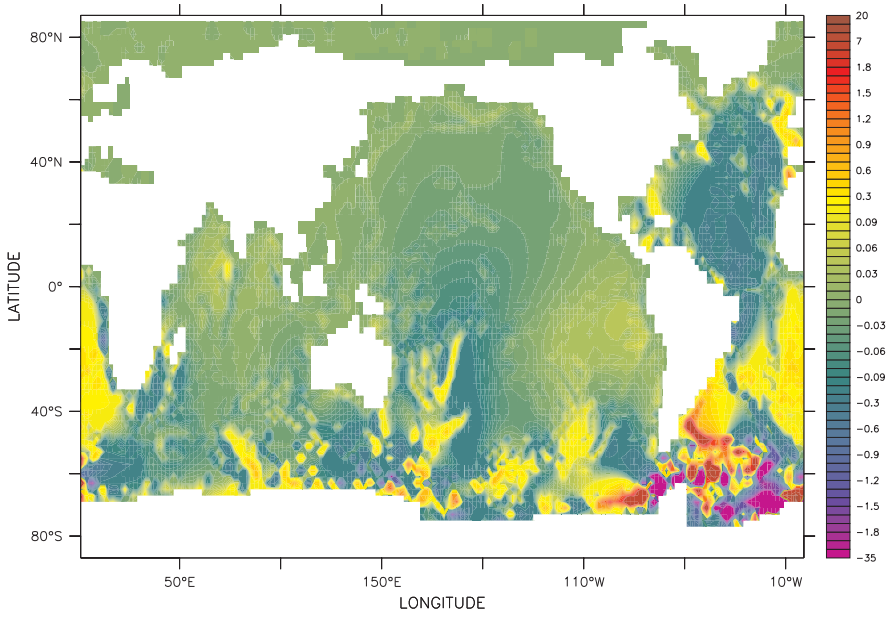

Fig. 5.20: Amplitude of the JEBAR term ($\mathrm{kg\,m^{-1}\ s^{-3}}$) 50 days after the introduction of the positive salinity anomaly to the Weddel Gyre in the FORTE model.

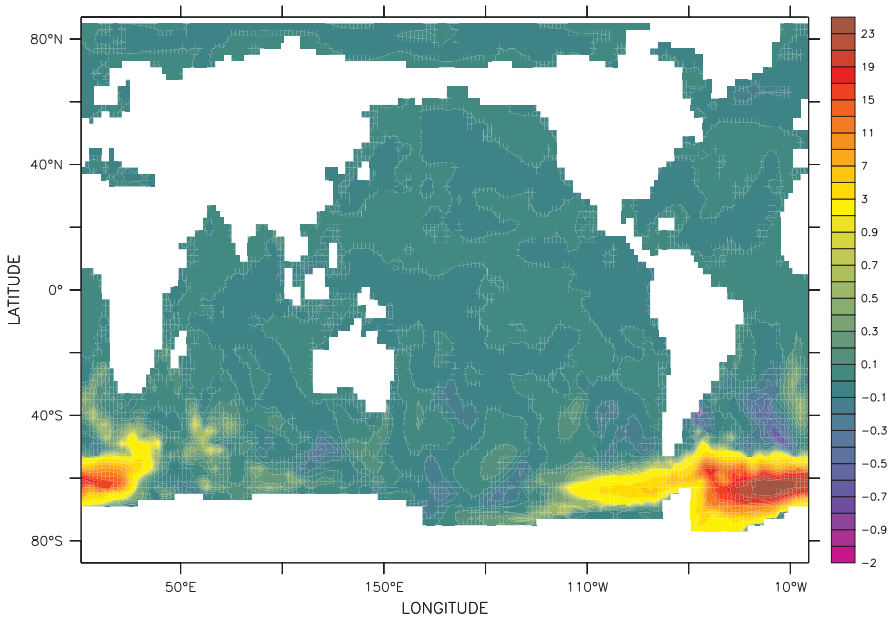

Fig. 5.21: Potential energy (kg m^{-1} s^{-2}) 180 days after the introduction of the positive salinity anomaly to the Weddel Gyre in the FORTE model.

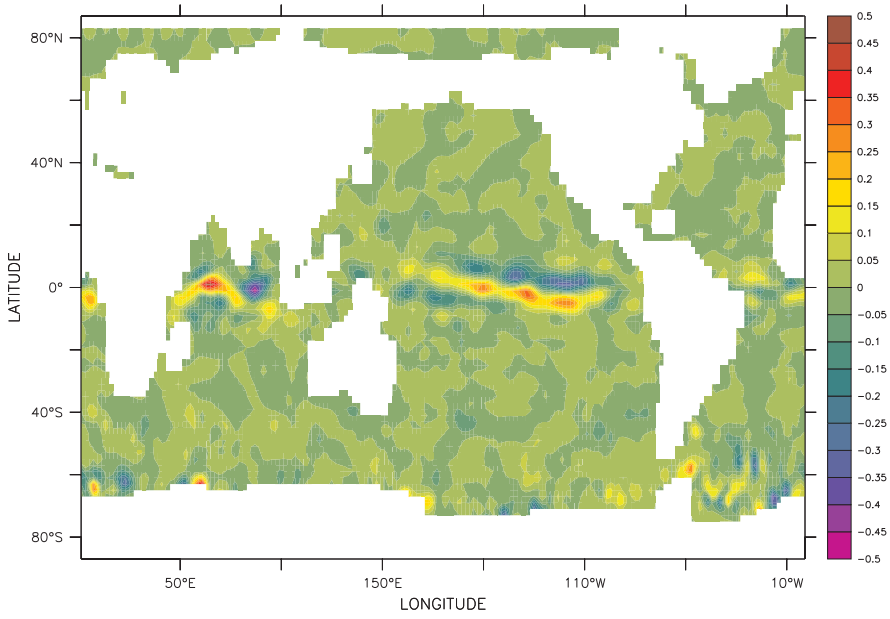

Fig. 5.22: Amplitude of the buoyancy term (kg m^{-1} s^{-3}) 180 days after the introduction of the positive salinity anomaly to the Weddel Gyre in the FORTE model.

in the barotropic energy at the source of the anomaly is at 50 days. Energy is transferred from the baroclinic to the barotropic mode of propagation within the source region. After the 50 day peak energy levels decline rapidly over the next 50 days as energy disperses from the source region.

Baroclinic kinetic energy shows a similar evolution to the barotropic in the Southern Ocean, although high values along ridge features and changes in topography are much better defined due to the much smaller Rossby radius associated with internal wave propagation (Figure 5.19). The JEBAR term shows a similar spatial pattern to the kinetic energy terms (Figure 5.20). Potential energy anomalies are slower to develop, but their spatial extent is similar to that of the barotropic kinetic energy. Interestingly, there is a positive (east) and negative (west) response extending equatorward along the Mid-Atlantic Ridge (Figure 5.21), very similar to the response of the idealised MOMA basin with the temperature anomaly above the ridge (Figure 6.16). The buoyancy term is dominated by a pulsing along the equator. This is attributed to w, the vertical velocity. Anomalies along the equator appear after around 30 days and persist throughout the remainder of the integration (Figure 5.21). Along the equator the period of the signal is predominantly 5 days. Off the equator (+/- 10 – 15°) there is a strong 20 day period that is easily observed in an animation. The ΔT^2 plots show the same period. It is not obvious what gives rise to these periods. They are the same for all ocean basins. All fields show that the majority of the energy remains in the Southern Ocean throughout the integration, and propagates around the coast of Antarctica as barotropic, and later baroclinic, Kelvin waves. Eastward advection of energy from the anomaly can be seen in the kinetic and potential energy fields (Figure 5.21).

In some high latitude NH locations in the Atlantic and Pacific basins, around Iceland for example, signals appear within 7 – 14 days. These are probably a response to the atmospheric anomalies. After 20 days increases in barotropic kinetic energy can be seen to form here also. The NH Atlantic signal arrives 2 days before the Pacific signal. These NH signals continue to grow in barotropic kinetic energy and propagate equatorward (south) along the western boundaries in both basins. Potential energy anomalies only occur in the North Atlantic around Iceland.

Propagation of barotropic Rossby waves can be seen between the East Pacific Rise and the western Pacific boundary. Barotropic kinetic energy in the Southern Ocean remains strong throughout the 360 day integration. Baroclinic kinetic energy along the equator and around Indonesia is relatively strong, and remains so throughout the integration. Some barotropic kinetic energy can be seen along the equator, mostly westward propagating or close to land boundaries, but amplitudes are considerably smaller than in the Southern Ocean or at NH

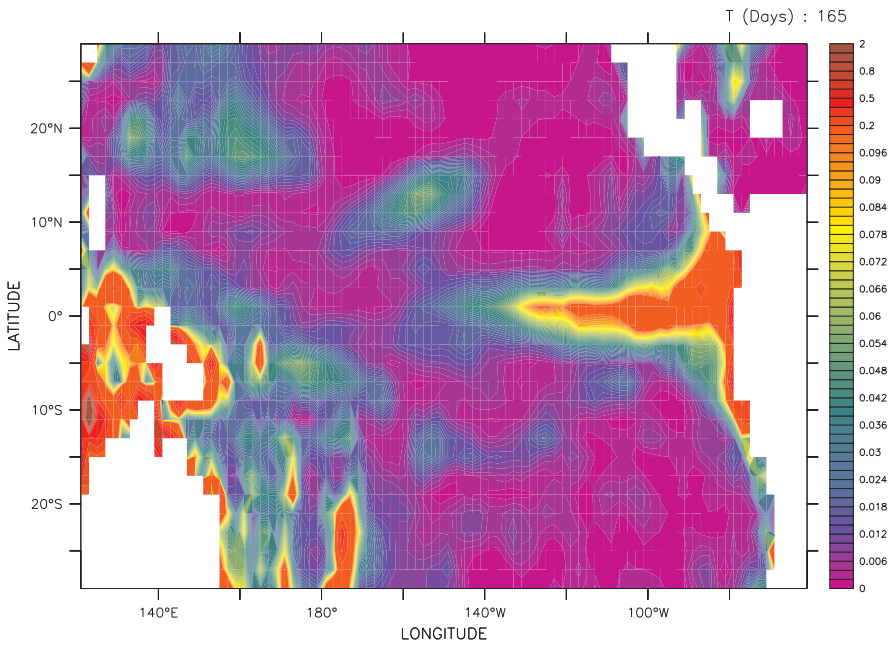

Fig. 5.23: Available potential energy ($\mathrm{kg\,m^{-1}\,s^{-2}}$) in the tropical Pacific after 165 days.

high latitudes. Energy in the NH is less persistent in both the barotropic and baroclinic modes. Rapid activity along the equatorial waveguide can be seen in the potential energy, although values are small. Available potential energy, which appears very similar spatially to the potential energy anomaly globally, shows a Rossby wave structure extending away from the eastern boundary in the tropical Pacific (Figure 5.23). This signal is distinguishable from around 100 days into the integration, which correlates with the arrival of the first strong baroclinic Kelvin wave at the eastern boundary (Figure 5.12), onwards.

The JEBAR term does not highlight any clear exchange of energy along the western Pacific boundary. Exchange of energy between the barotropic Kelvin and Rossby waves arriving at the boundary and the baroclinic mode of propagation may be smaller than suggested by *Ivchenko et al.* (2004), and in fact the main mechanism for forcing a strong equatorial response could be more like the one described by *Reznik and Zeitlin* (2006). In their experiment, the energy which causes an exponentially growing baroclinic response along the equator comes directly from the barotropic mode. Alternatively, the barotropic signal could excite the release of potential energy into the baroclinic mode, which would explain why the buoyancy term shows such a strong response along the equator in the FORTE model.

5.6 Summary and Discussion

The results demonstrate two distinct responses from the salinity anomaly and the contrasting roles of the ocean and atmosphere are defined.

The ocean mechanism identified is similar to that described in the idealised experiments carried out by *Ivchenko et al.* (2004). The energy from the anomaly in the Weddell Sea arrives at the western Pacific boundary via two ocean wave mechanisms. Barotropic Rossby waves transmit the signal directly across the Pacific Ocean. Barotropic Kelvin waves follow the Antarctic coastline and form waves which propagate along the ridge systems that extend away from the Southern Ocean and connect with land masses further north. The Kelvin and topographic wave response which transmits much of the signal to the equator in FORTE may not have appeared in the idealised model basin used by *Ivchenko et al.* (2004) due to the absence of topographic ridges spanning the Southern Ocean between Antarctica and the land mass forming the western boundary. Waves propagate along these ridges which provide a connection between Antarctica and the land masses in the southern hemisphere.

Analysis of the energy budget has clarified the mechanism. The increase in salinity caused by the anomaly drives deep convective overturning in the Weddell Sea and Drake Passage, creating strong kinetic and potential energy anomalies. Interaction between the convection and the bottom topography allows energy exchange between the baroclinic and barotropic modes of propagation, which excites a barotropic wave response that propagates to the western Pacific. Energy continues to be transferred to the barotropic mode some time after removing the anomaly, and peaks 50 days into the integration. Upon reaching the western Pacific, interaction of the barotropic signal with the boundary and topography transfers energy to the baroclinic modes, generating an equatorward baroclinic Kelvin wave response. At the equator the signal then propagates eastwards across the Pacific. Poleward propagating Kelvin waves are formed at the eastern boundary, which in turn form westward propagating Rossby waves which carry energy westward into the basin interior. The equatorial response is very rapid (order of days) due to the involvement of the barotropic mode. Initially the amplitude of the response is weak, but the cumulative effect of a succession of barotropic waves bringing energy to the western boundary results in strong changes in SST. The strongest SST anomaly in the equatorial Pacific occurs 6 months into the model run, with an amplitude of 2°C.

A recent paper by *Reznik and Zeitlin* (2006) offers a useful explanation for the mechanism seen here in the FORTE model. *Reznik and Zeitlin* (2006) describe the equatorial waveguide as "semi-transparent", meaning that it is possible for

barotropic waves to freely propagate across the equator. The barotropic wave excites a resonance in the equatorial waveguide, which results in the formation of an along equator baroclinic response. The barotropic signal need not be strong to excite a strong baroclinic response, and initially the baroclinic signal is seen to grow exponentially. In the FORTE results we see a train of weak barotropic waves propagating from the source of the anomaly to the equator, with a period of 1 day. After 1 month anomalies in SST are visible at the equator and the signal strengthens to produce the 2°C anomaly seen after 6 months. *Reznik and Zeitlin* (2006) continue to explain that the growth of the baroclinic response is arrested by the development of a secondary barotropic wave which is formed by the baroclinic waves. It is not possible to see this secondary barotropic response in the FORTE data due to insufficient temporal resolution in the data. It is also likely to be small compared to the anomalies caused by the baroclinic response and atmospheric interaction during the later stages of the model integration.

The atmospheric response is shown to affect the NH. Strong SST anomalies formed in the source region perturb the atmosphere and excite an atmospheric Rossby wave response. Rossby waves in the upper troposphere transmit the energy across the equator and into the NH high latitudes (*Tomas and Webster*, 1994). After 30 days SST anomalies in the NH high latitudes are seen. IGCM3, the atmosphere used in FORTE, is capable of producing Rossby waves, but at daily temporal resolution the propagation is not easily identified and can not be attributed to the anomaly introduced into the Weddell Gyre with any confidence. A detailed analysis of the atmospheric response will require a higher temporal resolution dataset, which is currently not feasible.

The absence of an equatorial SST response in the mixed-layer model shows clearly that the presence of a dynamic ocean is necessary for this teleconnection between the Southern Ocean and the tropics to occur. Both the full-ocean and mixed-layer models demonstrate significant responses in the NH high latitudes, implying that the mechanism responsible for this response is predominantly atmospheric.

The anomaly applied to this model is larger than would be realistically expected, but is of very short duration. In reality significant changes in the sea ice occur on seasonal or longer timescales, resulting in weaker but more persistent anomalies. The response to the anomaly applied in these experiments is large, with equatorial SST anomalies in excess of 2°C, however *Ivchenko et al.* (2004) have shown that smaller anomalies applied for longer time periods produce similar results.

Chapter 6

Equatorial energy exchange and the influence of ocean ridges on wave propagation

6.1 Introduction

Results from the FORTE model, presented in chapter 5, show energy exchange from the barotropic to baroclinic modes at the equator. It is not clear exactly how the energy exchange occurs. A recent study by *Reznik and Zeitlin* (2006) suggests that it might be possible for a non-linear baroclinic response to occur as a result of excitation of the equatorial waveguide by barotropic waves. The results of the FORTE model presented in chapter 5 also highlight some interesting effects which arise from the interaction between planetary waves and topographic ridges. It is clear that topographic features play an important role in the rapid propagation of the signal originating from the Weddell Sea.

Section 6.2 describes a simple study using the idealised MOMA ocean basin, described and used previously in chapter 4, that examines the equatorial energy response to anomalies placed at several locations remote from the equator.

Section 6.3 examines the nature of the along-ridge propagation in a series of short model experiments where a simple Mid-Atlantic Ridge is added to the idealised MOMA ocean basin.

6.2 Energy exchange in a primitive equation model

Reznik and Zeitlin (2006) mathematically describe a mechanism which explains a transfer of energy from the barotropic to the baroclinic mode of propagation.

Forced barotropic waves are propagated across the equatorial waveguide. As they do so they excite an exponentially growing baroclinic response within the equatorial waveguide. The growth of the baroclinic response later limits itself by producing a secondary barotropic signal which propagates within the equatorial waveguide. Energy analysis of a series of short model runs using the idealised MOMA ocean basin, which was introduced in chapter 4, is used to investigate the possibility of this being the mechanism responsible for the equatorial baroclinic energy in the FORTE results. The mechanism described by *Reznik and Zeitlin* (2006) has not yet been shown to occur in a numerical model.

6.2.1 Comparison of different forcing anomalies

Anomalies are introduced directly to the temperature field within the model, which permits time varying anomalies to be applied.

To find out if the model response is sensitive to the type of forcing applied, two forcing anomalies with a daily period were compared. The time varying temperature anomalies are initially introduced at a location on the western boundary (40°N – 44°N, 0°E – 4°E), creating a series of barotropic Kelvin waves which propagate equatorward along the western boundary.

Forcing (i) is a step forcing of 0.01°C applied to the whole water column within a given area (Figure 6.1). The small amplitude minimises disturbance, whilst exciting wave propagation. Forcing (ii) is a linearly (cumulatively) increasing anomaly applied in the same way as forcing (i). It is a larger anomaly, but the changes are less abrupt (Figure 6.2).

The resulting signal and energy transfer is similar for both the temperature anomalies. Barotropic Kelvin waves are clearly visible, propagating south to the equator, and extending over 20° south of the equator, across the equatorial waveguide (Figure 6.3, 6.4).

The amplitude of the anomaly is of little importance in this instance, providing the model response remains linear. The lack of restoring conditions at the surface, or any motion of the water within the static basin, ensures that wave propagation which arises from even a very small anomaly is clearly visible.

The energy response along the equator is almost identical in structure for the two different forcing anomalies (Figure **??**). The timing of the responses is identical for all the energy values presented. The response of forcing (ii) is larger in amplitude purely due to the larger magnitude of the anomaly applied. This comparison shows that, apart from the amplitude of the response, the results are not strongly sensitive to the type of anomaly introduced to the model.

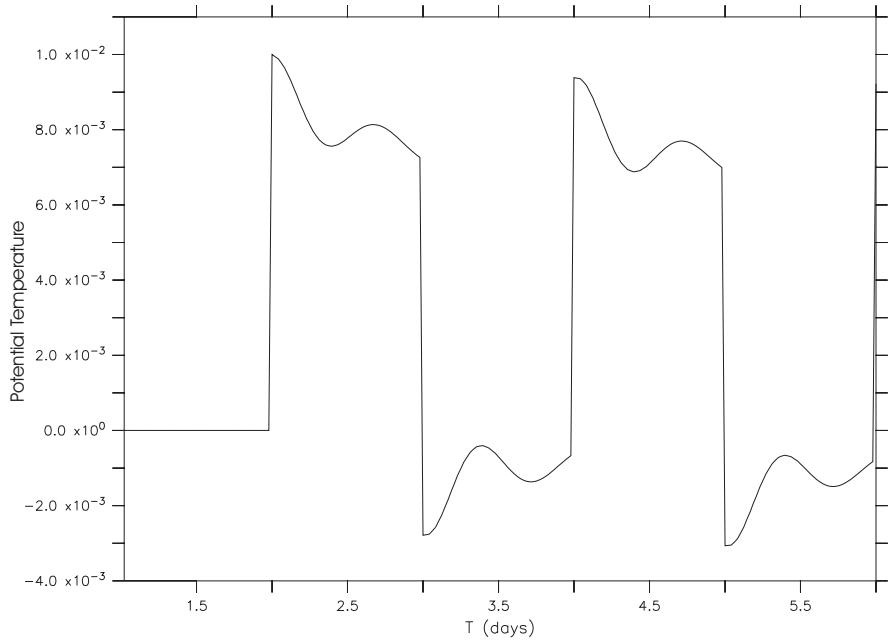

Fig. 6.1: Potential temperature anomaly (°C) in the mid-latitude forcing region (40°N) for forcing (i).

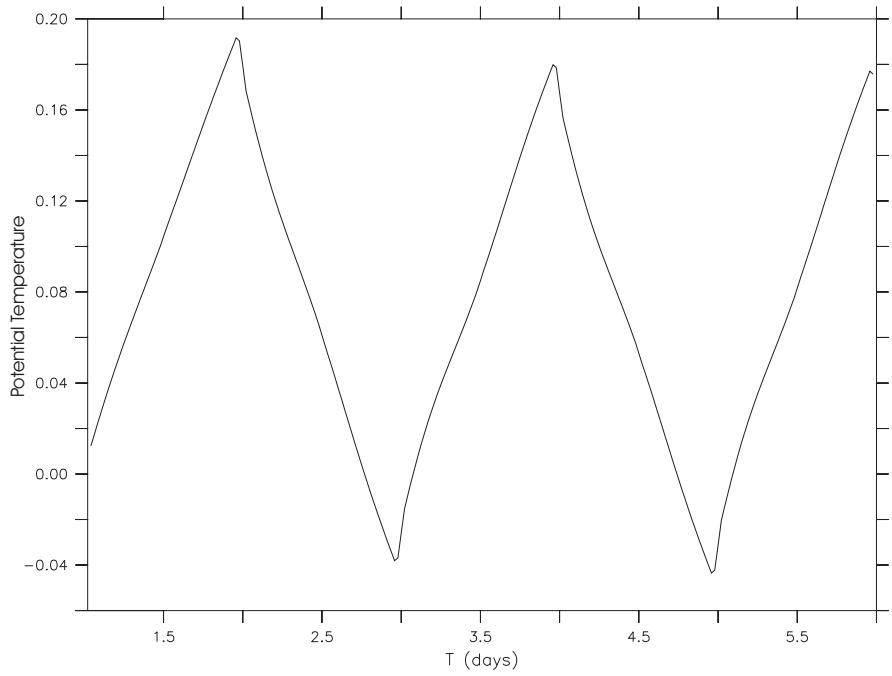

Fig. 6.2: Potential temperature anomaly (°C) in the mid-latitude forcing region (40°N) for forcing (ii).

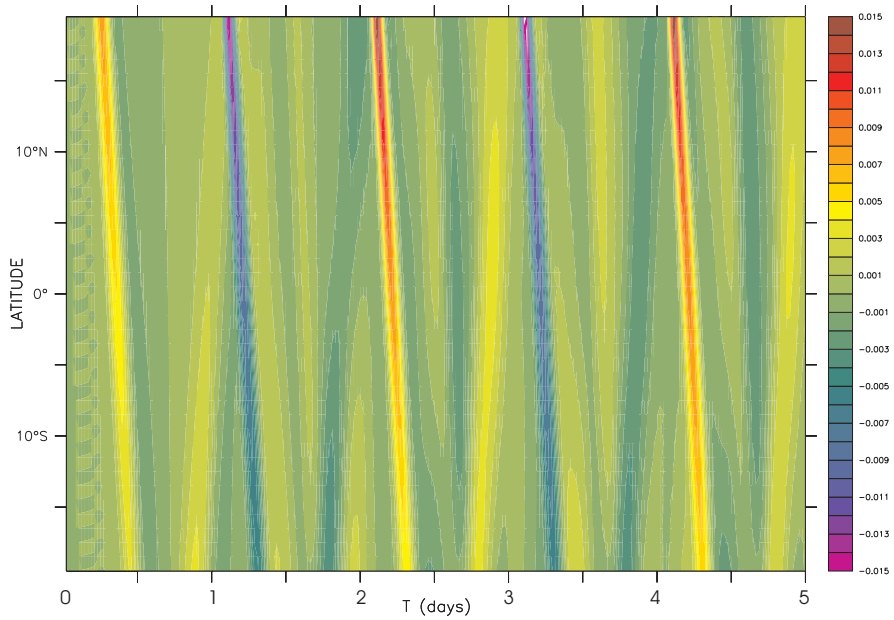

Fig. 6.3: Barotropic Kelvin wave propagation seen in FSH (in units of m), crossing the equator from mid-latitude forcing (i) in the idealised static basin.

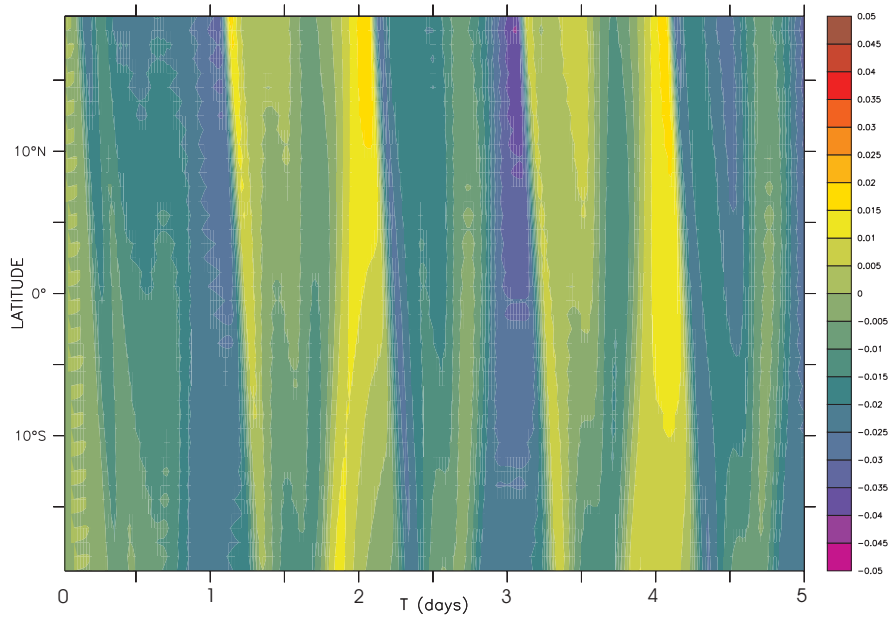

Fig. 6.4: Barotropic Kelvin wave propagation seen in FSH (in units of m), crossing the equator from mid-latitude forcing (ii) in the idealised static basin.

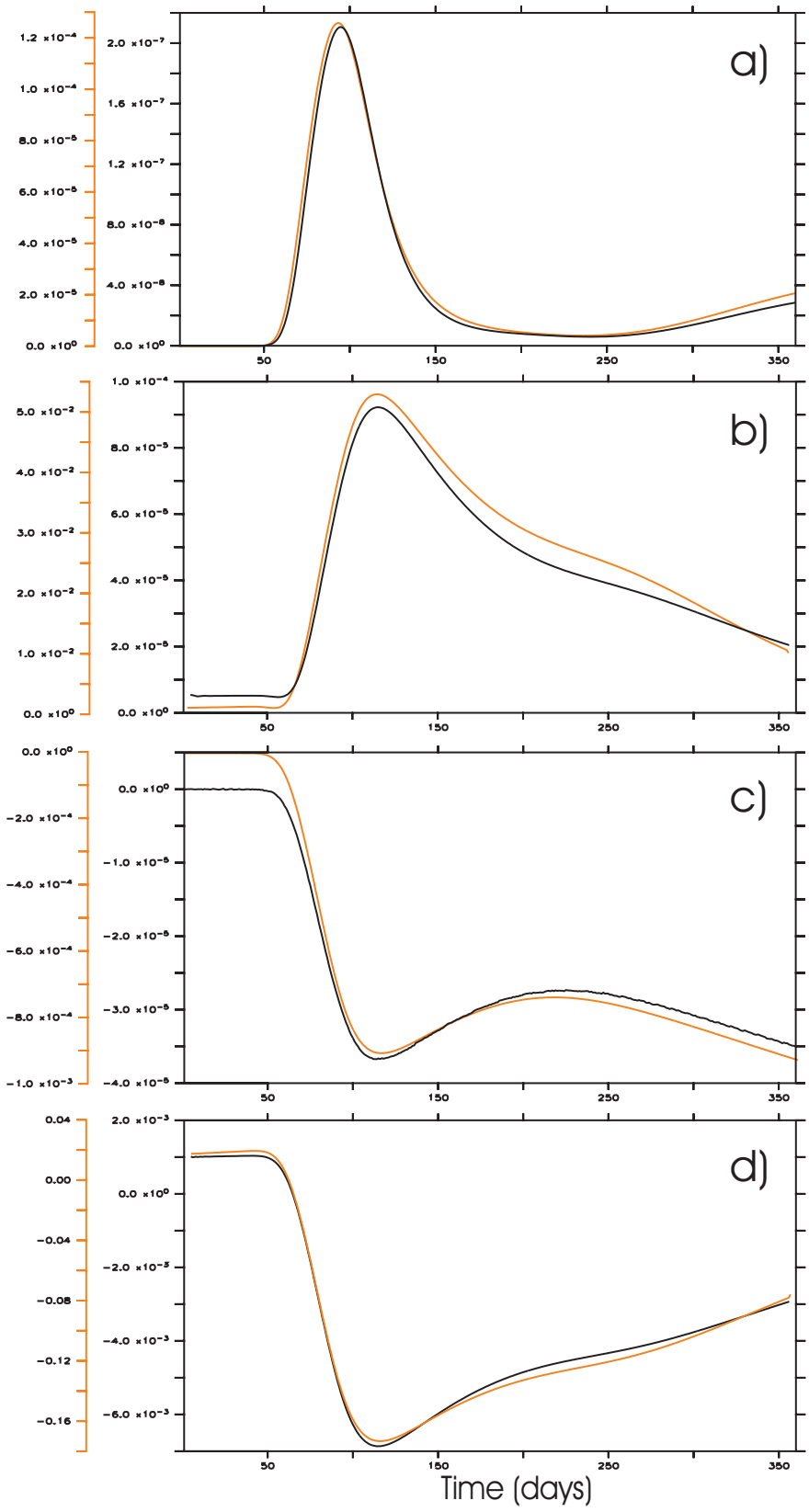

Fig. 6.5: a) Baroclinic kinetic energy anomaly (kg m^{-1} s^{-2}), b) Barotropic kinetic energy anomaly (kg m^{-1} s^{-2}), c) Potential energy anomaly (kg m^{-1} s^{-2}), and d) JEBAR (kg m^{-1} s^{-3}) averaged along the equator for forcing (i) (black), and forcing (ii) (red) anomalies located at 40°N.

6.2.2 Determining the role of the barotropic mode

The temperature anomaly is introduced at a second location further North (66°N – 70°N, 0°E – 4°E). The spatial displacement of the two locations will determine the mode (barotropic or baroclinic) by which the energy propagates to the equator. If the baroclinic signal along the equator is forced by barotropic wave propagation through the equatorial waveguide, as suggested by *Reznik and Zeitlin* (2006), a lag of order a few days at most would be expected from shifting the location of the anomaly poleward by 26°. However, if the energy transfer is predominantly baroclinic, a lag corresponding to the time taken for the baroclinic Kelvin wave to propagate from 66°N to 40°N, 35 days for a wave propagating at 1 ms^{-1}, should be seen.

The equatorial response of the two integrations is broadly similar in structure. The amplitude of the 66°N curves is considerably smaller due to the additional energy attenuation over the greater distance. The peak in baroclinic kinetic energy arrives 100 days into the integration for the 40°N location (Figure 6.6 a) (black)). The equivalent peak for the 66°N location arrives after 200 days of integration (Figure 6.6 a) (red)). The lag of 100 days between the two responses strongly indicates that the peak in baroclinic kinetic energy within the equatorial waveguide results from equatorward propagating baroclinic Kelvin waves along the western boundary. It does not suggest that the peak in baroclinic kinetic energy along the equator arises from energy exchange from the barotropic waves which are seen to propagate across the equatorial waveguide.

The peak in the baroclinic energy propagates equatorward along the western boundary from the source region at a speed of 0.65 $m\,s^{-1}$. Propagation of the Kelvin wave along the equator is at a similar speed. As shown previously, the discrepancy between the speed of the propagating signal observed here and theory is due largely to model resolution and viscosity.

In a further experiment the 66°N integration is repeated in the same basin, but this time with the model integrated to equilibrium with surface boundary conditions applied (Figure 6.7 (red)). The results from the static basin with the anomaly at 66°N are repeated for comparison (Figure 6.7 (black)). Again the response is broadly similar in structure. The presence of a background mean flow, which is predominantly directed northward along the western boundary, causes a further lag in the arrival of the peak in baroclinic kinetic energy at the equator of around 50 days. All other energy variables show a similar lag. Interestingly, the presence of background flow and restoring boundary conditions appears to have strengthened the signal reaching the equator. The model basin which has been integrated to equilibrium is able to maintain a strong thermocline, along which the baroclinic Kelvin wave propagates. The static basin model gradually

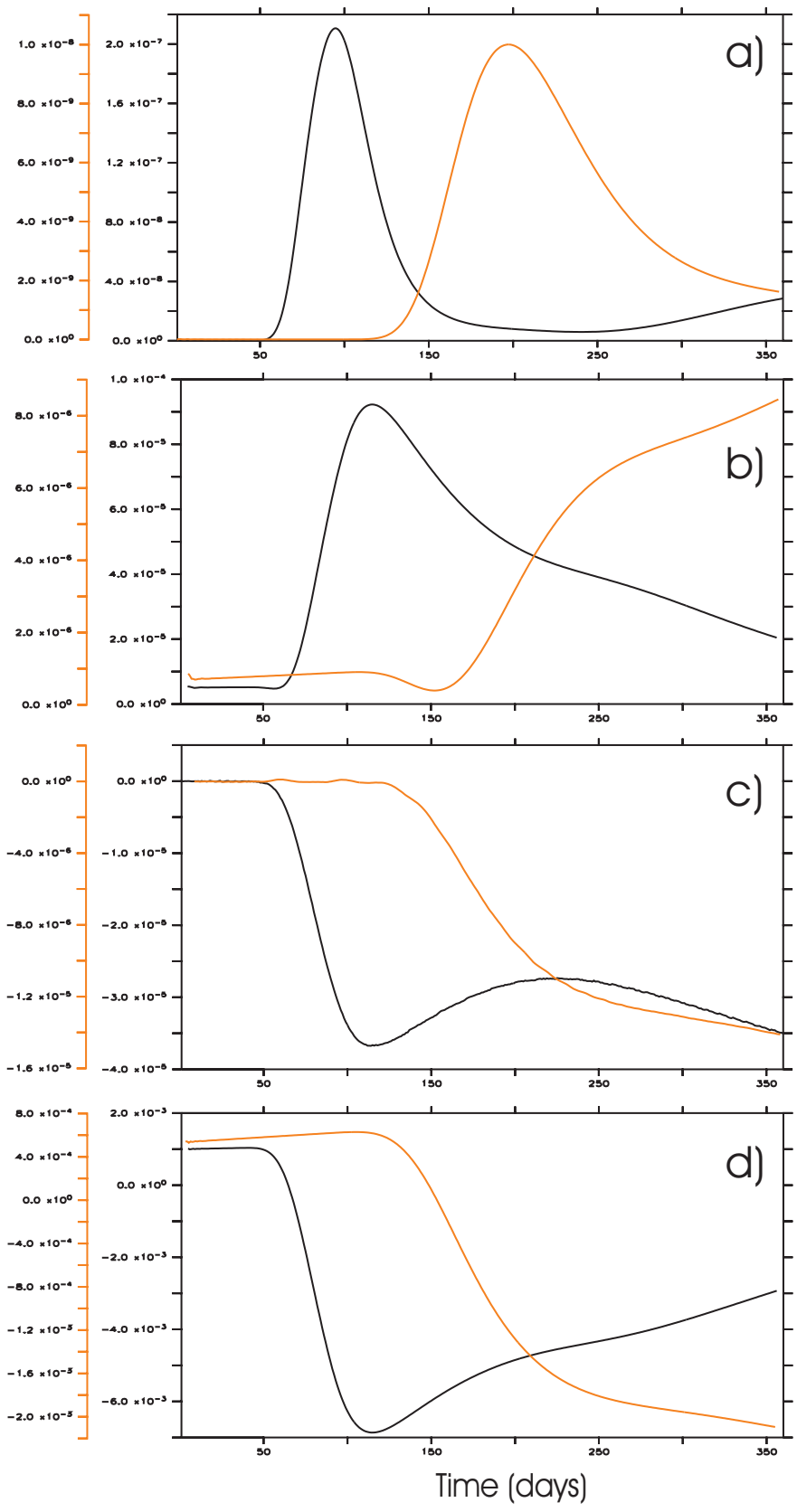

Fig. 6.6: a) Baroclinic kinetic energy anomaly (kg m^{-1} s^{-2}), b) Barotropic kinetic energy anomaly (kg m^{-1} s^{-2}), c) Potential energy anomaly (kg m^{-1} s^{-2}), and d) JEBAR (kg m^{-1} s^{-3}) averaged along the equator for the forcing (i) anomaly located at 40°N (black) and 66°N (red).

relaxes towards a uniform temperature in the vertical over time, which results in a weaker thermocline which is less ideal for wave propagation.

6.2.3 Energy at the equator

The baroclinic kinetic energy in the equatorial waveguide can be seen to grow exponentially, before tailing off again. A second, less prominent peak of baroclinic energy can be seen after the initial peak in the eastern side of the basin (Figure 6.8). The second peak is the returning equatorially trapped Rossby wave signal, which has been reflected from the eastern boundary. The initial peak represents the eastward propagating equatorial Kelvin wave and can be seen to arrive at 30°E before 40°E. The second peak originates from the eastern boundary and can be seen to arrive at 40°E before 30°E. A more gradual growth of baroclinic energy starts to form around 250 days into the integration (not shown).

To the eastern side of the basin off-equatorial Rossby waves are visible in the baroclinic energy field, propagating westward from the eastern boundary (Figure 6.9).

The maximum value of baroclinic kinetic energy along the equator varies with longitude (Figure 6.10). There is a strong peak on the western boundary, which is caused by the equatorward propagation of the baroclinic Kelvin wave along the coast. There is significant energy loss as the transition between coastally trapped Kelvin wave and equatorially trapped Kelvin wave occurs. The peak value of baroclinic energy in the equatorial Kelvin wave is approximately one third of the peak baroclinic energy which arrives at the equator in the coastally trapped Kelvin wave. A substantial amount of the energy is lost, either to boundary currents or to a diffusive Poincare wave field, because of the abrupt change in the direction of propagation where the equator and coastline meet (*LeBlond and Mysak*, 1978). In the idealised basin the equator and coast intersect at right angles. This is almost true for most points where the equator crosses land masses in the globe. Energy loss will be reduced at locations where the coastline and equator intersect at greater angles, for example equatorward propagation of a Kelvin wave along the coast of South America in the Northern Hemisphere. Across the basin between 10°E and 45°E there is a uniform decrease in the maximum value. The peak value then drops more rapidly near the eastern boundary as energy is transferred to poleward propagating coastal Kelvin waves.

The time of the maximum baroclinic kinetic energy along the equator is also interesting. The signal clearly arrives first at 4°E (Figure 6.11). On the coast the peak in energy lags behind the peak at 4°E by two days. This lag arises due to the implementation of no-slip boundaries in the MOMA model, which retards

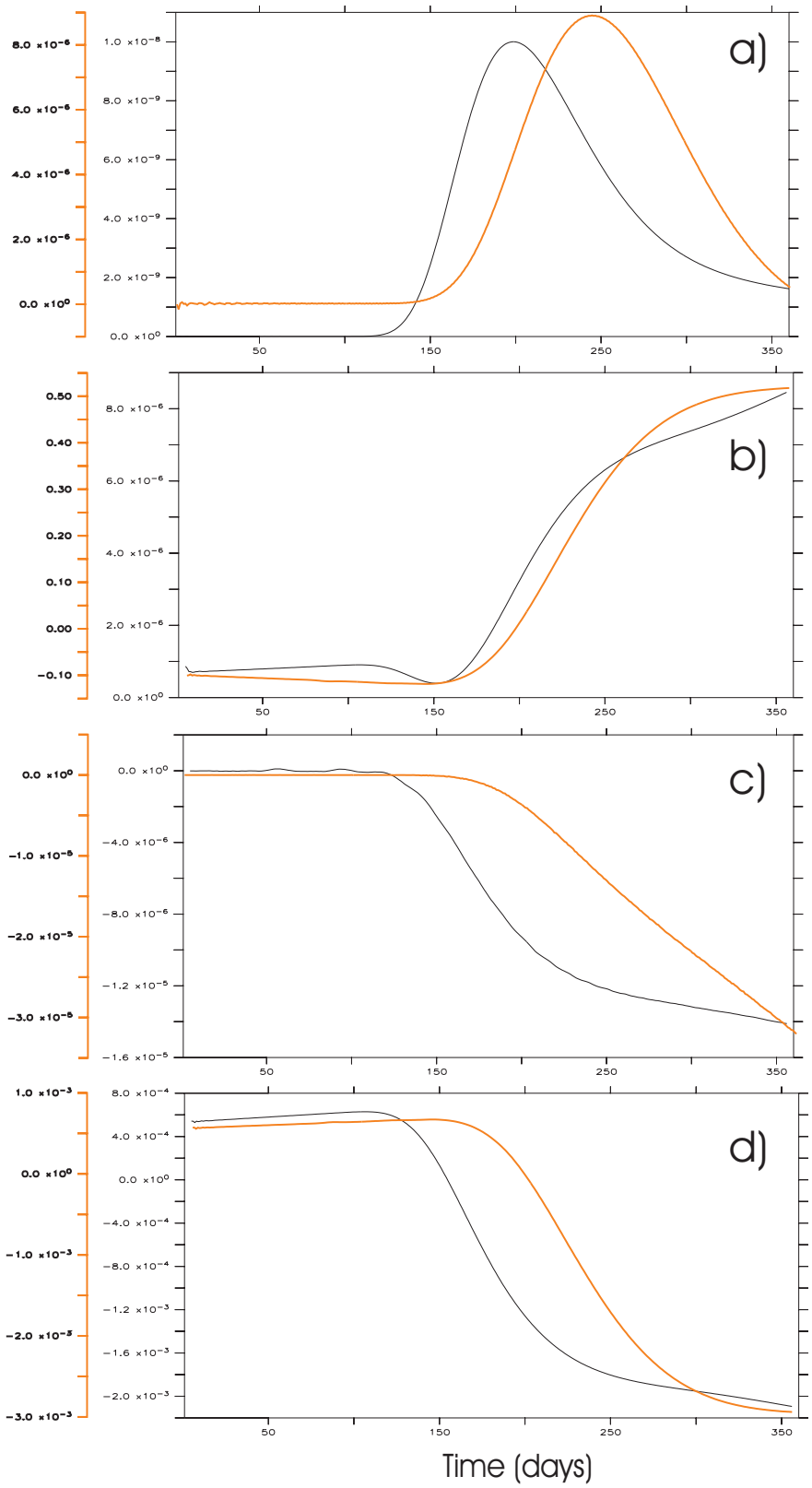

Fig. 6.7: a) Baroclinic kinetic energy anomaly (kg m^{-1} s^{-2}), b) Barotropic kinetic energy anomaly (kg m^{-1} s^{-2}), c) Potential energy anomaly (kg m^{-1} s^{-2}), and d) JEBAR (kg m^{-1} s^{-3}) averaged along the equator for the forcing (i) anomaly located at 66°N in the static basin (black), and in the spun up basin (red).

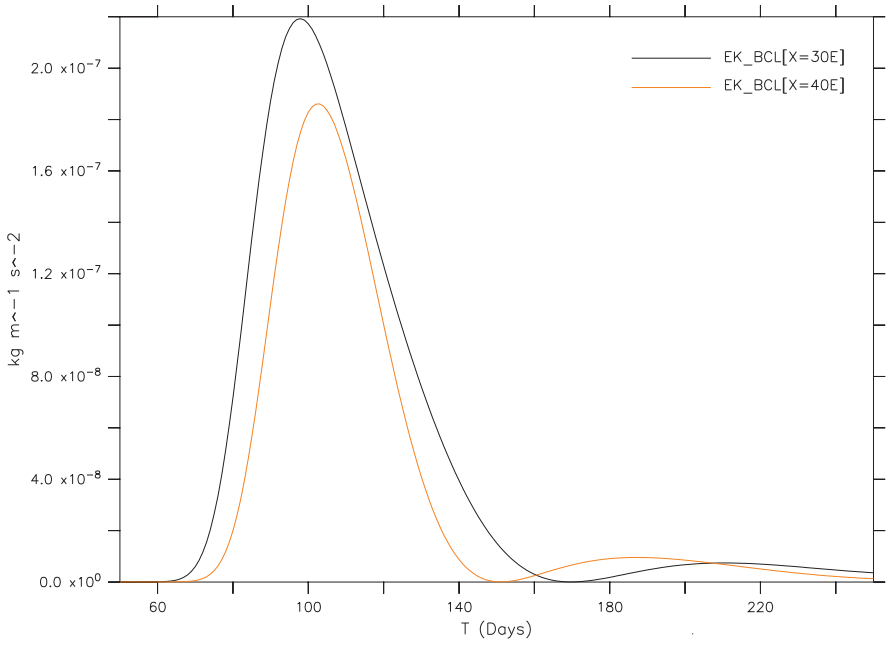

Fig. 6.8: Baroclinic kinetic energy against time at 30°E (black) and 40°E (red) on the equator for forcing (i) located at 40°N.

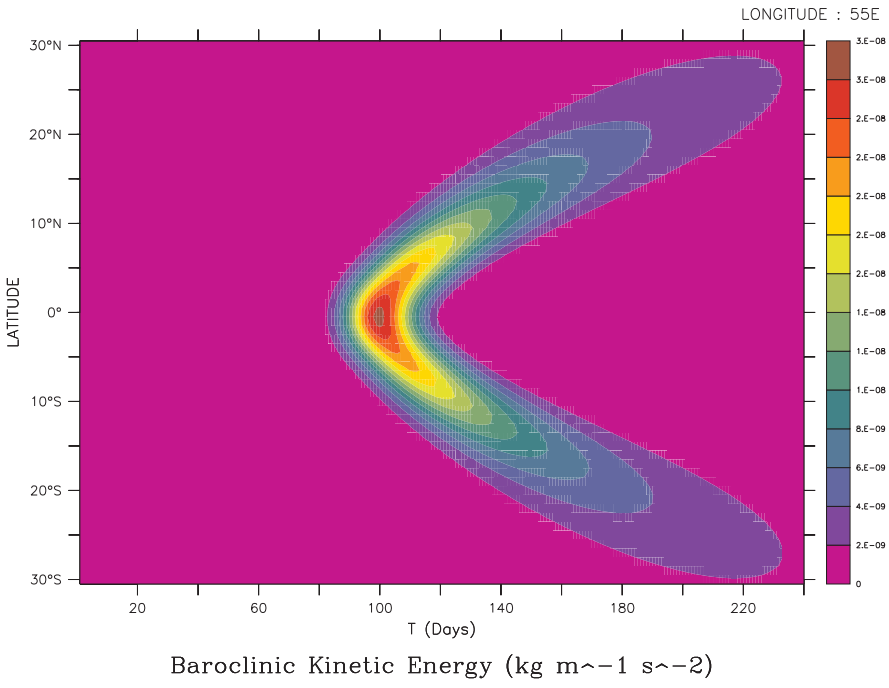

Fig. 6.9: Baroclinic kinetic energy anomaly (P-C) over time ($\mathrm{kg\,m^{-1}\,s^{-2}}$) at 55°E in the tropical region of the idealised MOMA basin after the introduction of forcing (i) at mid-latitudes. Rossby wave propagation is clearly shown.

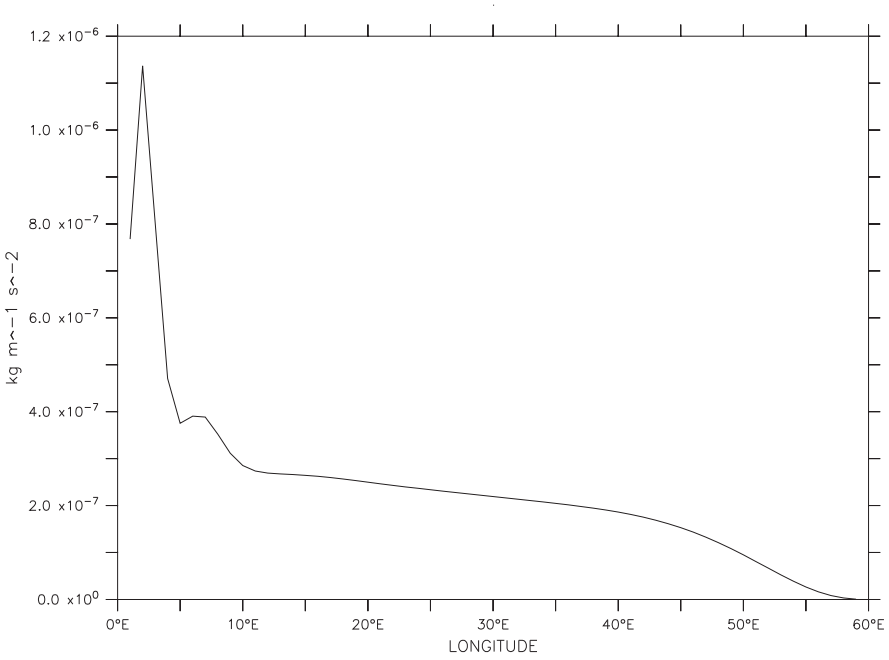

Fig. 6.10: Maximum baroclinic kinetic energy anomaly (P-C) along the equator in the idealised MOMA basin after the introduction of forcing (i). Units are $\mathrm{kg\,m^{-1}\,s^{-2}}$.

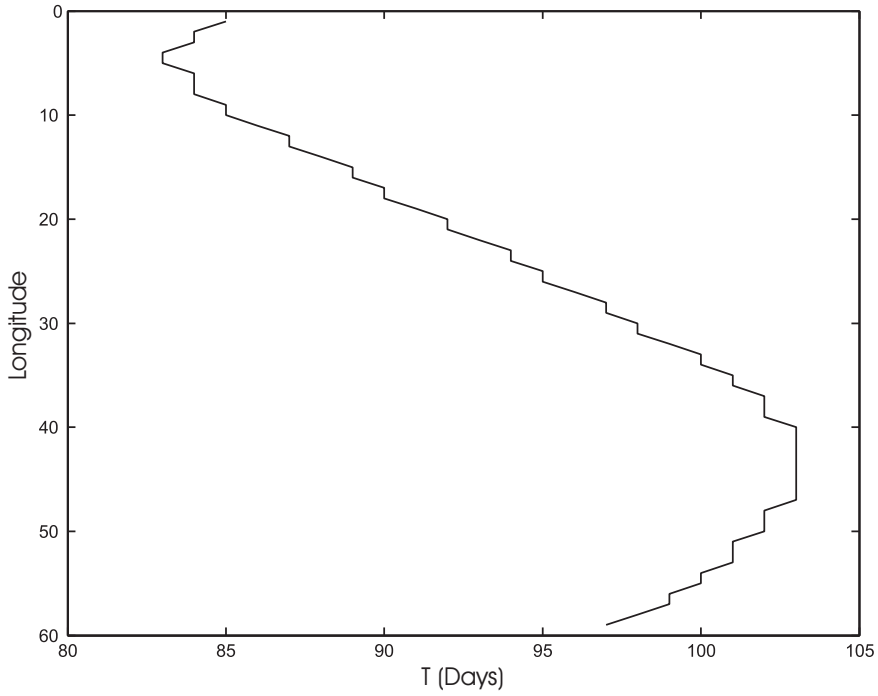

Fig. 6.11: Time of maximum baroclinic kinetic energy anomaly (P-C) along the equator in the idealised MOMA basin after the introduction of forcing (i).

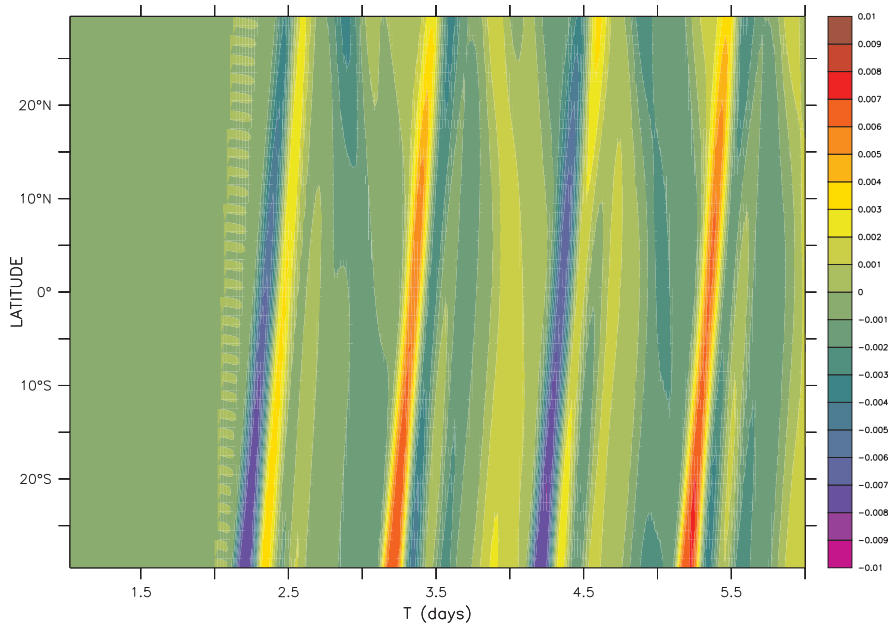

Fig. 6.12: Barotropic Kelvin wave propagation seen in FSH (m), crossing the equator from the forcing (i) anomaly located near the Drake Passage on the Antarctic coast (60°S, 56°E) in the idealised static MOMA basin.

the equatorward propagation of energy on the boundary. Between 4°E and 40°E the trend is linear, as would be expected by eastward propagating equatorially trapped Kelvin waves. From 48°E to the eastern boundary the peak in baroclinic kinetic energy arrives progressively earlier, suggesting propagation from east to west. This feature arises due to positive interference of the eastward propagating Kelvin wave and the westward propagating Rossby wave, which is reflected from the eastern boundary. The Kelvin wave propagates at $c = \sqrt{g'H}$, whilst the 1st baroclinic Rossby wave propagates at approximately $c = \frac{1}{3}\sqrt{g'H}$. The location of the peak in baroclinic energy on the equator, 3/4 of the way across the basin, is consistent with these wave speeds.

6.2.4 Equatorial energy response in the absence of a direct coastal path

The previous experiments show that, where an anomaly is located against a boundary, the mechanism which causes growth of baroclinic energy along the equator is baroclinic coastal Kelvin wave propagation along the western boundary.

One further experiment to try and identify the existence of a *Reznik and Zeitlin* (2006) type energy exchange locates the anomaly on the Antarctic coast, near the Drake Passage (60°S, 56°E). This location disconnects the source of the anomaly from the equator. There is no direct coastal pathway along which baroclinic

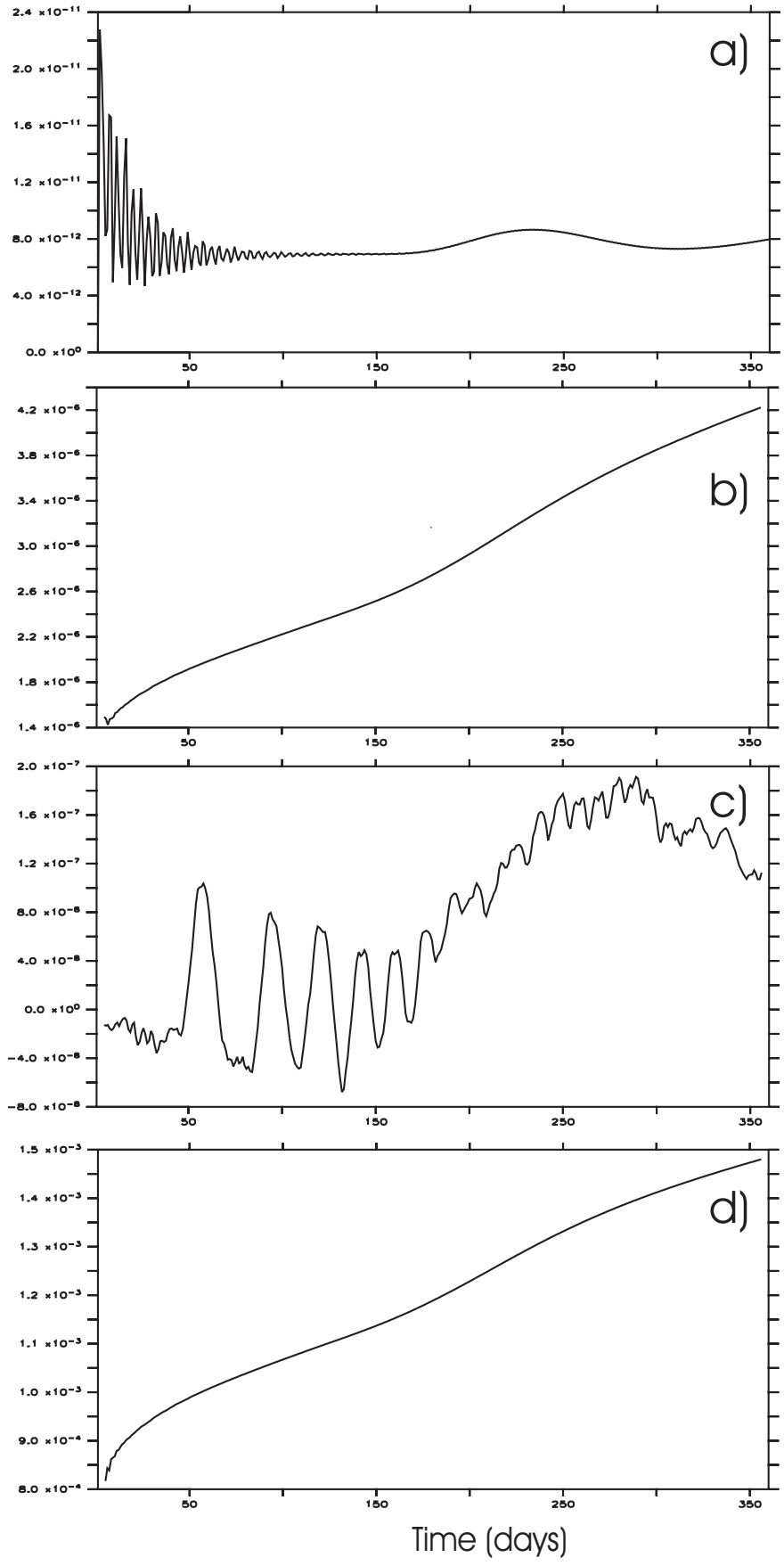

Fig. 6.13: a) Baroclinic kinetic energy anomaly (kg m^{-1} s^{-2}), b) Barotropic kinetic energy anomaly (kg m^{-1} s^{-2}), c) Potential energy anomaly (kg m^{-1} s^{-2}), and d) JEBAR (kg m^{-1} s^{-3}) averaged along the equator for the forcing (i) anomaly located near the Drake Passage on the Antarctic coast (60°S, 56°E).

Kelvin waves are able to propagate in order to reach the equator. Barotropic waves still propagate across the equatorial waveguide as shown before from the northern hemisphere locations (Figures 6.3, 6.4), but this time from south to north (Figure 6.12).

The response at the equator is notably different to the previous integrations. Amplitudes of all the energy values are greatly reduced (Figure 6.13). The baroclinic kinetic energy is initially strongly influenced by the barotropic wave propagation across the equatorial waveguide. The baroclinic energy does not show an exponential growth as one might expect to see based on the results of *Reznik and Zeitlin* (2006). The barotropic kinetic energy and the potential energy anomaly at the equator show similar responses. The previous experiments all show the barotropic kinetic energy and the potential energy anomaly to behave oppositely. The JEBAR response is markedly different to the previous experiments also. In the first 150 days it shows a quite distinct period, initially of 30 days, but decreasing with time to around 20 days. Similar periodicity appears in the vertical velocity seen along the equator in the FORTE model output in Chapter 5.

6.3 The influence of bottom topography on signal propagation

In chapter 5, results from FORTE suggest that topography plays an important role in the transmission of a signal away from a Southern Ocean anomaly. Sections taken from the results of the FORTE model across some of the major topographic ridge features which extend equatorward from the coast of Antarctica show a temperature signal, often with opposite signs either side of the topographic ridge (Figure 6.14). The anomaly in the FORTE model (chapter 5) is located over the southern extent of the Mid-Atlantic Ridge. Anomalies of similar magnitude propagate along either side of the ridge (Figure 6.14 a)). Further west, similar ridges show a slightly different response. For both the East Pacific Rise and the ridge on which the Kerguelen Archipelago lies, the anomaly which propagates along the eastern side of the ridge is considerably stronger than that which propagates along the western side (Figures 6.14 b), 6.14 c)).

The anomaly which propagates along the Mid-Atlantic Ridge extends equatorward to 30°S. Beyond this it is not easy to identify the signal. Propagation of Kelvin waves equatorward along the coast of South America and SST responses to atmospheric signals mask the signal propagating along the ridge. It is important to find out whether the signal which propagates along these topographic ridges is able to reach and influence the equator. In particular, the East Pacific

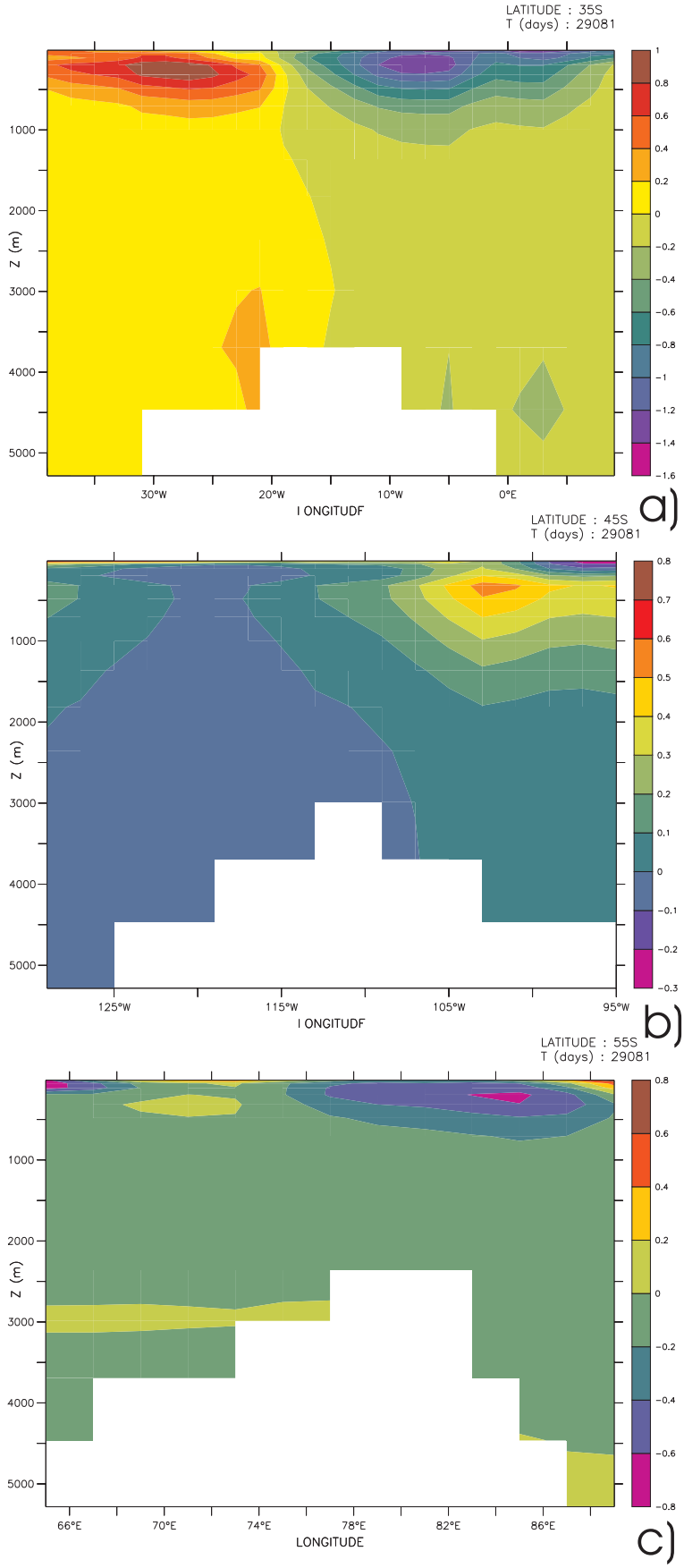

Fig. 6.14: Cross-section of the asymmetric temperature anomaly (°C) signals which form along a) the Mid-Atlantic Ridge, b) the East Pacific Rise, and c) near the Kerguelen Archipelago, 180 days after the introduction of the salt anomaly to the FORTE model (described in chapter 5). The anomalies are calculated from the ensemble mean (P-C).

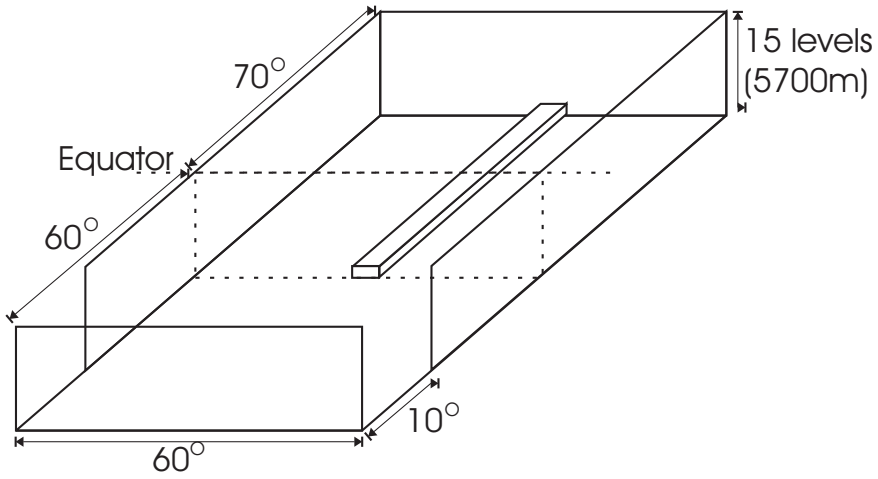

Fig. 6.15: Schematic showing the dimension of the idealised MOMA basin including the Mid-Atlantic Ridge.

Rise provides a possible route for a signal to very rapidly reach the eastern equatorial Pacific.

The static idealised basin setup provides an ideal tool to examine how topography influences wave propagation. The idealised basin is modified to include a single ridge 500 m (1 level) in height extending south from the northern boundary to the equator (Figure 6.15). A series of 360 day integrations are completed using the static idealised basin model. The first two experiments show the response of different anomalies placed directly over the ridge, adjacent to the northern boundary. These experiments simulate the response of the Mid-Atlantic Ridge in the FORTE model. In the third experiment the location of the anomaly is moved eastward away from the ridge, but remains adjacent to the northern boundary, simulating more closely the situation in which energy is seen to propagate along the East Pacific Rise in the FORTE model. A fourth experiment detaches the anomaly from the northern boundary, eliminating the direct path along which Kelvin waves are able to propagate. This experiment shows how the barotropic Rossby wave propagation across the East Pacific Rise, seen in the FORTE model, may interact with the topography.

6.3.1 Experiment (i)

The full-sin anomaly, used in the idealised basin without the ridge in chapter 4 (Figure 4.3 c)), is placed directly over the ridge and adjacent to the northern boundary. This anomaly is introduced to the initial field of the model. It is not sustained over time. The model is integrated for 360 days.

A feature forms along the ridge with temperature anomalies of opposite sign either side of the ridge (Figure 6.16). A positive anomaly extends equatorward

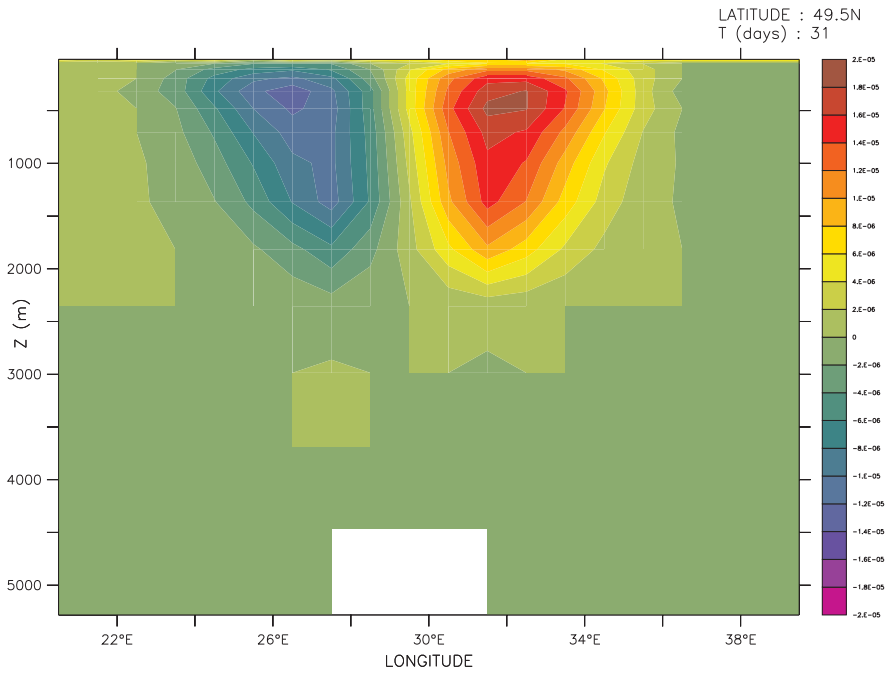

Fig. 6.16: Experiment (i): Vertical slice through 50°N after 30 days intergation showing temperature anomalies above the ridge in the idealised MOMA basin.

along the eastern side of the ridge, whilst a corresponding negative anomaly extends along the western side. The temperature anomalies extend to 2000 m depth, with the maximum amplitude at 300 m (level 5).

The anomalies do not propagate in the same way that the coastal Kelvin wave response does. The temperature anomaly grows stronger and extends further south over time (Figure 6.17 a)).

Initial growth of the anomaly is rapid (Figure 6.17 b)), and after 30 days very weak temperature anomalies, not visible on this scale, are visible as far south as 10°N. After 50 days the anomaly reaches it southern most extent and is sustained for the remainder of the 360 integration. The signal which extends down as far as 10°N is weak, and does not continue to grow in strength. The Kelvin wave response which propagates around the coastline and along the equator is far stronger. This response appears after 225 days and increases in amplitude for the remainder of the integration (Figure 6.17 b)).

Gill et al. (1986) conducted a series of numerical and laboratory experiments examining the Rossby adjustment over a step. They describe the along step propagation as a double Kelvin wave, which always propagates with the shallow step to the right. The propagation speed of the wave is given as the difference between the gravity wave speed for the shallow (on ridge) and deep (off ridge) water depths, $c = (\sqrt{gH_{deep}} - \sqrt{gH_{shallow}})$, making it considerably slower than a coastal Kelvin wave. For the idealised basin used here, propagation speed for a barotropic double Kelvin wave is 18.4 ms^{-1}.

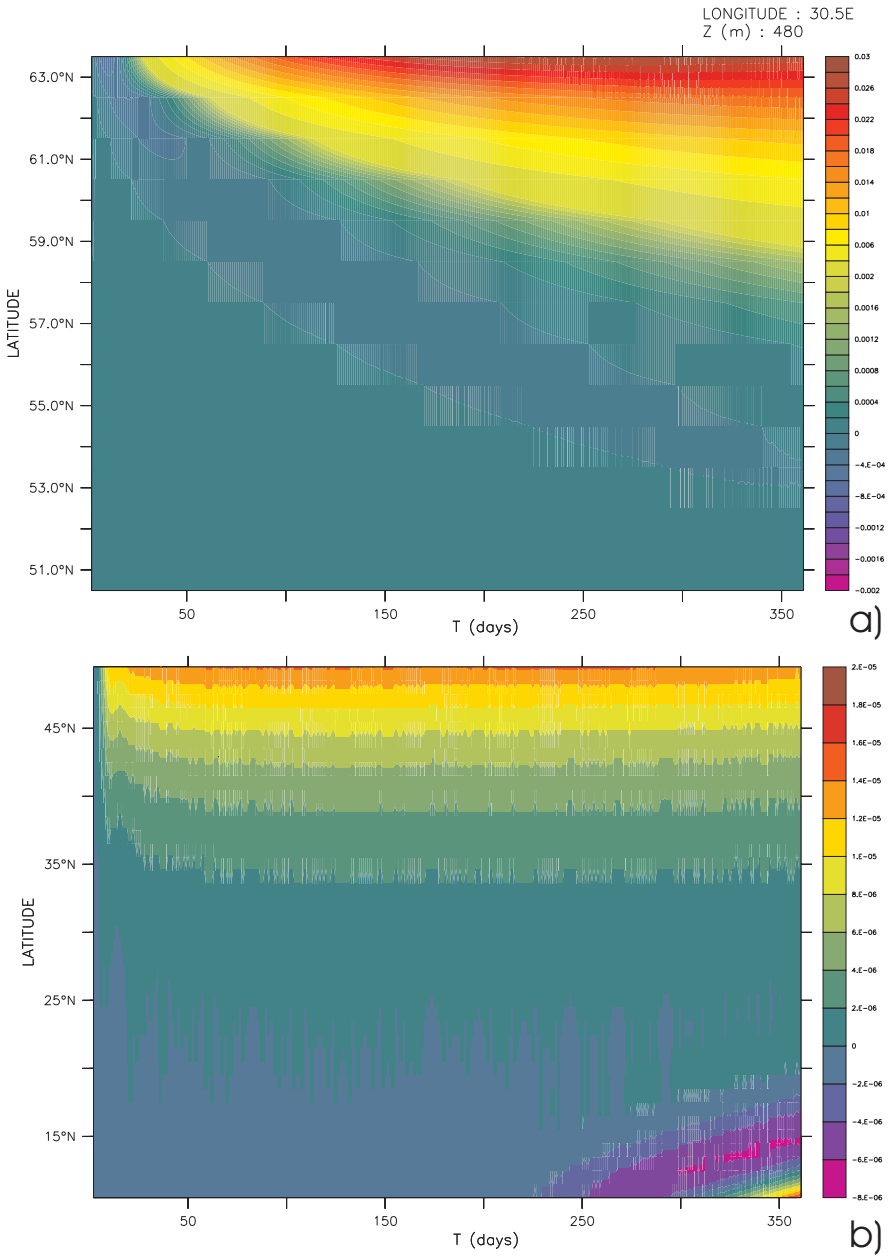

Fig. 6.17: Experiment (i): Hovmöller diagram at 30°, 480 m depth, along the eastern side of the ridge showing growth of temperature anomaly with time. a) 50°N to 65°N, and b) 10°N to 50°N are separated and use different scales for clarity.

The anomaly which extends along the Mid-Atlantic Ridge in FORTE show the same sign orientation of the anomaly either side of a ridge. A positive (negative) anomaly corresponds to downwelling (upwelling) of the thermocline along the ridge.

The overall response to the anomaly is very similar to that of the experiment without the ridge (compare Figures 6.18 c), 4.7). The effect of the signal which develops along the ridge is small compared to the Kelvin wave response which propagates around the boundary. The temperature anomaly which develops along the ridge weakens as it extends south, and is too weak to have any

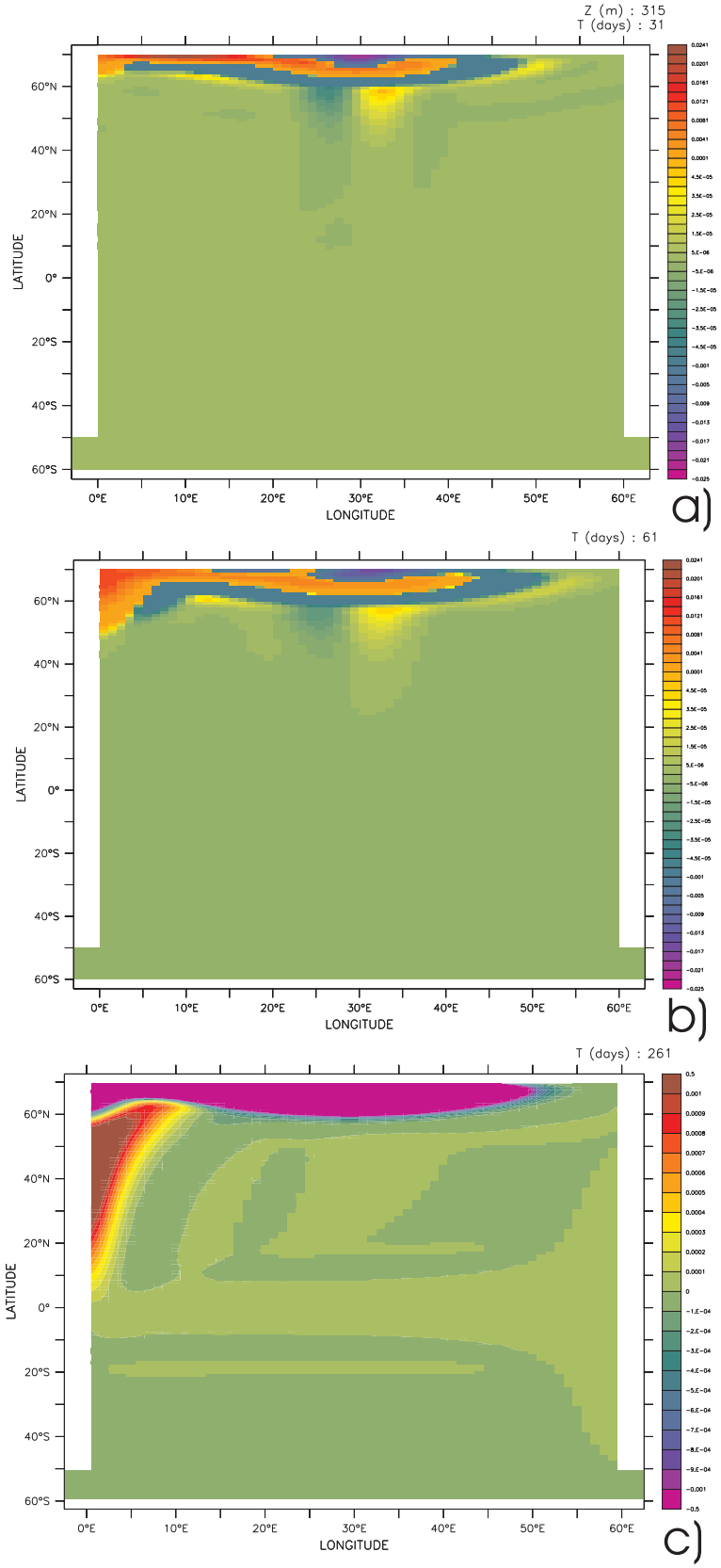

Fig. 6.18: Experiment (i): Temperature anomalies (°C) at level 5 after a) 30 days, b) 60 days, and c) 260 days integration in the idealised MOMA basin with a Mid-Atlantic Ridge.

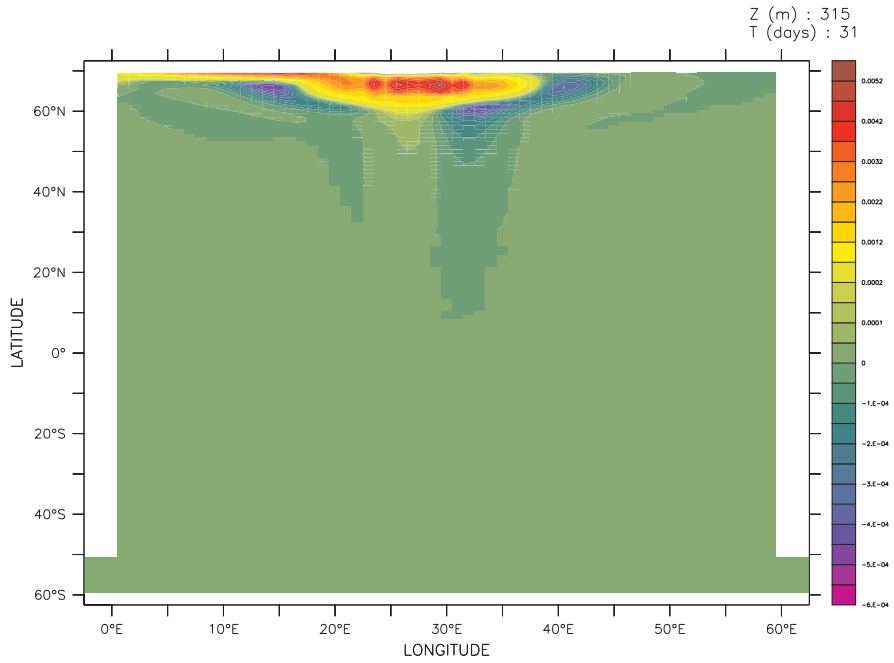

Fig. 6.19: Experiment (ii): Temperature anomalies (°C) at level 5 after 30 days integration in the idealised MOMA basin with a Mid-Atlantic Ridge.

significant influence on the equator. The Kelvin wave response at the equator is far stronger, and dominates the overall response of the basin to the anomaly (Figure 6.18 c)).

6.3.2 Experiment (ii)

For experiment (ii) the location of the anomaly remains the same, but this time forcing (i), described in section 6.2, is used (Figure 6.1). The anomaly used in experiment (i) is an initial disturbance, and does not provide a train of barotropic waves. The anomaly used for this experiment is time varying, producing barotropic waves daily throughout the integration.

Perhaps surprisingly, a response very similar to experiment (i) appears. The spatial distribution of the response to the anomaly is similar (Figure 6.19). In this case the signs of the anomalies have reversed, compared to experiment (i) (Figure 6.20).

The anomaly along the ridge extends further south than in experiment (i) (40°N compared to 53°N, Figure 6.21). Again, no effects of the anomaly are seen to influence the equator. There is little difference between the response from experiment (i) and the response from experiment (ii).

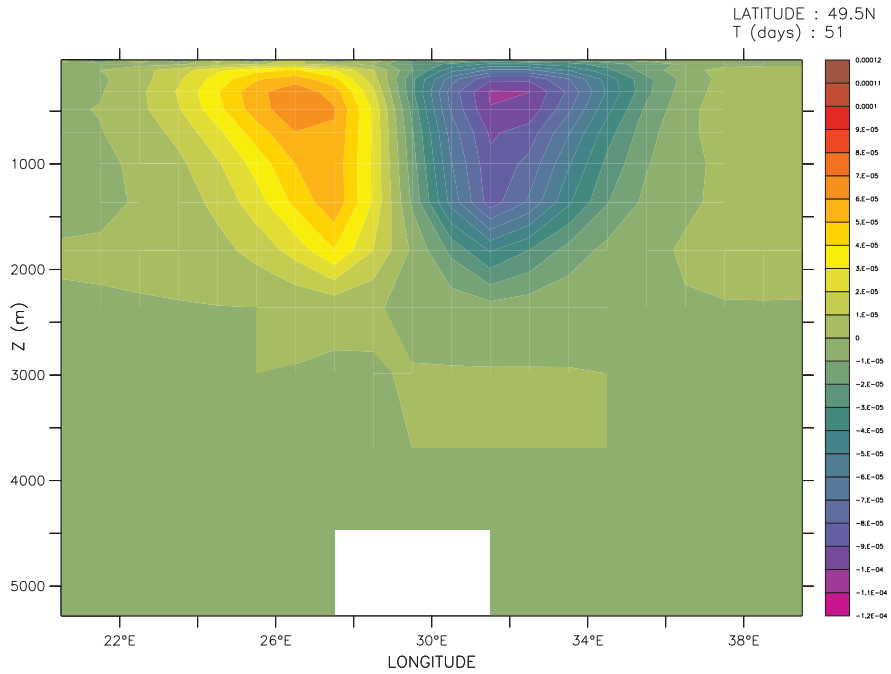

Fig. 6.20: Experiment (ii): Vertical slice through 50°N after 50 days integration showing temperature anomalies (°C) above the ridge in the idealised MOMA basin

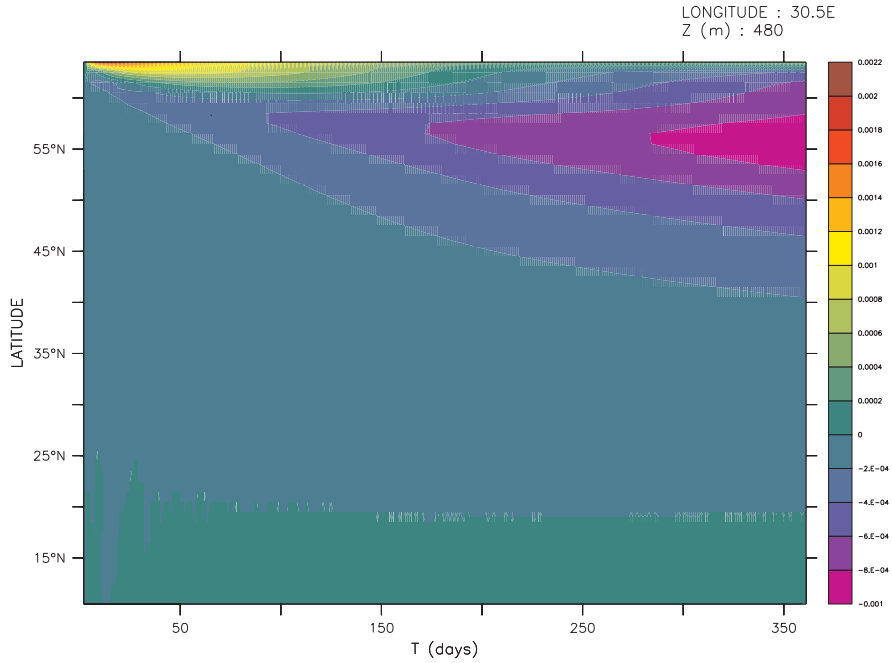

Fig. 6.21: Experiment (ii): Hovmöller diagram showing temperature anomalies (°C) at 480 m along the eastern side of the ridge in the idealised MOMA basin.

6.3.3 Experiment (iii)

For experiment (iii) the same anomaly as experiment (ii) is used, but located to the east along the northern boundary (40°E – 45°E). This location means that the anomaly is not directly forcing the water column above the ridge. Instead, the water column is forced by the coastal Kelvin wave which propagates westward along the northern boundary.

In the vertical profile taken across the ridge, a pattern similar to the ones seen when the anomaly is located directly over the ridge (experiments (i) and (ii)) can be seen (Figure 6.22). In this case the responses on either side of the ridge are asymmetric in both sign and shape. The response on the eastern side of the ridge is similar in width and depth to the anomalies seen in experiments (i) and (ii). The response on the western side of the ridge is considerably smaller. In experiments (i) and (ii), where the anomaly is located directly over the ridge, both the east and west responses were the same amplitude. In this case the response along the western side of the ridge is weaker. This asymmetry arises due to the propagating Kelvin wave reaching the eastern side of the ridge first and dissipating energy along the ridge. This weakens the Kelvin wave before it reaches the western side of the ridge, and there is less energy to dissipate along the far side of the ridge.

The spatial pattern of the response shows the evolution of the Kelvin and Rossby wave response along the coast and equator (Figure 6.23). Propagation along the ridge, with positive anomalies on the east and negative anomalies on the west can also be seen. These results show that direct forcing of the water column above the ridge is not necessary to trigger propagation along the ridge. The coastal Kelvin wave which propagates along the northern boundary is able to excite a similar response in the baroclinic structure along the ridge.

6.3.4 Experiment (iv)

In a fourth experiment the anomaly is moved south from its location in experiment (iii) (40°E – 45°E, 45°N – 50°N), detaching it from the northern boundary. The detachment of the anomaly from the northern boundary prevents the propagation of a coastal Kelvin wave, which normally dominates the model response, masking the much weaker response along the ridge.

After 30 days a temperature response along the ridge has appeared (Figure 6.26). It is weak in amplitude, but shows a similar structure to the response seen in experiment (iii). Over time the gyre circulation formed around the location of the anomaly by vortex stretching of the water column propagates west (compare figures 6.24, 6.25).

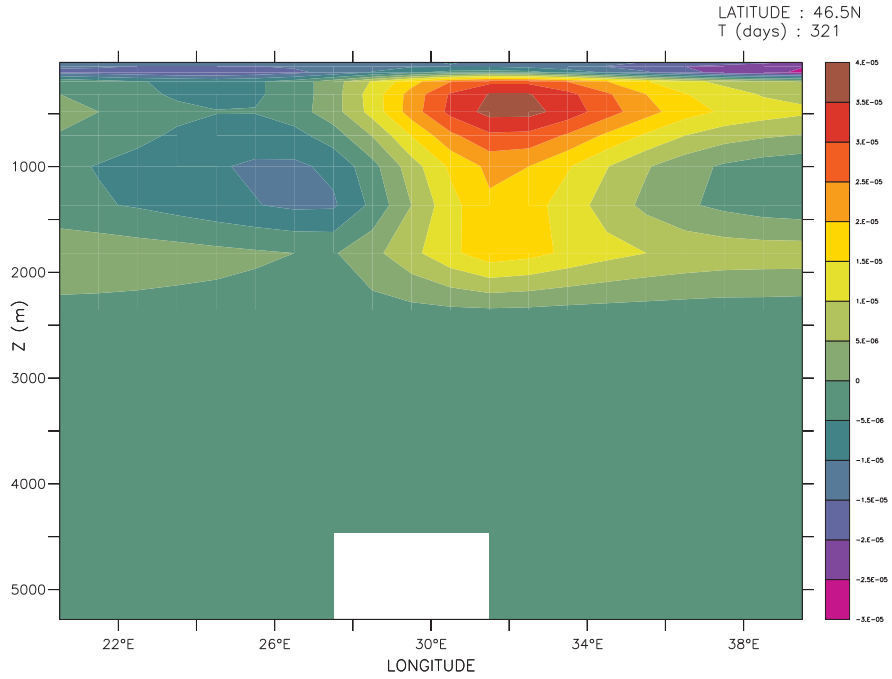

Fig. 6.22: Experiment (iii): Vertical slice through 47°N after 320 days integration showing temperature anomalies (°C) above the ridge in the idealised MOMA basin.

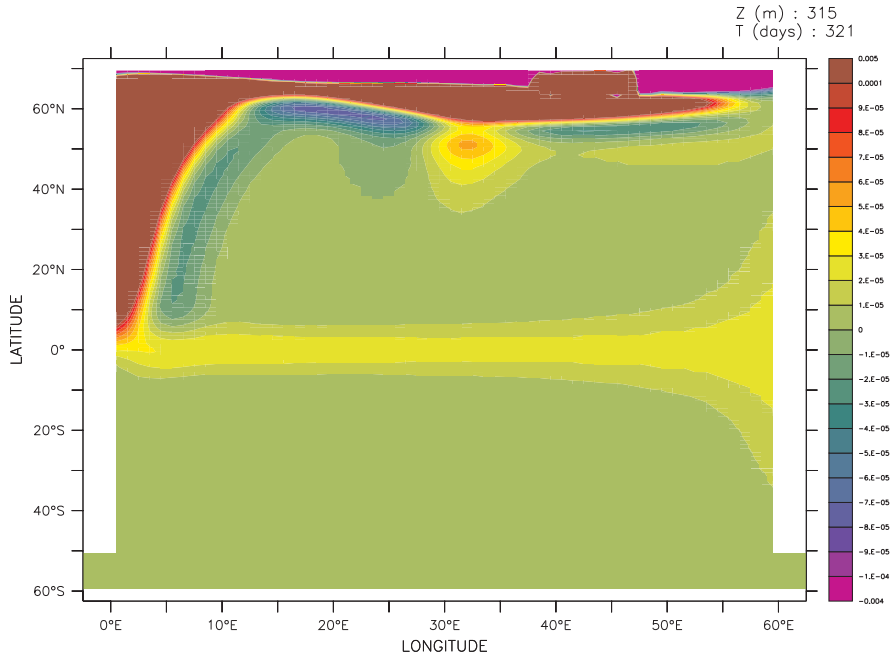

Fig. 6.23: Experiment (iii): Temperature anomalies (°C) at level 5 after 320 days integration in the idealised MOMA basin with a Mid-Atlantic Ridge.

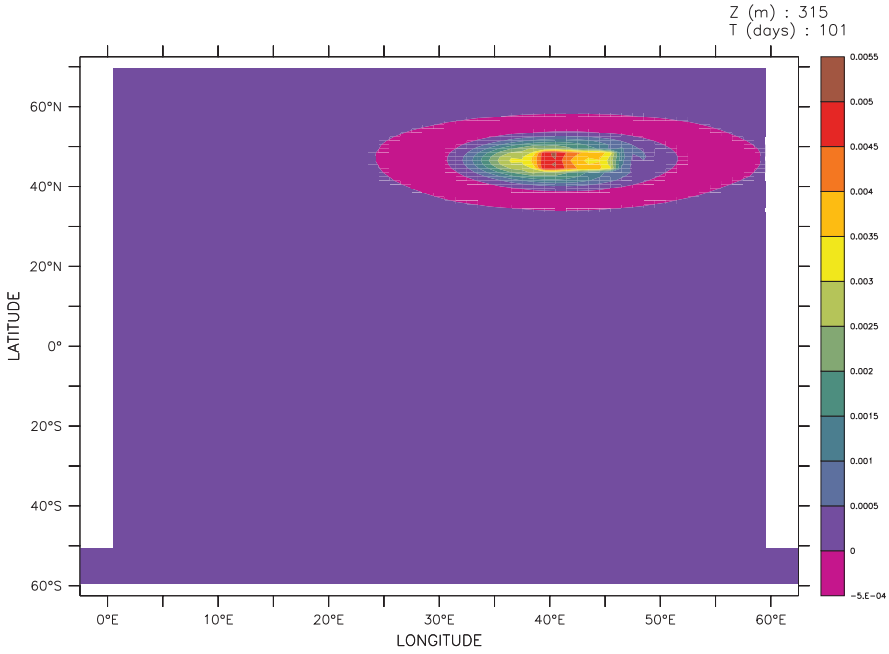

Fig. 6.24: Experiment (iv): Temperature anomalies (°C) at level 5 after 100 days integration in the idealised MOMA basin with a Mid-Atlantic Ridge.

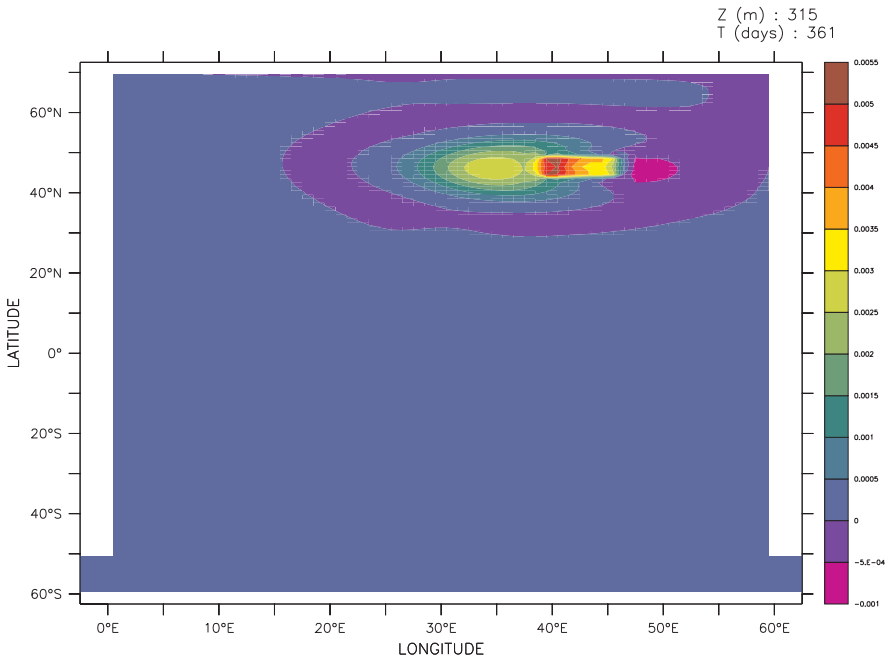

Fig. 6.25: Experiment (iv): Temperature anomalies (°C) at level 5 after 360 days integration in the idealised MOMA basin with a Mid-Atlantic Ridge.

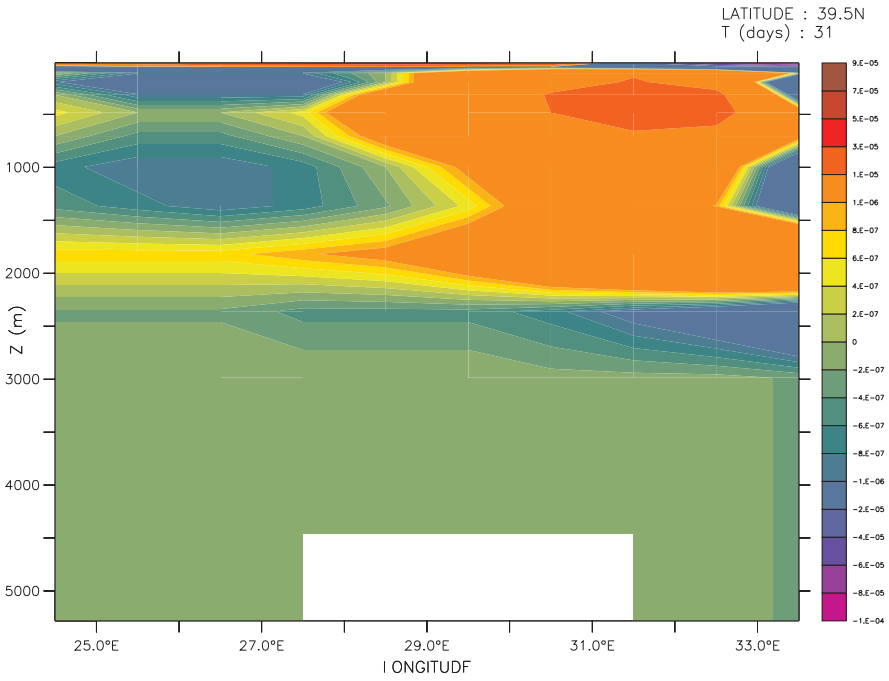

Fig. 6.26: Experiment (iv): Vertical slice through 40°N after 30 days integration showing temperature anomalies (°C) above the ridge in the idealised MOMA basin.

The spatial response of the model is very different to all of the previous experiments. The Kelvin and Rossby wave propagation which dominates the spatial response of the previous experiments is not present. Towards the end of the 360 day integration a pattern resembling the vertical cross-section taken from the previous experiment can be seen across the ridge (Figure 6.27, 6.28). The response along the eastern side of the ridge is separated vertically into two maxima, with the maximum of the negative response, which occurs along the western side of the ridge, located at mid-depth between them (Figure 6.27). The effect is even more pronounced in a section across the ridge at 62°N, to the north of the anomaly(Figure 6.28).

6.3.5 Discussion

These idealised model experiments show an interesting response arising from interaction of an anomaly with topography. In experiments (i) and (ii) the anomaly is placed directly over the ridge in the idealised basin. An anomaly, symmetric in shape with maxima at 500 m depth, but of opposite sign either side of the ridge, forms. The response is unlike a typical wave response, such as the coastal Kelvin wave which is seen to propagate around the basin. Instead the response grows in amplitude. It does not continue to propagate towards the equator, and the amplitude of the response south of 20°N is very small.

Experiment (iii) shows that a response along the ridge can also arise from Kelvin

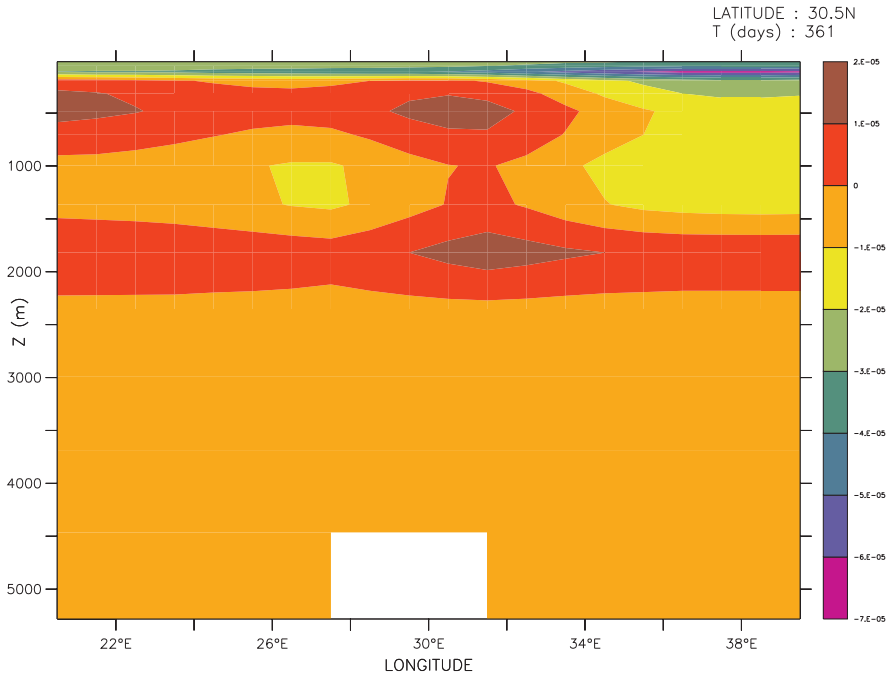

Fig. 6.27: Experiment (iv): Vertical slice through 30°N after 360 days integration showing temperature anomalies (°C) above the ridge in the idealised MOMA basin.

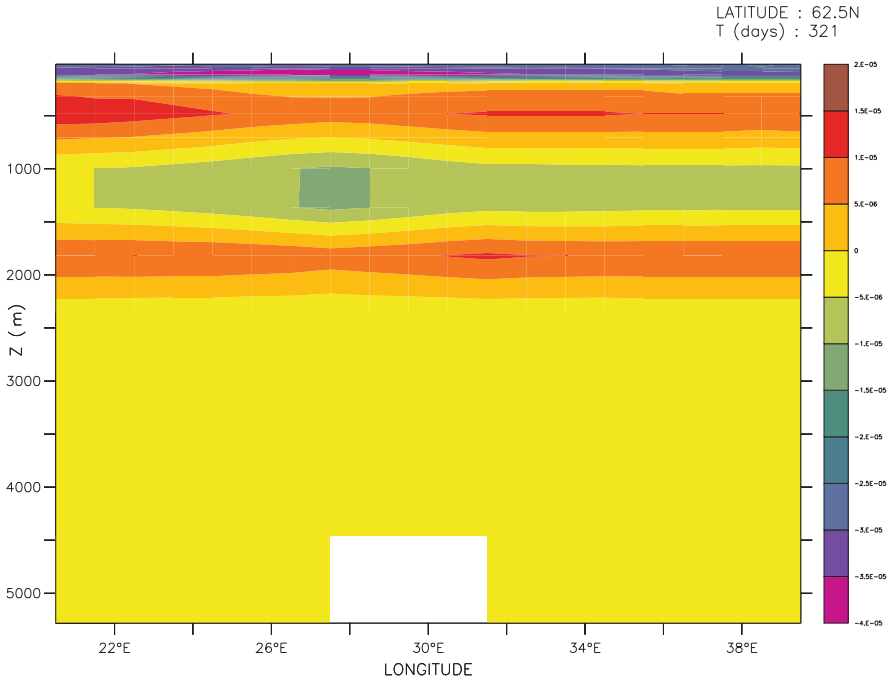

Fig. 6.28: Experiment (iv): Vertical slice through 62°N after 320 days integration showing temperature anomalies (°C) above the ridge in the idealised MOMA basin.

waves propagating along the coast and over the region where the ridge joins the northern boundary. The along ridge response is different to the cases where the anomaly is placed directly over the ridge (Figure 6.22). The response on the eastern side of the ridge, nearest the anomaly, is similar to the response on the eastern side of the ridge in experiments (i) and (ii), with a maximum signal at 500 m, extending down to 2000 m. The response on the western side of the ridge is much weaker, and the maximum amplitude is deeper at around 1200 m. This asymmetry arises from energy loss from the westward propagating coastal Kelvin wave as it crosses the ridge. More energy is available in the coastal Kelvin wave to propagate southward along the eastern side of the ridge than the western side of the ridge, since the western side of the ridge is reached by the Kelvin wave after it has crossed the eastern side. Similar effects are seen in chapter 5, where strong dissipation of energy from the barotropic Rossby waves occurs along the East Pacific Rise, effectively blocking most of the barotropic Rossby wave signal and preventing it from reaching the coast of Australia (Figure 6.14 b)).

In experiment (iv), the location of the forcing anomaly away from the northern boundary prevents the coastal Kelvin wave response, which is seen to dominate the overall model response in the previous three experiments, from propagating. The response along the ridge is weaker than in experiments (i)-(iii), but the vertical cross-section resembles the response seen in experiment (iii). Later in the integration the response is stronger, and it can be seen to develop into two distinct maxima along the eastern side of the ridge, with the single maximum on the western side of the ridge located at mid-depth between them (Figures 6.27, 6.28). The strongest signal appears late in the model integration, and is linked to the westward propagation of the gyre circulation caused by the anomaly across the ridge (Figures 6.24, 6.25).

Where the anomaly meets the ridge, the response extending south along the ridge is stronger than the response which extends north. The vertical section taken at 31°N shows a response that is more similar to experiment (iii). North of the anomaly, a similar pattern in the vertical slice can be identified, but it is weaker and is more dispersed horizontally.

All four experiments show similar responses along the ridge in the idealised model basin. The largest difference is the asymmetry between the two sides of the ridge which arises once the anomaly is moved east of the ridge. This is explained by the loss of energy from the coastal Kelvin wave as it crosses the eastern edge of the ridge first.

The results show that it is possible to excite a response along the ridge with coastal Kelvin wave propagation, as well as by directly forcing the water column above the ridge. Locating the forcing anomaly away from the coastline and ridge results in a much weaker response than the previous experiments, but a persistent

anomaly is able to produce a response which extends along the ridge.

6.4 Conclusion

The results from section 6.2 show that where a coastal pathway to the equator is provided, the energy at the equator arises from baroclinic Kelvin wave propagation. In the absence of a coastal pathway the equatorial energy response is very different. The amount of energy which reaches the equator is much smaller, and an exponential growth of energy, as suggested by *Reznik and Zeitlin* (2006) does not occur.

The model studies in section 6.3 show that it is possible for signals to be transmitted along topographic ridges. The responses seen do not propagate, but instead establish themselves and grow in amplitude. They can be strong over short distances, but weaken rapidly away from the source of energy. *Gill et al.* (1986) show that interaction of a signal propagating along a step in topography with a coast gives rise to a boundary current and coastal Kelvin wave propagation. The implications for this are that, in cases where topography exists between land masses, for example Antarctica and Australia, it is possible for signals to be transmitted along the topography to connected land masses. For example, a Kelvin wave response to a Southern Ocean anomaly, propagating around Antarctica, would be able transmit a signal across the Southern Ocean and form Kelvin waves along the coast of the Western Pacific. The results from the idealised model suggest that transmission of a signal directly to the equator only by means of topography is unlikely. However, it is possible for a signal to extend 30° away from a boundary with sufficient amplitude to trigger a Kelvin wave response along a connecting coastline.

The results of section 6.3 suggest that a different equatorial response would arise if the experiment from section 6.2.4 (anomaly in Drake Passage) were repeated with a topographic ridge introduced to the model between Antarctica and the western boundary. The topographic ridge would allow transfer of the signal from Antarctica to the western boundary.

Chapter 7

Discussion

The previous chapters examine the potential for high latitude anomalies to influence tropical climate via ocean wave mechanisms. The results of chapters 3 to 6 are summarised in sections 7.1 to 7.4. Section 7.5 discusses the relative roles of the ocean and atmosphere in global teleconnections. Section 7.6 outlines the implications of such rapid teleconnections on global climate. Section 7.7 discusses potential extensions of the work presented in this thesis for further study.

7.1 Dipole in HadCM3

EOF analysis of the COAPEC 100yr HadCM3 model run shows a clear cross-equatorial dipole structure with a decadal period in the first EOF.

Further analysis of the subsurface layers in the tropical Atlantic shows that baroclinic Kelvin and Rossby wave activity is present. Baroclinic Kelvin and Rossby waves are seen propagating along the equator. Westward propagating Rossby waves extend across the tropical Atlantic, and can be seen to drive anomalies towards the surface layers. Once into the surface layers the anomaly is rapidly mixed by the wind to produce a large scale coherent anomaly. The northern and southern lobes of the dipole can be seen to oscillate asymmetrically about the equator with a decadal period. These results suggest that Kelvin and Rossby waves in the tropical ocean can play a very important role in the evolution of climate phenomena such as the TAD.

There are several possible mechanisms which could result in a baroclinic wave response, including remote forcing from high latitudes, forcing through wind anomalies in mid-latitudes, or a number of possible triggering mechanisms within the tropics, such as ENSO or NAO teleconnections. The complexity of HadCM3 and the number of possible forcing mechanisms makes it very difficult to trace the origin of the wave propagation seen in the subsurface.

The role of the atmosphere in producing the decadal asymmetry is particularly interesting. The atmosphere alone is unable to produce such low frequency signals, so any effects it does have must be as part of a coupled ocean-atmosphere system. It is possible that once the dipolar signal has developed the atmosphere acts to enhance and sustain the anomaly through positive feedback.

7.2 Wave propagation in an idealised model

Experiments using an idealised ocean basin configuration in MOMA demonstrate a baroclinic ocean wave response to a high latitude anomaly.

A temperature anomaly placed in the north west corner of the basin perturbs the levels within the model, creating a baroclinic Kelvin wave response. The baroclinic Kelvin wave propagates equatorward along the western boundary. On reaching the equator an eastward propagating equatorial Kelvin wave develops and propagates to the eastern boundary. Here, poleward propagating Kelvin waves are formed, which initiate propagation of baroclinic Rossby waves back into the ocean interior as they propagate poleward along the eastern boundary.

It is clear from these experiments that it is possible for high latitude anomalies to have both a rapid and significant effect on the tropics. The importance of the equatorial waveguide is apparent. The effects of even a small anomaly are distributed throughout the equatorial and tropical regions, whereas areas away from the equator (eg mid-latitudes) show very little influence from the anomaly (Figure 4.7).

A paper by *Yang* (1999) illustrates an interesting wave response created in an idealised model through high latitude salt forcing. A cross-equatorial dipole is created in the idealised basin and all model fields are shown to adopt the period of the salt forcing.

The introduction of a sinusoidally varying salt forcing with a decadal period to the high latitudes results in a pulsing meridional overturning circulation at the same frequency. All variables within the model are seen to acquire this frequency. No evidence of an asymmetric cross-equatorial dipole appears in the SST, although some asymmetry arises from the southern tropical region responding more strongly to the signal than the northern tropical region. Some asymmetry can be seen forming in the shallow meridional overturning cells that operate in the tropics. This asymmetry could give rise to SST anomalies of opposite signs either side of the equator. The unrealistically strong surface forcing, which acts to damp any surface temperature or salinity anomalies back to the Levitus 1998 values over a period of 40 days may prevent decadal asymmetry from developing. In the case of a coupled system it would be possible for

feedback between the ocean and atmosphere to arise. Such feedback could sustain, or even enhance, SST anomalies in the tropics. A further study, in which an idealised coupled ocean-atmosphere model is used to try and establish a cross-equatorial dipole would be of interest. *Hüttl and Böning* (2006) discuss a model experiment in which cross-equatorial asymmetry could not be established as a result of applying a heat flux formulation to a more complex model experiment. The heat flux formulation used inhibits the formation of decadal variability in the tropical Atlantic because it prevents the possibility of air-sea interactions *Seager et al.* (2001).

7.3 Rapid ocean teleconnection in FORTE

Work using the FORTE coupled climate model has shown that it is possible for a very rapid response to occur through an ocean teleconnection. Barotropic Kelvin and Rossby waves propagate away from the source of the anomaly and are able to excite a baroclinic wave response in the equatorial waveguide. The baroclinic waves produce anomalies in the equatorial Pacific within 1 month, and strong SST anomalies are seen within 6 months of the start of the integration. Such a strong anomaly has good potential for triggering an El Niño event. *Reznik and Zeitlin* (2006) describe a plausible mechanism for the transfer of energy from barotropic waves into the equatorial waveguide, although without further model integrations it cannot be verified that this is precisely the mechanism seen in FORTE. It is clear from the timing of the SST response in the equatorial Pacific that the transfer of energy cannot be purely from a baroclinic signal propagating from the Weddell Gyre anomaly. Barotropic waves are seen to propagate throughout the global ocean, which means that exciting a similar response in the Atlantic and/or Indian ocean basins is entirely possible. Why the strongest response appears in the Pacific is not clear. It could be that the size of the basin allows resonance, which amplifies the signal. The study of the effects of model resolution on the propagation of Kelvin and Rossby waves suggests that the response seen in the FORTE model is likely to be considerably slower than reality. Although the barotropic wave propagation is comparatively well resolved at 2° resolution, the baroclinic response is not, even close to the equator. Some assessment of the effect of resolution on the response time could be done by repeating the experiments using a higher resolution version of FORTE. This is unfeasible due to the long spinup time required to reach (near) equilibrium in the model. The study on the influence of resolution on wave propagation in the idealised MOMA basin also suggests that a considerable increase in resolution from the current 2° version of the model would be necessary.

7.4 Energy exchange and the influence of topography

In chapter 6 two of the interesting results which arose in the FORTE model integrations from chapter 5 were examined using an idealised ocean basin.

A series of model experiments examined the possibility of a *Reznik and Zeitlin* (2006) type of energy exchange within the equatorial waveguide. Theoretical work suggests that it may be possible for barotropic wave propagation to excite an exponentially growing baroclinic kinetic energy response at the equator.

Placing an anomaly which creates a train of barotropic Kelvin waves on the western boundary of an idealised ocean basin triggers an equatorial baroclinic kinetic energy response. The barotropic waves do not appear to excite any significant baroclinic signal at the equator, as suggested by *Reznik and Zeitlin* (2006). Moving the location of the anomaly demonstrates that the large baroclinic response which appears along the equator is produced by baroclinic Kelvin wave propagation along the western boundary. A very different response is seen when the anomaly is located in the Southern Ocean, removing all direct pathways along which a coastal Kelvin wave may propagate. The response does not show an exponential growth in the baroclinic kinetic energy, although this may still occur later on if the integration were continued. The strong equatorial Pacific response seen in FORTE (chapter 5) occurs after only 6 months. If a barotropic-baroclinic energy exchange was involved, it should also appear in the idealised basin model within one year of integration.

The influence of topography on the wave response in the idealised basin is also examined. Topography representing the Mid-Atlantic Ridge is introduced to an idealised ocean basin and anomalies are placed at different locations in the north of the basin to excite an along-ridge response. In two experiments different anomalies are located over the ridge adjacent to the northern boundary. A baroclinic signal forms above the ridge, with opposite signs on either side. The signal grows along the ridge, but doesn't propagate in the same way as a coastal Kelvin wave or other coastally trapped wave. The similarity between the responses of the different anomalies suggests that the signal which develops is robust. A third experiment locates the anomaly to the east of the ridge, such that a response along the ridge is triggered by the coastal Kelvin wave which propagates west along the northern boundary. The response in this case is asymmetric in shape as well as sign, with more energy being transferred to the signal along the eastern side of the ridge than the west. A further experiment detaches the anomaly from the northern boundary, inhibiting the formation and propagation of the coastal Kelvin wave. Interestingly, the response at the ridge is still identifiable, although the magnitude is considerably weaker. In the absence of the coastal Kelvin wave, the along-ridge response becomes comparatively

much more significant.

The results suggest that anomalies are able to use topographic ridges to cross ocean basins, and that in locations such as the Southern Ocean where there is no direct connection of land masses to Antarctica, this mechanism could transfer energy and excite wave propagation along coastlines away from Antarctica. In the case of the results from the FORTE model (chapter 5), this mechanism is significant in transferring the signal from the coastal Kelvin wave which propagates along Antarctica across to the coast of Australia.

7.5 Oceanic and atmospheric roles in teleconnections

The results presented in the previous chapters, along with previous studies, suggest that both the ocean and atmosphere play important roles in teleconnections around the world (*Ivchenko et al.*, 2004; *Dickey et al.*, 1992; *Richardson et al.*, 2005; *Yuan and Martinson*, 2000). The ocean is shown in chapter 5 to be particularly important for teleconnections from high latitudes to the equator. The equatorial waveguide channels energy arriving from remote sources along the equator, focussing the signal along a channel where the coupled climate system is highly sensitive to even small perturbations (*Trenberth et al.*, 1998). It has been shown mathematically that a weak barotropic signal crossing the equatorial waveguide is able to excite an exponentially growing response along the equator (*Reznik and Zeitlin*, 2006). The energy analysis of the FORTE model results shows strong exchanges of energy between potential and internal kinetic energy.

The atmosphere is also capable of rapid teleconnections. The results presented in chapter 5 show an atmospheric teleconnection that bridges the equator and triggers a response in the high latitude northern hemisphere. It is entirely possible for the atmosphere to influence the equatorial regions also, but from the anomaly used in this integration it is clear that the ocean response dominates. Use of an atmospheric anomaly in the model, such as changes in wind stress over the Southern Ocean for example, may show the Atmosphere to be more significant in transmitting signals to the equator.

Atmospheric teleconnections are likely to arise from the anomalies that form in the tropics as a result of the ocean teleconnection. These have not been examined here, but previous publications show strong evidence for teleconnections from ENSO events to the high latitudes (*Dickey et al.*, 1992, 1999, 2003; *Mo et al.*, 1997; *Yuan and Martinson*, 2000). An interesting extension to the current study would be to introduce an anomaly to the tropics in the FORTE model and examine the remote responses which arise. There is potential to establish a feedback mechanism between high latitudes and the equator. A high latitude

anomaly can trigger an equatorial response, which in turn could result in a teleconnection to high latitudes, which could force another anomaly at high latitudes. Atmospheric teleconnections to the tropical Atlantic or Indian Oceans are also possible. Numerous studies have shown the influence of an atmospheric 'bridge' between the tropical Pacific and Atlantic oceans (*Czaja et al.*, 2002; *Chang et al.*, 2000; *Enfield and Mayer*, 1997; *Sutton et al.*, 2000; *Giannini et al.*, 2000; *Harrison and Larkin*, 1998; *Curtis and Hastenrath*, 1995). This 'bridge' has also been shown to work in the opposite direction, from the Atlantic Ocean to the Pacific Ocean (*Dong and Sutton*, 2002a).

Ocean teleconnections will have a stronger influence propagating from high latitudes to the equator than vice versa. Waves which propagate towards the equator are channelled into the equatorial waveguide. Energy accumulates here as Kelvin and Rossby waves propagate back and forth across the ocean basins. The equatorial and tropical atmosphere is very sensitive to small changes in the tropical ocean SST (*Trenberth et al.*, 1998). The atmosphere is less sensitive to SST anomalies at high latitudes, and there is no waveguide to concentrate the energy from ocean wave propagation.

7.6 Implications for predicting tropical climate phenomena

The results presented in this thesis emphasise the importance of the tropics with regards to climate phenomena on all timescales. They demonstrate clearly that anomalies which occur remote to the tropics are capable of influencing global climate, and the important role of planetary waves, which are able to rapidly transmit signals over great distances is made apparent.

It is clear that greater understanding of high latitude anomalies and remote forcing mechanisms is needed if we are to reliably predict tropical climate phenomena such as ENSO and the TAD. It is possible that a number of high latitude phenomena, from both the northern and southern hemisphere, could excite a baroclinic response in the equatorial waveguide. The tropical atmosphere is particularly sensitive to even small changes in SST, which means that even weak anomalies have the potential to trigger a strong climate response.

There are numerous difficulties to overcome in order to try and monitor the mechanism. At present it has been shown in some simple model studies that it is possible to transmit a signal from the Southern Ocean to the equator. These do not provide sufficient details on how or where to observe the ocean in order to detect the mechanism. The location of the anomaly introduced to FORTE in chapter 5

was chosen for several reasons, which are outlined within the chapter. It is not suggested that this is the only, or even the most likely, location for substantial anomalies to occur. The anomaly propagates a barotropic Kelvin wave along the Antarctic coast, which is able to propagate all the way around Antarctica. Wave propagation could be initiated from any location close to Antarctica. The Drake Passage location enables propagation of barotropic Rossby waves across to the western boundary, so may provide stronger forcing than some locations along the Antarctic coast.

In *Ivchenko et al.* (2004) energy is propagated to the western boundary solely through the barotropic Rossby wave response. The absence of topography from the model excludes the possibility of a Kelvin wave response crossing the Southern Ocean and propagating equatorward. Results from the FORTE model strongly suggest that the barotropic Kelvin wave component of the mechanism dominates, and that the majority of the energy is transmitted through this. A study to identify the relative roles of these two pathways would be useful and may facilitate observation of the teleconnection in the ocean.

Observation of the Rossby and Kelvin wave pathways will require different methods. The barotropic Rossby wave propagation may be observable by satellite (*Fu*, 2004). The temporal resolution of the TOPEX/Poseidon dataset is 10 days, which is not sufficient to capture the barotropic wave response. *Fu* (2004) regrid the data to produce a 3 day temporal resolution, at the cost of spatial resolution, and are able to show barotropic Rossby wave propagation. The Kelvin wave response is significantly faster, and even by regridding satellite data it is not possible to capture the wave propagation. Kelvin waves have been observed using tide gauges, but the tide gauge array is limited in the Southern Ocean and the data is heavily influenced by atmospheric variability. In both cases the difficulty will be in extracting the signal from the background. With the details of the source of the mechanism unknown it is impossible to identify an individual wave as a direct response to the anomaly in the same way that it is possible in the model data.

A more realistic approach to observing the mechanism could be to monitor barotropic Kelvin wave activity along the western boundary of the Southern Pacific. It may be possible to correlate enhanced Kelvin wave activity with enhanced variability in the Niño 3.4 index. Baroclinic Kelvin and Rossby wave activity along the equator is also observable in satellite data.

7.7 Further work

There is considerable work to be done to fully understand the teleconnection mechanisms linking high latitude oceans to the equator and tropics. The process of baroclinic wave propagation is already well documented, but the barotropic Rossby and Kelvin wave mechanism which is the focus of Chapter 5 is not well understood. Experiments using the FORTE model suggest that the barotropic Kelvin wave propagating along the coast of Antarctica and equatorwards along topographic features which cross the Southern Ocean carries more of the energy than the barotropic Rossby wave mechanism which is seen clearly in *Ivchenko et al.* (2004).

One extension of the study of fast climate responses using FORTE would be an ocean only integration, which would remove all atmospheric response to the anomaly. This would confirm the finding that the equatorial response results predominantly from fast wave propagation in the ocean. It would also clarify the NH high latitude response, and give a better indication of the role of the atmosphere in transmitting this high latitude response.

The most significant criticism of the FORTE model study was the use of an unrealistically large salinity anomaly. For the purpose of this study, which was primarily to identify and compare the relative roles of the ocean and atmosphere in facilitating the teleconnection between the high latitudes and the equator, the size of the anomaly is of minor importance. For future studies it will be important to quantify the anomaly, perhaps by identifying an extreme event which may occur once per century, or even once per decade. Results of model studies using a realistic forcing will enable quantifiable estimates of the response seen at the equator.

It is also important to examine other possible sources and locations for the anomaly. Wind stress variability over the Southern Ocean, changes in the strength of the ACC, fresh water and salt water anomalies are all plausible mechanisms for triggering the barotropic wave mechanism. All of these could occur at various locations round Antarctica, or as a circumpolar anomaly like the one used in *Richardson et al.* (2005). Northern hemisphere locations should also be considered, in particular regions of deep convection in the North Atlantic.

There is strong evidence to suggest that the mechanism could be able to produce El Niño conditions in the equatorial Pacific and therefore rapidly have global impact. This has not yet been proven in model studies, and would be a significant step towards justifying the mechanism as a focus for further work. In order to show the mechanisms capability to trigger, or even just enhance, and El Niño event it is first necessary to be able to reproduce a reliable ENSO signal, something that most coupled climate models are unable to do.

No examination of the signal which appears in the Atlantic or Indian ocean basins has been carried out in this study. El Niño has specifically been focussed on due to its demonstrated global connectivity and impact.

Numerous papers have been published showing strong atmospheric teleconnections between El Niño and the tropical Atlantic on interannual timescales. A possible further study would be to examine the significance of the direct barotropic wave signal to the tropical Atlantic compared to the atmospheric bridge from the equatorial Pacific. Does the direct signal influence different regions of the tropical Atlantic? It is known from previous studies that different areas of the tropical Atlantic are dominated by signals from different sources (*Sutton et al.*, 2000). It has also been documented that the atmospheric bridge predominantly provides interannual timescale variability. Does the direct teleconnection to the tropical Atlantic provide a wider range of timescales (eg seasonal, annual, decadal)?

Atmospheric propagation of signals from the equator to high latitudes has also been well documented (*Dickey et al.*, 2003). Are there oceanic signals which can rapidly feed back to the high latitude oceans in a similar way? The sensitivity of the tropical ocean and atmosphere to small perturbations in SST suggests that the barotropic propagation of signals will be far more effective in the pole – equator direction.

Chapter 8

Conclusion

This thesis examines the potential for tropical climate phenomena to be triggered from anomalies in the extra-tropics and high latitudes.

A study of the TAD in the COAPEC 100 year HadCM3 dataset shows that propagation of Kelvin and Rossby wave like signals within the equatorial waveguide play an important role in the nature of the SST anomaly. This suggests that the forcing mechanism for the TAD could be located outside the tropics. Idealised model studies show that a coastal Kelvin wave response can be triggered from the high latitude northern hemisphere. The Kelvin wave propagates to the equator, and then eastward along it. A Kelvin and Rossby wave response similar to the waves seen in the HadCM3 analysis forms. This result shows a connection between high latitude anomalies and responses in the tropical climate, which relies on the propagation of a baroclinic coastal Kelvin wave equatorward along the western boundary.

Integrations of the FORTE coupled climate model, presented in chapter 5, give further evidence that a high latitude anomaly can trigger a tropical climate response. The Weddell Sea location of the anomaly in this experiment means that the mechanism is more complex than the one described above, since there is no direct pathway for a baroclinic Kelvin wave to propagate to the equator. A strong response is seen in the equatorial Pacific after six months. This rapid response indicates that the signal must arrive through barotropic wave propagation, since the atmospheric response to the anomaly is shown to have little effect in the tropics. Analysis of the pathways along which energy propagates shows that topography extending away from the coast of Antarctica enables the signal to cross the Southern Ocean and form equatorward propagating Kelvin waves along the coast of Australia, South America and Africa.

Idealised basin model integrations are used in chapter 6 to further examine the equatorial energy exchange. They do not show a rapid growth of baroclinic kinetic energy arising from barotropic wave propagation. Instead, where a

pathway exists, the energy comes from equatorward propagating baroclinic Kelvin waves. In the case where the anomaly is located in the Drake Passage, with no available pathway for the baroclinic Kelvin wave to propagate, the equatorial response is very different. No exponential growth of the baroclinic energy is seen within the 360 day integration. Experiments using an idealised model with a Mid-Atlantic Ridge show that extension of a signal along topography does occur, and that at latitudes similar to the Southern Ocean the signal is potentially capable of extending across the Southern Ocean with sufficient strength to initiate a coastal Kelvin wave response. The signal does not propagate as a wave, instead it grows in amplitude, but remains weak near the equator. This suggests that propagation of a signal along the East Pacific Rise to the eastern equatorial Pacific is unlikely to result in a strong response.

This work demonstrates that the tropical climate is sensitive to anomalies at high latitudes. It shows that through barotropic wave propagation, the ocean is capable of rapidly influencing the tropics. Responses in the tropical ocean can occur on timescales more commonly associated with the atmosphere, and it is also shown that the ocean teleconnection is more important than the atmosphere for initiating tropical ocean responses when high latitude anomalies occur in the ocean.

Although there are areas where further work is needed to clearly establish the some of the processes involved in rapid ocean teleconnections between the high latitudes and tropics, the work in this thesis provides a compelling argument that such teleconnections cannot be ignored.

Appendix A

Energy budget analysis

To aid understanding of the wave propagation in the following chapters, analysis of the energy budget will be carried out. Volume averaged values of barotropic and baroclinic kinetic energy anomaly (A.1,A.2), available potential energy anomaly (A.3), and potential energy anomaly (A.4) are calculated in units kg m^{-1} s^{-2} throughout the domain. All equations calculate the anomaly (perturb-control), so results are purely the response of the ocean to the anomaly. Advection of energy across open boundaries means that the energy budget will not close to zero, but the equations still provide useful information on where and how signals from the anomaly propagate.

$$Ek\_bcl = \frac{1}{H}\int_z \frac{1}{2}\rho({u^i_{an}}^2 + {v^i_{an}}^2)\ dz \tag{A.1}$$

where u^i_{an}, v^i_{an} is the Eastward,Northward baroclinic velocity anomalies (perturb-control), ρ is density, and z is layer depth, and H is the ocean depth.

$$Ek\_btr = \frac{1}{2}\rho({u^e_{an}}^2 + {v^e_{an}}^2) \tag{A.2}$$

where u^e_{an}, v^e_{an} is the Eastward,Northward barotropic velocity anomalies.

$$A.P.E. = \frac{1}{2H}\int_z g\frac{\rho^2_{an}}{\overline{\rho_z}}\ dz \tag{A.3}$$

where g=gravity, ρ_{an}=perturbation-control density anomaly and $\overline{\rho_z}$ is an area averaged reference density.

$$P.E. = \frac{1}{H}\int_z \rho_{an} g z\ dz \tag{A.4}$$

where g=gravity,and z is the layer thickness.

Values are calculated for each grid point.

A.1 The JEBAR and buoyancy terms

Also calculated are two terms describing the exchange of energy. The JEBAR term (Joint Effect of Baroclinicity and Relief) (A.5) provides the exchange of energy between the internal and external modes (*Sarkisyan*, 1971; *Treguier*, 1992; *Ivchenko et al.*, 1997). It is non-zero in the presence of variable topography and a variable density field:-

$$T = \frac{1}{H}\int_z (P^e - P^B)U_m^e \frac{\partial H}{\partial x_m}\ dz \tag{A.5a}$$

where x_1, x_2 are horizontal distances in the easterly,northerly direction, U_m^e is the barotropic velocity anomaly in the easterly and northerly directions, P^B is the bottom pressure, P^e (external pressure) is calculated by

$$P^e = \frac{1}{H}\int_z P\ dz \tag{A.5b}$$

and

$$U_m^e \frac{\partial H}{\partial x_m} = U_1^{e2}\frac{\partial H}{\partial x_1} + U_2^{e2}\frac{\partial H}{\partial x_2} \tag{A.5c}$$

Exchange between potential energy and the internal mode of kinetic energy is calculated using:-

$$B = \frac{1}{H}\int_z w\rho_{an} g\ dz \tag{A.6}$$

where w is the vertical velocity.

Equations (A.5) and (A.6) are in units $\mathrm{kg\,m^{-1}s^{-3}}$. Exchange between potential energy and the external mode of kinetic energy is expressed through the combination of the JEBAR and Buoyancy terms. Energy is transferred between potential and the internal mode through the Buoyancy term (B). It is then redistributed between the internal and external modes using the JEBAR term (T). The anomaly (perturb-control) is calculated in each case.

The JEBAR term is non-zero where a density gradient exists above topography. Flow over topography results in compression/stretching of the water column, which results in vortex stretching. The term is most significant where there are strong density gradients and/or steep topography, such as coastal shelves and topographic features such as the Mid-Atlantic Ridge. It is not possible at present to accurately measure the JEBAR effect in the ocean. *Guo et al.* (2003) note that resolution can play an important role in the representation of the JEBAR term in numerical models. They find that coarse resolution models tend to underestimate the strength of the JEBAR term. For this study it is not possible to increase the

resolution of the model, but it does suggest that the results of the study are likely to be an underestimate of the response to a high latitude salinity anomaly.

Appendix B

Published GRL article

a

a

Bibliography

Adcroft, A. J., C. N. Hill, and J. C. Marshall (1999), A new treatment of the coriolis terms in C-grid models at both high and low resolutions, *Monthly Weather Review*, *127*, 1928–1936.

Arakawa, A. (1966), Computational design for long-term numerical integrations of the equations of atmospheric motion, *Journal of Computational Physics*, *1*, 119–143.

Arnault, S. (1987), Tropical Atlantic geostrophic currents and ship drifts, *Journal of Physical Oceanography*, *18*, 1050–1060.

Arnault, S., B. Bourles, Y. Gouriou, and R. Chuchla (1999), Intercomparison of upper layer circulation of the western equatorial Atlantic Ocean: In situ and satellite data., *Journal of Geophysical Research*, *104*(C9), 21,171–21,194.

BADCwebsite (2006), Met Office - Global Sea Ice Coverage and Sea Surface Temperature data (1856-present), `http://badc.nerc.ac.uk/data/gisst/`.

Bakun, A. (1978), Guinea Current Upwelling, *Nature*, *271*, 147–150.

Bayev, S. A., and A. B. Polonskiy (1991), Seasonal variability of the Equatorial Countercurrent and the North Equatorial Current in the central tropical Atlantic, *Oceanology*, *31*, 155–159.

Behera, S., S. Rao, H. Saji, and T. Yamagata (2003), Comments on "A cautionary note on the interpretation of EOFs", *Journal of Climate*, *16*(7), 1087–1093.

Betts, A. K., and M. J. Miller (1993), The Betts-Miller scheme, in *The representation of cumulus convection in numerical models of the atmosphere*, Eds. K.A. Emanuel and D.J. Raymond.

Binet, D. (1997), Climate and pelagic fisheries in the Canary and Guinea currents 1964-1993: The role of Trade Winds and the Southern Oscillation, *Oceanologia Acta*, *20*, 177–190.

Bischof, B., E. Rowe, A. J. Mariano, and E. H. Ryan (2001), Ocean Currents URL, `http://oceancurrents.rsmas.miami.edu/`.

Blaker, A. T., B. Sinha, V. O. Ivchenko, N. C. Wells, and V. B. Zalesny (2006), Identifying the roles of the ocean and atmosphere in creating a rapid equatorial response to a Southern Ocean anomaly, *Geopysical Research Letters*, *33, L06720, doi:10.1029/2005GL025474*, 1–4.

Bryan, K. (1969), A numerical model for the study of the circulation of the world ocean, *Journal of Computational Physics*, *4*(3), 347–376.

Cai, W., and P. G. Baines (2001), Forcing of the Antarctic Circumpolar Wave by El Niño-Southern Oscillation teleconnections, *Journal of Geophysical Research*, *106*(C5), 9019–9038.

Carton, J. A., X. H. Cao, B. S.Giese, and A. M.daSilva (1996), Decadal and interannual SST variability in the tropical Atlantic Ocean, *Journal of Physical Oceanography*, *26*(7), 1165–1175.

Cayan, D. R. (1992), Latent and sensible heat flux anomalies over the Northern Oceans: the connection to monthly atmospheric circulation, *Journal of Climate*, *5*, 354–369.

Chang, P., L. Ji, and H. Li (1997), A decadal climate variation in the tropical atlantic ocean from thermodynamics air-sea interactions, *Nature*, *385*, 516–518.

Chang, P., R. Saravanan, L. Ji, and G. Hegerl (2000), The Effect of local Sea Surface Temperatures on Atmospheric Circulation over the Tropical Atlantic Sector, *Journal of Climate*, *13*(13), 2195–2216.

Chelton, D. B., and M. G. Schlax (1996), Global observations of Rossby Waves, *Science*, *272*, 234–238.

Coward, A. C., and B. A. de Cuevas (2005), The OCCAM 66 level model: physics, initial conditions and external forcing, *NOC,S Internal Report*, *99*, 1–58.

Cox, M. D. (1984), A primitive equation, 3-dimensional model of the ocean, *GFDL Ocean Group Technical Report*, *1*.

Curtis, S., and S. Hastenrath (1995), Forcing of anomalous sea surface temperature evolution in the tropical Atlantic during Pacific warm events, *Journal of Geophysical Research*, *100*, 15,835–15,847.

Czaja, A., P. van der Vaart, and J. Marshall (2002), A Diagnostic Study of the Role of Remote Forcing in Tropical Atlantic Variability, *Journal of Climate*, *15*(22), 3280–3290.

Davey, M., W. Hseih, and R. Wajsowicz (1983), The Free Kelvin Wave with lateral and vertical viscosity, *Journal of Physical Oceanography*, *13*, 2182–2191.

Dickey, J. O., S. L. Marcus, and R. Hide (1992), Global Propagation of Interannual Fluctuations in Atmospheric Angular Momentum, *Nature*, *357*, 484–488.

Dickey, J. O., O. P. Gegout, and S. L. Marcus (1999), Earth-atmosphere Angular Momentum Exchange and ENSO: The Rotational Signature of the 1997-1998 Event, *Geophysical Research Letters*, *26*, 2477–2480.

Dickey, J. O., S. L. Marcus, and O. de Viron (2003), Coherent interannual and decadal variations in the atmosphere-ocean system, *Geophysical Research Letters*, *30*(11).

Dommenget, D., and M. Latif (2000), Interannual to Decadal Variability in the Tropical Atlantic, *Journal of Climate*, *13*(4), 777–792.

Dommenget, D., and M. Latif (2002), Notes and correspondence: A cautionary note on the interpretation of EOFs, *Journal of Climate*, *15*(2), 216–225.

Dommenget, D., and M. Latif (2003), Reply to comments of Behera et al., *Journal of Climate*, *16*(7), 1094–1097.

Dong, B., and R. Sutton (2002a), Adjustment of the coupled ocean-atmosphere system to a sudden change in the Thermohaline Circulation, *Geophysical Research Letters*, *29*(15), 18–1 to 18–4.

Dong, B., and R. Sutton (2002b), Variability in the North Atlantic heat content and heat transport in a coupled ocean-atmosphere GCM, *Journal of Climate Dynamics*, *19*, 485–497.

Dukowicz, J. K. (1995), Mesh effects for Rossby waves., *Journal of Computational Physics*, *119*, 188–194.

Edwards, N. R., and R. Marsh (2005), Uncertainties due to transport-parameter sensitivity in an efficient 3-D ocean-climate model, *Climate Dynamics*, *24*, 415–433.

Enfield, D., and D. Mayer (1997), Tropical Atlantic SST variability and its relation to El Niño-Southern Oscillation, *Journal of Geophysical Research*, *102*, 929–945.

Enfield, D., A. Mestas-Nunez, D. Mayer, and L. Cid-Serrano (1999), How ubiquitous is the dipole relationship in the tropical Atlantic sea surface temperatures, *Journal of Geophysical Research*, *104*(C4), 7841–7848.

Folland, C. K., T. N. Palmer, and D. E. Parker (1986), Sahel rainfall and worldwide sea temperatures: 1901-85, *Nature*, *320*, 602–607.

Fratantoni, D. M., W. E. Johns, and T. L. Townsend (1995), Rings of the North Brazil Current: Their structure and behavior inferred from observations and a numerical simulation, *Journal of Geophysical Research*, *100*(C6), 10,633–10,654.

Fu, L. L. (2004), Latitudinal and Frequency Characteristics of the Westward Propagation of Large-Scale Oceanic Variability, *Journal of Physical Oceanography*, *34*, 1907–1921.

Gent, P. R., and J. C. McWilliams (1990), Isopycnal mixing in ocean circulation models, *Journal of Physical Oceanography*, *20*, 150–155.

Giannini, A., Y. Kushnir, and M. A. Cane (2000), Interannual variability of the Carribean Rainfall, ENSO, and the Atlantic Ocean, *Journal of Climate*, *13*(2), 297–311.

Gill, A. E. (1982), *Atmosphere–Ocean Dynamics*, 662 pp., Academic Press.

Gill, A. E., and A. J. Clarke (1974), Wind induced upwelling, coastal currents, and sea level changes, *Deep Seas Research*, *21*, 325–345.

Gill, A. E., M. K. Davey, E. R. Johnson, and P. F. Linden (1986), Rossby adjustment over a step, *Journal of Marine Research*, *44*(4), 713–738.

Goodman, P. (2001), Thermohaline Adjustment and Advection in an OGCM, *Journal of Physical Oceanography*, *31*(6), 1477–1497.

Gordon, A. L., and J. C. Comiso (1988), Polynyas in the Southern-Ocean, *Scientific American*, *258*(6), 90–97.

Gordon, C., C. Cooper, C. Senior, H. Banks, J. Gregory, T. Johns, J. Mitchell, and R. Wood (2000), The simulation of SST, sea ice extents and ocean heat transports in a version of the Hadley Centre coupled model without flux adjustments, *Climate Dynamics*, *16*, 147–168.

Griffies, S. M., R. C. Pacanowski, and R. W. Hallberg (2000), Spurious Diapycnal Mixing Associated with Advection in a z-Coordinate Ocean Model, *Monthly Weather Review*, *128*, 538–564.

Griffies, S. M., R. C. Pacanowski, M. Schmidt, and V. Balaji (2001), Tracer Conservation with an Explicit Free Surface Method for z-Coordinate Ocean Models, *Monthly Weather Review*, *129*, 1081–1098.

Guo, X., H. Hukuda, Y. Miyazawa, and T. Yamagata (2003), A Triply Nested Ocean Model for Simulating the KuroshioRoles of Horizontal Resolution on JEBAR, *Journal of Physical Oceanography*, *33*, 146–169.

Handoh, I., A. Matthews, G. Bigg, and D. Stevens (2006), Dominant Coupled ocean-atmosphere interannual modes in the tropical Atlantic: Part I. The North Tropical Atlantic, *International Journal of Climatology*, *DOI: 10.1002/joc.1343*.

Harangozo, S. A. (2000), A search for ENSO teleconnections in the west Antarctic peninsula climate in Austral winter, *International Journal of Climatology*, *20*, 663–679.

Harrison, D. E., and N. K. Larkin (1998), El Niño-Southern Oscillation sea surface temperature and wind anomalies, 1946-1993, *Review of Geophysics*, *36*, 353–399.

Harzallah, A., J. O. R. D. Aragao, and R. Sadourny (1996), Interannual rainfall variability in northeast Brazil: Observation and model simulation, *International Journal of Climatology*, *16*, 861–878.

Hasselmann, K. (1988), PIP and POPs: The reduction of complex dynamical systems using Principal Interaction and Principal Oscillation Patterns., *Journal of Geophysical Research*, *93*, 11,015–11,021.

Hastenrath, S. (1985), *Climate and Circulation of the Tropics*, 455 pp., D. Reidel.

Hastenrath, S., and L. Druyan (1993), Circulation anomaly mechanisms in the tropical Atlantic sector during the Northeast Brazil rainy season: Results from the GISS General Circulation Model, *Journal of Geophysical Research*, *98*(D8), 14,917–14,923.

Hastenrath, S., and L. Greischar (1993), Circulation mechanisms related to Northeast Brazil rainfall anomalies, *Journal of Geophysical Research*, *98*(D3), 5093–5102.

Hastenrath, S., and L. Heller (1977), Dynamics of climatic hazards in Northeast Brazil, *Quarterly Journal of the Royal Meterological Society*, *103*, 77–92.

Hayes, S. P., P. Chang, and M. J. McPhaden (1991), Variability of the sea surface temperature in the eastern equatorial Pacific Ocean, *Journal of Geophysical Research*, *92*, 10,553–10,566.

Hellerman, S., and M. Rosenstein (1983), Normal monthly wind stress over the world ocean with error estimates, *Journal of Physical Oceanography*, *13*, 1093–1104.

Hickey, H., and A. J. Weaver (2004), The Southern Ocean as a Source Region for Tropical Atlantic Variability, *Journal of Climate*, *17*, 3960–3972.

Houghton, R., and Y. Tourre (1992), Characteristics of low frequency sea surface temperature fluctuations in the tropical Atlantic, *Journal of Climate*, *5*(7), 765–771.

Hseih, W., M. Davey, and R. Wajsowicz (1983), The Free Kelvin Wave in Finite-Difference Numerical Models, *Journal of Physical Oceanography*, *13*, 1383–1397.

Huang, B., and J. Shukla (1996), A comparison of two surface wind stress analyses over the tropical Atlantic during 1980-1987, *Journal of Climate*, *9*(6), 906–927.

Huang, B., and J. Shukla (1997), Characteristics of the interannual and decadal variability in a general circulation model of the tropical Atlantic Ocean, *Journal of Physical Oceanography*, *27*(8), 1693–1712.

Hulme, M. (1992), A 1951-80 global land precipitation climatology for the evaluation of general circulation models, *Climate Dynamics*, *7*, 57–72.

Hurrel, J. W. (1995), Decadal trends in the North Atlantic Oscillation regional temperatures and precipitation, *Science*, *269*, 676–679.

Hüttl, S., and C. Böning (2006), Mechanisms of decadal variability in the shallow subtropical circulation of the Atlantic Ocean: a model study, *Journal of Geophysical Research*, *111*(C7), 1–2.

Ingham, M. C. (1970), Coastal upwelling in the northwestern gulf of Guinea, *Bulletin of Marine Science*, *20*, 1–34.

Ivchenko, V. O., A. M. Treguier, and S. E. Best (1997), A Kinetic Energy Budget and Internal Instabilities in the Fine Resolution Antarctic Model, *Journal of Physical Oceanography*, *27*, 5–22.

Ivchenko, V. O., V. B. Zalesny, and M. R. Drinkwater (2004), Can the equatorial ocean quickly respond to Antarctic sea ice/salinity anomalies?, *Geophysical Research Letters*, *31*(L15310), doi:10.1029/2004GL020,472.

Jin, F. F. (2001), Low-frequency modes of tropical ocean dynamics, *Journal of Climate*, *14*, 3874–3881.

Johns, W. E., T. N. Lee, R. C. Beardsley, J. Candela, R. Limeburner, and B. Castro (1998), Annual cycle and variability of the North Brazil Current, *Journal of Physical Oceanogrpahy*, *28*(1), 103–128.

Joyce, T. M., C. Frankignoul, J. Yang, and H. E. Phillips (2004), Ocean response and feedback to the SST dipole in the Tropical Atlantic, *Journal of Physical Oceanography*, *34*(11), 2525–2540.

Kalnay, E., et al. (1996), The NCEP/NCAR 40-year reanalysis project, *Bull. Am. Meteorol. Soc.*, *77*, 437–471.

Karoly, D. J. (1989), Southern Hemisphere circulation features associated with El Niño-Southern Oscillation events, *Journal of Climate*, *2*, 1239–1252.

Killworth, P. D., and J. R. Blundell (1999), The effect of bottom topography on the speed of long extratropical planetary waves, *Journal of Physical Oceanography*, *29*, 2689–2710.

Killworth, P. D., and J. R. Blundell (2003), Long Extratropical Planetary Wave Propagation in the Presence of Slowly Varying Mean Flow and Bottom Topography. Part I: The Local Problem, *Journal of Physical Oceanography*, *33*, 784–801.

Killworth, P. D., D. Stainforth, D. J. Webb, and S. M. Paterson (1991), The development of a free-surface Bryan-Cox-Semtner ocean model, *Journal of Physical Oceanography*, *21*, 1333–1348.

Killworth, P. D., D. B. Chelton, and R. A. de Szoeke (1997), The Speed of Observed and Theoretical Long Extratropical Planetary Waves, *Journal of Physical Oceanography*, *27*, 1946–1966.

Lamb, P. J. (1978), Large-scale tropical Atlantic circulation patterns associated with sub-Saharan Africa weather anomalies, *Tellus*, *30*, 240–251.

Lamb, P. J., and R. A. Peppler (1987), North Atlantic Oscillation: Concept and an application, *Bull. Amer. Meteor. Soc.*, *68*, 1218–1225.

LeBlond, P. H., and L. A. Mysak (1978), *Waves in the Ocean*, 602 pp., Elsevier.

Levitus, S., and T. P. Boyer (1998), World Ocean Atlas 1998, Volume 4, Temperature., *NOAA Atlas*, *NESDIS 2*, 99pp.

Levitus, S., R. Burgett, and T. P. Boyer (1998), World Ocean Atlas 1998, Volume 3, Salinity., *NOAA Atlas*, *NESDIS 3*, 99pp.

Liu, Z. (2002), How long is the memory of Tropical Ocean Dynamics?, *Journal of Climate*, *15*(23), 3518–3522.

Liu, Z., L. Wu, R. Gallimore, and R. Jacobs (2002), Search for the origins of Pacific decadal climate variability, *Geophysical Research Letters*, *29*, 42–1–42–4.

Longhurst, A. R. (1962), A review of the Oceanography of the Gulf of Guinea, *Bull. Inst. Afr. Noire*, *24*, 633–663.

Lough, J. M. (1986), Tropical Atlantic sea surface temperatures and rainfall variations in subsaharan africa, *Monthly Weather Review*, *114*, 561–570.

Marchal, E., and J. Picaut (1977), Repartition et abondance evaluees par echo-integration des poissons du plateau Ivoiro-Ghaneen en relation avec les upwellings locaux, *J. Rech. Oceanogr.*, *2*, 39–57.

Markham, C. G., and D. R. McLain (1977), Sea surface temperatures related to rain in Cear, Northeastern Brazil, *Nature*, *265*, 320–323.

Mead, C. T. (1989), Asymmetries of the oceanic thermohaline circulation and meridional heat transport, *University of Southampton PhD Thesis*, p. 254.

Mehta, V. M. (1998), Variability of the tropical ocean surface temperatures at decadal-multidecadal timescales. Part I: The Atlantic Ocean, *Journal of Climate*, *11*(9), 2351–2375.

Mo, K. C., J. O. Dickey, and S. L. Marcus (1997), Interannual Fluctuations in Atmospheric Angular Momentum Simulated by the NCEP Medium Range Forecast Model, *Journal of Geophysical Research*, *102*, 6703–6713.

Molinari, R. L. (1982), Observations of eastward currents in the tropical South Atlantic Ocean, *Journal of Geophysical Research*, *87*, 9707–9714.

Moura, A. D., and J. Shukla (1981), On the dynamics of droughts in Northeast Brazil: Observations, theory and numerical experiments with a general circulation model, *Journal of Atmospheric Science*, *38*, 2653–2675.

Munk, W. H. (1950), On wind-driven ocean circulation, *Journal of Meteorology*, *7*, 79–93.

Munnich, M., M. Cane, and S. Zebiak (1991), A study of self-excited oscillations in a tropical oceanatmosphere system. Part II: Nonlinear cases, *Journal of Atmospheric Science*, *48*, 1238–1248.

Nobre, P., and J. Shukla (1996), Variations of Sea Surface Temperature, Wind Stress, and Rainfall over the Tropical Atlantic and South America, *Journal of Climate*, *9*(10), 2464–2479.

North, G. R., T. L. Bell, and R. F. Cahalan (1982), Sampling Errors in the Estimation of EOFs, *Monthly Weather Review*, *110*, 699–706.

O'Brien, J. J. (1986), The Diffusive Problem, *Proceedings of the NATO Advanced Study Institute on Advanced Physical Oceanographic Numerical Modelling*, pp. 127–144, D. Reidel Publishing Co., Dordrect.

Pacanowski, R. C., and S. M. Griffies (2000), MOM 3.0 Manual, *Tech. rep.*, NOAA/Geophysical Fluid Dynamics Laboratory.

Paris, C. B., R. K. Cowen, K. M. Lwiza, D. P. Wang, and D. B. Olson (2002), Multivariate objective analysis of the coastal circulation of Barbados, West Indies: implication for larval transport, *Deep-Sea Research Part I*, *48*(8), 1363–1386.

Peterson, R. G., and L. Stramma (1991), Upper-level circulation in the South Atlantic Ocean, *Progress in Oceanography*, *26*, 1–73.

Peterson, R. G., and W. B. White (1998), Slow teleconnections linking the Antarctic Circumpolar Wave with the tropical El Niño-Southern Oscillation, *Journal of Geophysical Research*, *103*, 24,573–24,583.

Philander, G., D. Gu, D. Halpern, G. Lambert, N.-C. Lau, T. Li, and R. C. Pacanowski (1996), Why the ITCZ is mostly North of the Equator, *Journal of Climate*, *9*(12), 2958–2972.

Philander, S. G. H. (1990), *El Niño, La Niña and the Southern Oscillation*, 289 pp., Elsevier, New York.

Picaut, J. (1983), Propagation of the seasonal upwelling in the eastern equatorial Atlantic, *Journal of Physical Oceanography*, *13*, 18–37.

Pope, V. D., M. L. Gallani, P. R. Rowntree, and R. A. Stratton (2000), Propagation of the seasonal upwelling in the eastern equatorial Atlantic, *Climate Dynamics*, *16*, 123–146.

Rao, V. B., M. C. D. Lima, and S. H. Franchito (1993), Seasonal and interannual variations of rainfall over eastern northeast Brazil, *Journal of Climate*, *6*(9), 1754–1763.

Reznik, G. M., and V. Zeitlin (2006), Resonant excitation of Rossby waves in the equatorial waveguide and their nonlinear evolution, *Physical Review Letters*, *96*(3), 1–4.

Richardson, G., M. R. Wadley, K. Heywood, D. P. Stevens, and H. T. Banks (2005), Short-term climate response to a freshwater pulse in the Southern Ocean, *Geophysical Research Letters*, *32*(L03702), doi:10.1029/2004GL021,586.

Richardson, P. L., and G. Reverdin (1987), Seasonal cycle of velocity in the Atlantic North Equatorial Countercurrent as measured by surface drifters, current meters, and ship drifts, *Journal of Geophysical Research*, *92*, 3691–3708.

Richardson, P. L., and D. Walsh (1986), Mapping climatological seasonal variations of surface currents in the tropical Atlantic using ship drifts, *Journal of Geophysical Research*, *91*, 10,537–10,550.

Rogers, J. C. (1990), Patterns of low-frequency monthly sea-level pressure variability (1899-1986) and associated wave cyclone frequencies, *Journal of Climate*, *3*, 1364–1379.

Rowell, D. P., C. K. Folland, and K. M. an M. N. Ward (1995), Variability of summer rainfall over tropical North Africa (1906-92): Observations and modelling, *Quarterly Journal of the Royal Meteorological Society*, *121*, 669–704.

Sarkisyan, A. S. (1971), Joint effect of baroclinicity and bottom relief as an important factor in the dynamics of sea currents (in Russian), *Izv. Acad. Sci. USSR, Atmos. Oceanic Phys.*, *7*, 116–124.

Schott, F. A., J. Fischer, and L. Stramma (1998), Transports and pathways of the upper-layer circulation in the western tropical Atlantic, *Journal of Physical Oceanography*, *28*(10), 1904–1928.

Seager, R., Y. Kushnir, N. Naik, J. Chiang, and J. Miller (2001), Looking for the role of the ocean in Tropical Atlantic Decadal Climate Variability, *Journal of Climate*, *14*(5), 638–655.

Semtner, A. J. (1974), Simple climatic indices for the tropical Atlantic Ocean and some applications, *Technical Report, UCLA Department of Meteorology*, *9*.

Servain, J. (1991), An oceanic general circulation model with bottom topography. in: Numerical Simulation of Weather and Climate, *Journal of Geophysical Research*, *96*(C8), 15,137–15,146.

Simmonds, I., and T. H. Jacka (1995), Relationships between the Interannual Variability of Antarctic Sea Ice and the Southern Oscillation, *Journal of Climate*, *8*, 637–647.

Sinha, B., and R. Smith (2002), Development of a fast Coupled General Circulation Model (FORTE) for climate studies, implemented using the OASIS coupler, *Tech. rep.*, Southampton Oceanography Centre, Internal Document, No. 81, 67pp.

Smith, R., C. Dubois, and J. Marotzke (2004), Ocean circulation and climate in an idealised Pangean OAGCM, *Geophysical Research Letters*, *31*(L18207), doi:10.1029/2004GL020,643.

Stramma, L. (1991), Geostrophic transport of the South Equatorial Current in the Atlantic, *Journal of Marine Research*, *49*, 281–294.

Sutton, R., S. Jewson, and D. Rowell (2000), The elements of climate variability in the tropical Atlantic region, *Journal of Climate*, *13*(18), 3261–3284.

Terray, L., S. Valcke, and A. Piacentini (1999), The OASIS Coupler User Guide Version 2.3, Tech. Rep. TR/CMGC/99-37, *Tech. rep.*, CERFACS, Toulouse, France,.

Thompson, H. D., B. W. Webb, and J. D. Hoffman (1985), The cell Reynolds number Myth, *International Journal of Numerical Methods in Fluids*, *5*, 305–310.

Tomas, R. A., and P. J. Webster (1994), Horizontal and Vertical Structure of Cross-Equatorial Wave Propagation, *Journal of Atmospheric Science*, *51*(11), 1417–1430.

Tourre, Y., B. Rajagopalan, and Y. Kushnir (1999), Dominant Patterns of Climate Variability in the Atlantic Ocean Region During the Last 136 Years, *Journal of Climate*, *12*(8), 2285–2299.

Treguier, A. M. (1992), Kinetic energy analysis of an eddy resolving, primitive equation model of the North Atlantic, *Journal of Geophysical Research*, *97*, 687–701.

Trenberth, K. E., and J. M. Caron (2001), Estimates of meridional atmosphere and ocean heat transports, *Journal of Climate*, *14*, 3433–3443.

Trenberth, K. E., G. W. Branstator, D. Karoly, A. Kumar, N.-C. Lau, and C. Ropelewski (1998), Progress during TOGA in understanding and modelling global teleconnections associated with tropical sea surface temperatures, *Journal of Geophysical Research*, *103*, 14,291–14,324.

Venegas, S., and M. R. Drinkwater (2001), Sea ice, atmosphere, and upper ocean variability in the Weddell Sea, Antarctica, *Journal of Geophysical Research*, *106*, 16,747–16,766.

Verstraete, J. M. (1992), The seasonal upwellings in the Gulf of Guinea, *Progress in Oceanography*, *29*, 1–60.

Wajsowicz, R. C. (1986), Free planetary waves in Finite-difference numerical models, *Journal of Physical Oceanography*, *16*, 773–789.

Weare, B. C. (1977), Empirical orthogonal analysis of Atlantic Ocean surface temperatures, *Quarterly Journal of the Royal Meteorological Society*, *103*, 467–478.

Webb, D. J. (1996), An ocean model code for array processor computers, *Computers and Geosciences*, *22*(5), 569–578.

Wilson, W. D., E. Johns, and R. L. Molinari (1994), Upper layer circulation in the western tropical North Atlantic Ocean during August 1989, *Journal of Geophysical Research*, *99*, 22,513–22,523.

Xie, S.-P. (2001), Coupled Aspect of Atlantic Ocean-Atmosphere Variability, *CLIVAR Publication Series*, *42*, 46–64.

Yang, J. (1999), A linkage for decadal climate variations in Labrador Sea and the tropical Atlantic Ocean, *Geophysical Research Letters*, *26*, 1023–1026.

Yuan, X., and D. G. Martinson (2000), Antarctic sea ice extent variability and its global connectivity, *Journal of Climate*, *13*, 1697–1717.

Zebiak, S. E. (1989), Oceanic heat content and El Niño Cycles, *Journal of Physical Oceanography*, *19*, 475–486.

Zebiak, S. E. (1993), Air-sea interaction in the equatorial Atlantic region, *Journal of Climate*, *6*(8), 1567–1586.